



Chair of Metal Forming

Master's Thesis



Parameter Optimisation Study  
for the Finite-Element Analysis of  
Wire-Arc Additive Manufacturing

Marcel Czipin

April 2023





**MONTANUNIVERSITÄT LEOBEN**  
www.unileoben.ac.at

## Affidativ

I declare in lieu of an oath that I have written this thesis independently, that I have not used any sources or aids other than those indicated and that I have not made use of any unauthorized aids.

I declare that I have read, understood and followed the guidelines of the Senate of the University of Leoben „Good Scientific Practice“ .

Furthermore, I declare that the electronic and printed version of the submitted scientific thesis are identical in form and content.

Leoben, 12.04.2023

---

Signature of the author

Marcel Czipin



# Acknowledgments

First and foremost, my thanks go to Univ.-Prof. Dipl.-Ing. Dr.techn. Martin Stockinger as head of the Chair of Metal Forming for the approval and supervision of this project. Without his trust and the provided resources, this thesis would not have been possible.

I would also like to thank the entire chair's team for the welcoming environment, especially Dipl.-Ing. Karin Hartl as co-supervisor and for her support over the course of this project.

Furthermore, I want to thank all friends I have found in fellow students, above all Alexander and Wolfgang, for the long-standing mutual support and cohesion throughout our studies.

# Abstract

This thesis investigates the feasibility of the Finite-Element software DEFORM<sup>®</sup> in multi-layer arc welding by applying Design of Experiments to statistically analyse welding parameter influences. For this purpose, a manufacturing experiment was conducted, in which 32 layers of Ti-6Al-4V were built onto a substrate plate fitted with thermocouples to log the temperature history. The obtained real process data was then used to extract the layer timing and detailed movement data of the welding torch. A heat source model was then programmed in MATLAB<sup>®</sup> based on the normalised layer height and volumetric heating power, controlling thermal power depending on real deposition settings. Dummy heat sources were introduced to correctly activate each layer due to restrictions inside the DEFORM<sup>®</sup> arc welding environment. All accomplished results were combined in one time-synchronised heat source model to ensure convenient timetable import in simulations. Furthermore, the standardised Ti-6Al-4V material model was improved and extended to ensure accurate and stable calculations.

A parameter analysis study was conducted by applying statistical Design of Experiments, in which the absolute deviation between the temperature response curves and their thermocouple counterparts served as a comparative basis. A total of 8 parameters were identified as interesting and grouped in three experimental runs. Each run focused on different emphases to reduce the individual parameter count and thus the number of experiments needed for meaningful results. Individual timestamps were investigated through full quadratic response surface models, finding theoretical optimal process parameters for each subsequent data point. For this purpose, a custom MATLAB<sup>®</sup> code was developed for enhanced analysis, chaining the individual results to form a time series based analysis. Thermal conductivity  $k$  and heat source power efficiency  $\eta$  were found to be most influential by far, and the front and rear ellipsoid apex showed to be most influential among geometrical heat source parameters. Due to their small deviation from values suggested in literature, normalised heat source dimensions were used to focus on energetic parameters, enabling the proposal of time-dependent functions for heat source power and conductive boundary conditions.

An improved Finite-Element model was built using all gathered information, which follows boundary conditions and timings as realistically as possible. A very accurate approximation of real temperature measurements was possible in thermal analysis, however, the certainty of a realistic development remains to be confirmed by subsequent experiments.

# List of Acronyms

3D	3 dimensional
AI	Artificial Intelligence
AM	Additive Manufacturing
ANN	Artificial Neural Network
ANOVA	Analysis of Variance
CCC	Circumscribed Central Composite
CCD	Central Composite Design
CCF	Faced Central Composite
CCI	Inscribed Central Composite
CFD	Computational Fluid Dynamics
CMT	Cold Metal Transfer
CNC	Computerised Numerical Control
CPU	Central Processing Unit
DDF	Deposition Difference Factor
DEM	Diffuse Element Method
DoE	Design of Experiments
DoF	Degrees of Freedom
DL	Deep Learning
EFG	Element-Free Galerkin Method
FE	Finite-Element
FEA	Finite-Element Analysis
GDE	Goldak Double Ellipsoid
GMAW	Gas Metal Arc Welding
GPU	Graphics Processing unit
GTAW	Gas Tungsten Arc Welding
HAZ	Heat Affected Zone
ML	Machine Learning
PAW	Plasma Arc Welding
RMSE	Root Mean Square Error
RSM	Response Surface Methodology
TC	Thermocouple
WAAM	Wire-Arc Additive Manufacturing

# List of Symbols

$\beta_{ij}$	-	Response surface coefficients
$\eta$	-	Thermal efficiency
$\lambda$	$\frac{W}{m^2 \cdot K}$	Coefficient of heat conduction
$\mu_{SA}$	-	Steel - Aluminium coulomb friction coefficient
$\mu_{TA}$	-	Titanium - Aluminium coulomb friction coefficient
$\mu_{TS}$	-	Titanium - Steel coulomb friction coefficient
$\mu_{TT}$	-	Titanium - Titanium coulomb friction coefficient
$\sigma$	MPa	Stress
$\sigma_r$	$\frac{W}{m^2 \cdot K^4}$	Stefan Boltzmann constant
$\varepsilon$	-	Strain
$\varepsilon_e$	-	Elastic strain
$\varepsilon_p$	-	Plastic strain
$\varepsilon_r$	-	Emissivity
$\varepsilon_{th}$	-	Thermal induced strain
$\rho$	$\frac{kg}{m^3}$	Material density
$N_{layers}$	-	Number of layers deposited
$A_{layer}$	mm <sup>2</sup>	Top-view surface are of one layer
$b_{norm}$	mm	Normalised width of the deposited wall
$b_{weld}$	mm	Real width of the deposited wall
$C_f$	m	Front ellipsoid apex
$c_p$	$\frac{J}{kg \cdot K}$	Specific heat capacity
$C_{pL}$	$\frac{J}{kg}$	Liquidus heat capacity
$C_{pS}$	$\frac{J}{kg}$	Solidus heat capacity
$C_{pT}$	$\frac{J}{kg}$	Transition heat capacity
$C_r$	m	Rear ellipsoid apex
$C_y$	m	Common ellipsoid width
$C_z$	m	Common ellipsoid depth
$d$	mm	Diameter
$ddf$	-	Deposition Difference Factor
$F$	N	Force



$f_f$	-	Power distribution factor to the front
$f_r$	-	Power distribution factor to the rear
$h_c$	$\frac{W}{m^2 \cdot K}$	Coefficient of heat convection
$H_L$	J	Liquidus enthalpalpy
$h_{layer}$	mm	Layer height
$H_S$	J	Solidus enthalpalpy
$H_T$	J	Transition enthalpalpy
$h_{wall}$	mm	Height of the deposited wall
$k$	$\frac{N}{mm \cdot s \cdot K}$	Coefficient of heat conduction
$l_{layer}$	mm	Absolute length of a deposited layer
$l_{travel}$	mm	Effective torch travel length
$M_T$	Nm	Torque
$P$	W	Power
$Q$	W	Total heat source power
$Q_{cd}$	$\frac{W}{m^2}$	Conductive heat flux
$Q_{cv}$	$\frac{W}{m^2}$	Convective heat flux
$Q_f$	W	Heat source power to the front
$Q_r$	$\frac{W}{m^2}$	Radiation heat flux
$Q_r$	W	Heat source power to the rear
$s$	$\frac{s}{step}$	Stepwidth
$S$	-	Response surface
$T$	°C	Temperature
$t$	s	Time
$T_0$	°C	Reference temperature
$T_i$	°C	Initial element activation temperature
$T_L$	°C	Liquidus temperature
$T_S$	°C	Solidus temperature
$T_T$	°C	Transition temperature
$V_{layer}$	mm <sup>3</sup>	Layer volume
$x$	mm	Absolute distance in x coordinate
$x_i$	-	Response surface input parameter
$y$	mm	Absolute distance in y coordinate
$y_{shift}$	mm	Excentric shift of the weld bead center line
$z$	mm	Absolute distance in z coordinate

# Table of Contents

<b>Acknowledgments</b> . . . . .	<b>I</b>
<b>Abstract</b> . . . . .	<b>II</b>
<b>List of Acronyms</b> . . . . .	<b>III</b>
<b>List of Symbols</b> . . . . .	<b>IV</b>
<b>Table of Contents</b> . . . . .	<b>VI</b>
<b>1 Introduction</b> . . . . .	<b>1</b>
<b>2 Theoretical Background</b> . . . . .	<b>2</b>
2.1 Wire-Arc Additive Manufacturing . . . . .	2
2.1.1 Welding Technology . . . . .	2
2.1.2 Parameters and Influencing Variables . . . . .	4
2.1.3 Opportunities and Challenges . . . . .	7
2.2 Ti-6Al-4V Properties in Arc Welding . . . . .	11
2.3 Finite-Element Analysis of Arc Welding Processes . . . . .	12
2.3.1 Thermal Analysis . . . . .	12
2.3.2 Mechanical Analysis . . . . .	14
2.3.3 Suitable Elements . . . . .	14
2.3.4 Mesh Structure and Creation . . . . .	15
2.3.5 Weld Bead Models . . . . .	16
2.3.6 Heat Source Models . . . . .	20
2.3.7 Element Activation Strategies . . . . .	23
2.4 Statistical Design of Experiments . . . . .	26
2.4.1 Procedure . . . . .	26
2.4.2 Opportunities . . . . .	27
2.4.3 Applications . . . . .	27
2.4.4 Statistical Approaches and Design Methods . . . . .	27

<b>3</b>	<b>Numerical Modelling of the Experiment</b>	<b>31</b>
3.1	Experimental Setup	31
3.1.1	Temperature Measurement	32
3.1.2	Process Data	33
3.2	Data Preparation and Methodic Implementation	33
3.2.1	3D Modelling	33
3.2.2	Extraction of Individual Layer Times	34
3.2.3	Layer Model	36
3.2.4	Wire Feed Strategy	37
3.2.5	Arc Power Normalisation	38
3.2.6	Activation Volume	40
3.2.7	Time Synchronised Process Control	40
3.2.8	Introduction of Dynamic Step Size	42
3.2.9	Detailed Material Model for Ti-6Al-4V	44
3.3	Pre-Processing in DEFORM <sup>®</sup>	45
3.3.1	Geometry	45
3.3.2	Meshing	46
3.3.3	Calculation Steps	47
3.3.4	Boundary Conditions	48
3.3.5	Heat Source and Activation Volume Setup	53
3.3.6	Step Size and Simulation Control	54
3.3.7	Point Tracking for Temperature Response	54
<b>4</b>	<b>Parameter Optimisation</b>	<b>56</b>
4.1	Analysis of Influencing Variables	56
4.1.1	Thermal Efficiency	56
4.1.2	Goldak Double Ellipsoid Parameters	56
4.1.3	Element and Time Step Size	57
4.1.4	Properties of Molten Elements	59
4.2	Design of Experiments	59
4.2.1	Determination of the Objective	59
4.2.2	Reference Data	59

4.2.3	Design Method . . . . .	60
4.2.4	Response Surface Model . . . . .	62
4.2.5	Interpretation Method . . . . .	65
4.3	Simulation Runs and Parameter Variation . . . . .	67
4.3.1	Run 1 - Inspection of Geometric Influence . . . . .	67
4.3.2	Run 2 - Inspection of Thermal Influence . . . . .	69
4.3.3	Run 3 - Verification of Contact Setting Assumptions . . . . .	71
4.4	Improved Approach through Previous Findings . . . . .	72
4.4.1	Heat Source Setup in DEFORM <sup>®</sup> . . . . .	72
4.4.2	Mesh Generation for Layer-Wise Arc Welding . . . . .	73
4.4.3	Time Dependent Thermal Conduction . . . . .	75
4.4.4	Contact Property Definition . . . . .	75
4.4.5	Simulation Control . . . . .	77
4.4.6	Temperature Response with Optimised Parameters . . . . .	77
<b>5</b>	<b>Results . . . . .</b>	<b>79</b>
5.1	Realistic Heat Source Model . . . . .	79
5.2	Improved Ti-6Al-4V Material Model for Arc Welding . . . . .	80
5.3	Parameter Studies . . . . .	81
5.4	Resulting Finite Element Model . . . . .	82
<b>6</b>	<b>Discussion . . . . .</b>	<b>85</b>
6.1	Raw Data and Boundary Conditions . . . . .	85
6.2	Methodic Implementation . . . . .	87
6.3	Influence and Effect of Parameters . . . . .	88
6.4	Multi-Layer Arc Welding in DEFORM <sup>®</sup> 12.1 . . . . .	89
<b>7</b>	<b>Conclusion and Outlook . . . . .</b>	<b>91</b>
7.1	Dynamic Process Values . . . . .	91
7.2	Improved Temperature Measurement . . . . .	92
7.3	Automation and Digitalisation . . . . .	92
7.4	Advanced Statistical Analysis and Machine Learning . . . . .	93
	<b>List of Figures . . . . .</b>	<b>94</b>
	<b>List of Tables . . . . .</b>	<b>96</b>
	<b>Bibliography . . . . .</b>	<b>97</b>
	<b>A Improved Material Model for Ti-6Al-4V . . . . .</b>	<b>104</b>
	<b>B Design of Experiments . . . . .</b>	<b>105</b>

# 1 Introduction

Wire-Arc Additive Manufacturing (WAAM) can be used to rapidly build complex parts while maintaining material efficiency and reducing machining costs. This is especially important for large structural components, often made from high performance materials like the grade 5 titanium alloy Ti-6Al-4V. In contrast to other Additive Manufacturing (AM) processes, arc welding is utilised to drastically increase the material feed rate. Therefore, larger parts can be built in comparable short time with rather inexpensive equipment.

However, using a powerful arc welding heat source also comes with disadvantages. Local temperature gradients and overall heat distribution are drastically affected, which can cause distortion and residual stresses in the built workpiece, if not controlled correctly. Combined with a rough and geometrically indeterminate surface finish of the welded layers, adhering to manufacturing tolerances can be a challenge.

Finite-Element Analysis (FEA) can be used to optimise the distortion and residual stress distribution in a component to be built with WAAM. For this analysis to work properly, process parameters need to be determined very precisely, which can be difficult to conduct. Besides parameters like the heat transfer coefficient between the substrate and adjacent components or the emissivity of welded materials, the arc welding heat source turns out to play a major role. Due to its complex three dimensional geometric shape, small variations can evoke big impact on the heat affected zone (HAZ) around the weld pool and thus affect the precision of the FEA. There are also differences in methods used to activate elements around the heat source while welding, which further increases the complexity and error possibility.

Previous investigations in [1] focused on testing the general usability of the then newly available AM module in DEFORM<sup>®</sup> version 12.1 by replicating a single wall manufacturing experiment conducted in [2]. During the comparison of simulation results and real measurements, it became clear that the FEA in DEFORM<sup>®</sup> showed significant differences in some process stages. Therefore, this thesis pursues the objective of building on previous findings to further refine the heat source model, as well as overall boundary conditions. The ultimate goal is to improve the accuracy of FEA to a point at which reliable predictions of the distortion and stress in a manufactured part can be made.

## **2 Theoretical Background**

In the following paragraphs, a summary of the findings of recent scientific papers and literature shall be conducted to create a knowledge basis for further investigations. This includes an overview of the used manufacturing method and material, as well as possible models for FEA studies regarding the heat source.

### **2.1 Wire-Arc Additive Manufacturing**

Contrary to other AM processes, WAAM utilises an arc welding heat source to locally melt wire which is automatically fed into the welding pool. An inert gas atmosphere protects the liquid and freshly solidified material around the HAZ. Commonly available welding equipment is used to produce parts very cost effective and allows easy setup changes. By mounting the welding equipment onto some sort of Computerised Numerical Control (CNC) device, automatic material application becomes possible. This functionality is then used to build multiple layers of material onto the substrate, which commonly vary between 1-2mm in height. As of the comparably large layer height and faster feed rates, building time can be drastically reduced compared to powder based AM. [3, 4, 5, 6, 7]

The substrate can be a simple half finished product or an already existing part which needs to be repaired. It provides the basis for every WAAM process and therefore needs to be mounted onto the fixture table properly, to make electrical contact for arc welding. Usually, generic machine shop clamps are used to hold the substrate in place on a slotted welding table. [3, 8, 9]

After machine calibration, the building process can be started. To assure proper adhesion, it can be necessary to conduct preheating passes with the welding torch or to apply preceding heat treatments in an oven. This ensures consistent bonding between the weld bead and substrate by decreasing the temperature gradient induced through arc welding. [4, 9]

#### **2.1.1 Welding Technology**

In contrast to other AM processes, spooled wire is used as build material. This drastically increases deposition rates and heat sources with less energy density are necessary to quickly

melt a high volume of material. Fundamentally, any electric arc heat source can be used in WAAM. However, the most commonly used technologies can be summed up in three categories, as also visualised and compared in Figure 2.1: [6, 7, 10, 11, 12]

1. Gas Tungsten Arc Welding (GTAW)

An electric arc is created between a next to non-wearing wolfram electrode and the substrate material. This electrode is covered by a shielding gas nozzle to protect the molten pool and cool the torch. Since the arc can be controlled quite well and held stable, surface quality is usually excellent. However, the welding wire needs to be added separately from a specialised outside feeding device. [10]

2. Gas Metal Arc Welding (GMAW)

In contrast to other technologies, the wire is simultaneously used as melting electrode and constantly fed through the torch nozzle. Unpredictable arc interruptions and re-ignition upon contact with the substrate, may cause spatter and overall surface quality can be harder to control. [10]

While being an easy to implement and use process, GMAW is easily affected by arc wandering. This effect increases surface roughness, especially on titanium alloys, which is the reason for rather using GTAW or PAW for this certain alloys. [11]

A special variation of GMAW is called Cold Metal Transfer (CMT) developed by Fronius. This method uses a high frequent forwards and backwards motion of the welding wire to achieve very little heat input into the surrounding material. Therefore, tolerance control and risk of spatter are significantly improved. [8, 13]

3. Plasma Arc Welding (PAW)

Like in GTAW, a wolfram electrode is used to ignite and constantly hold an electric arc to the substrate material. Additionally, plasma gas is used to stabilise and concentrate the energy input. Depending on the process, plasma gas and shielding gas can be identical (usually argon) or plasma gas mixtures can be used to further enhance properties like penetration and energy density. [10, 14]

Due to the highest energy density in this list, PAW is able to achieve high deposition rates while maintaining decent surface quality. [11, 14]

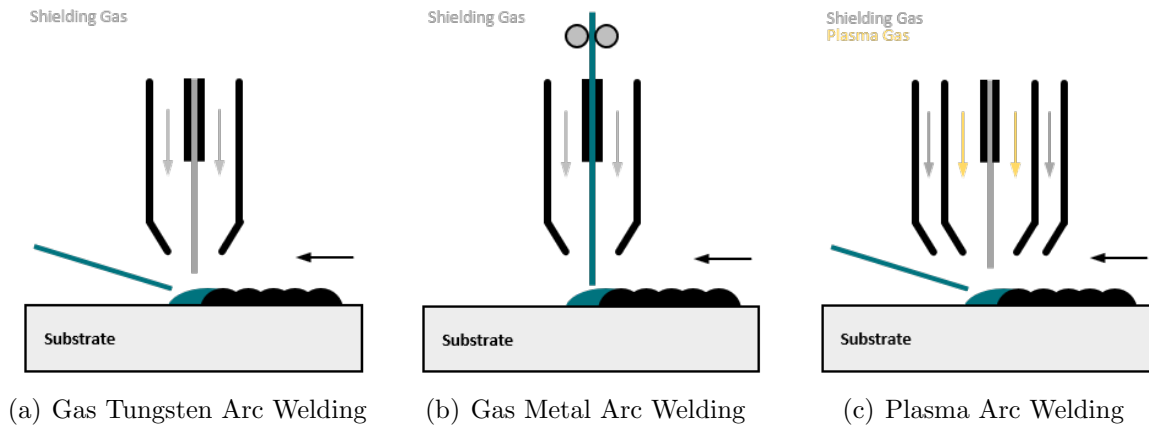


**Figure 2.1:** Schematic overview of welding technologies used in WAAM cf. [10]

Depending on the chosen welding technology and material combination, current pulsing or different polarity can be utilised for better weldability and overall quality. There are also a lot of gas mixtures from which can be chosen, depending on the welding property that needs to be improved. Shielding gas has a big influence on the weld pool's shape, penetration and protective functions, therefore a suitable mixture is vital for consistent results. [10, 15, 16, 17]

## 2.1.2 Parameters and Influencing Variables

In many cases, process parameters are linked to each other. By changing one parameter, others can be influenced in a way that the outcome is very different from previous settings. This correlation, and the fact that a change in process parameters also affects process planning and thus later FEA, make it very difficult to efficiently find ideal and universally applicable settings. [9, 17, 18]

### 2.1.2.1 Welding Current and Voltage

The basic controls on a welding machine are represented by current and voltage. While voltage is held constant in most cases, welding current has a significant effect on surface roughness and the overall heat input. Arc power controls the weld bead's geometry, spatter probability, penetration depth and mechanical properties. It is important to have enough power available to sufficiently melt the amount of fed material, while simultaneously avoiding excessive melting of the previous layers to ensure a minimum of distortion and geometrical deviation. [7, 9, 15, 17, 19, 20]



### 2.1.2.2 Wire Feed

Wire diameter and feed rate determine the material flow and thus limit the possible deposition rate. The feed rate also plays a major role in the weld bead's shape and size. Therefore, wire acceleration and feed velocity need to be controlled very precisely to achieve consistent results. [17, 19, 20]

As can be observed in Figure 2.2, the wire feed rate and wire diameter influence the width and depth of the weld pool, as well as the deposition height. However, the correlation between process parameters and wire feed is approximately linear due to conservation of volume, expect for minor geometric deposition artefacts. [17, 20]

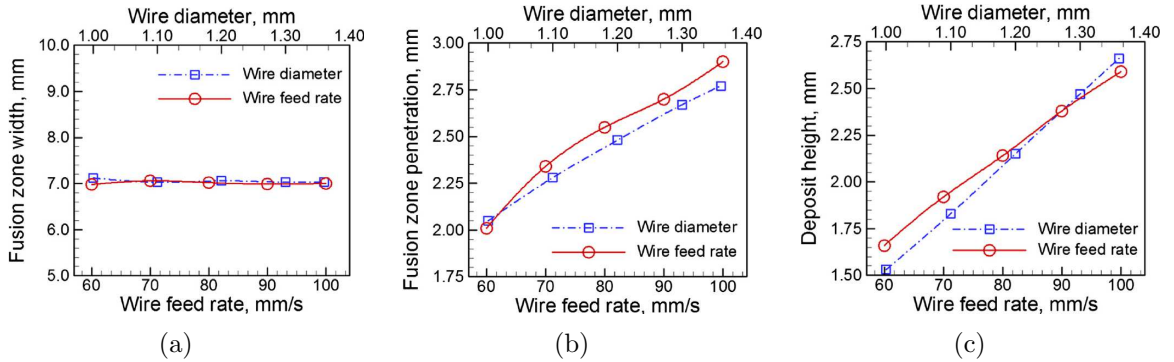


**Figure 2.2:** Weld bead parameters in dependence of wire feed rate and diameter [20]

### 2.1.2.3 Travel Speed and Build Strategy

When it comes to build strategy, three main categories (Figure 2.3) of deposition are possible in the layer plain: [7]

1. Single

When building thin walled structures, single bead deposition is chosen. [7]

2. Parallel

In contrast to thin walls, parallel deposition can be used to build thick walls when an enlargement of the used welding wire is no option. [7]

3. Oscillation

Similar to parallel deposition, this variant can be used to build thick walls or solid structures. It is found, that oscillating build paths improve the weld bead's flatness compared to parallel paths, which also increases process stability. [7, 19]

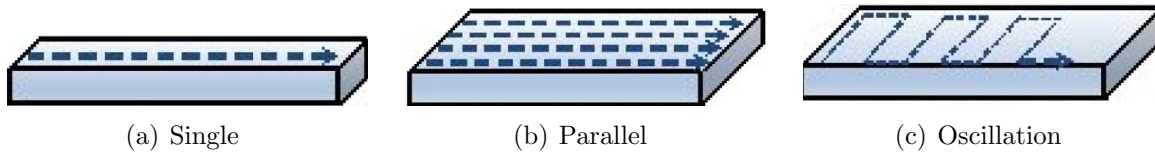


**Figure 2.3:** Possible in-layer deposition strategies [7]

A difference in layer quality can be noticed between the deposition directions. When the heat source is moved unidirectionally, inconsistencies in starting- and end points of the welded layers can be observed. This effect scales with the number of layers built. Therefore, bidirectional tool paths are used to balance out said effect and equalise heat distribution. [9, 18, 21]

#### 2.1.2.4 Shielding Gas and Atmosphere

For sufficient shielding, the gas flow of the torch is set to about 15 litres per minute or more, depending on its size. For better protection on special alloys, typically argon flooded containers are used to submerge and shield the whole welding assembly. [12, 22]

As previously mentioned in chapter 2.1.1, the shielding gas choice influences many welding parameters like weld pool shape, penetration and energy input. [10, 15]

#### 2.1.2.5 Heat Transfer and Thermal Radiation

Conduction to nearby structures, thermal radiation, as well as convection effects form the combined influencing variable of heat transfer. A consequence to those effects is the weld bead's shape and thus a critical variable for process control. In general, the thermo-physical behaviour of WAAM is more complex than in simple arc welding, because deposition conditions vary and temperature and cooling effects change with each layer deposited. [7, 11, 20, 23]

In manufacturing time stages, conduction is the dominant method of heat transfer in arc welding. Previous investigations however showed, that a significant temperature overestimation may occur in calculations which only recognise conduction. Therefore, some provided standard models using only conduction might be inadequate to deliver accurate cooling rates and resulting temperature fields, as shown in Figure 2.4. [11, 20, 22]

Although specific data for one experimental setup is described and absolute values can not be transferred directly, this illustrates a trend in general FEA of WAAM. It can be clearly seen in Figure 2.4(a) and 2.4(b), that cooling rates are influenced by arc power and travel speed. Wire feed and diameter seem to have no significant influence. What stands out is the serious difference of taking convection into account in thermal calculations. [20]

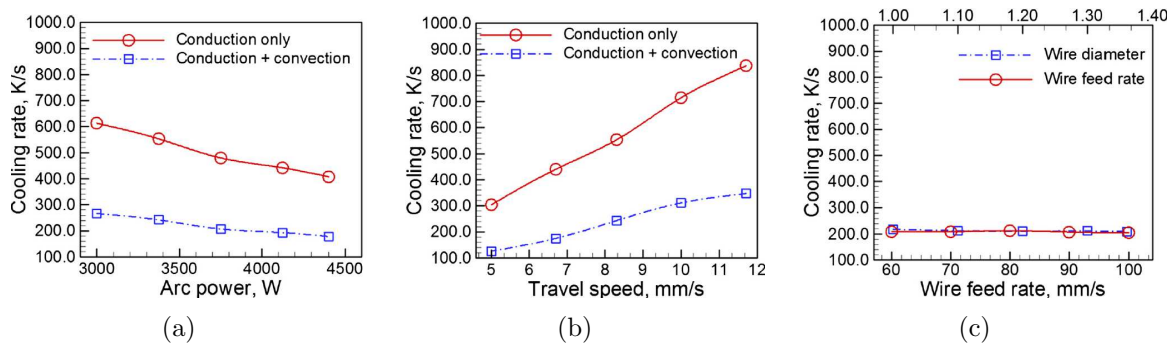


**Figure 2.4:** Cooling rate in dependence of different process parameters [20]

Cool down phases in between layer manufacturing steps are common to prevent overheating of the part. In this process stages, thermal radiation is the dominant effect for energy transmission. [22]

### 2.1.3 Opportunities and Challenges

Every process offers individual benefits over other solutions, however also downsides or rather complex challenges can be found. To summarise special opportunities and problems remaining in the current state of research, a quick overview is provided in the following.

#### 2.1.3.1 Operating Cost

Equipment cost can be counted as an advantage of WAAM. In general, inexpensive and field tested welding equipment can be combined with industry standard CNC machines. Spare parts and consumables are readily available worldwide and can be sourced from different manufacturers. Deposition rates are typically much higher than in laser based AM, with up to 10 kg per hour. Therefore, manufacturing time can be reduced drastically, which combined with relatively inexpensive consumables like wire, results in reasonable manufacturing cost per hour. [6, 11, 17, 18, 24]

Material efficient manufacturing of large parts for the aerospace industry possibly offers the largest field of application, as seen today. As part weight is an important sales argument, components are designed with lots of pockets, biometric structures and holes to optimise the load capacity to weight ratio. Therefore, a large amount of material would need to be removed from semi finished products by subtractive machining. This causes additional tooling cost and process time. Using WAAM allows to only build the needed material with a minimum of machining allowance for later surface finish and fits. [5, 7, 19, 25, 26]

### 2.1.3.2 Flexibility

Welding wire can be sourced in various sizes, qualities and alloys. This allows for a rather quick and material efficient change in the welding setup. Unlike powder bed technologies, only the substrate and welding wire need to be changed to process different materials. Complex and elaborate cleaning routines can mostly be eliminated and there is practically no waste or material that needs to be reprocessed. [5, 6, 15, 24]

### 2.1.3.3 Residual Stress and Distortion

Due to high cyclic temperature gradients and a non homogeneous heat distribution, residual stresses are unavoidable. During building, the current top layer obtains its main residual stress through shrinkage of the weld pool. Therefore, deformation stacks with each layer, amplifying bending moments (Figure 2.5) and thus the effect of warping and bulking when the clamping system is opened. In some areas, the local stress exceeds the material's yield strength and thus causes plastic deformation, which introduces distortion. Due to the accumulation of said distortion effects, unacceptable dimensional inaccuracy may occur over time. FEA can be used to minimise those effects and predict residual stress states of finished parts by taking various parameters into account. [4, 5, 7, 15, 22]

Pre tensioning through clamping mechanisms raises the total residual stress state in a part because of blocked thermal expansion. This further reduces the created part's load capacity and fatigue strength by benefiting crack propagation. [5]

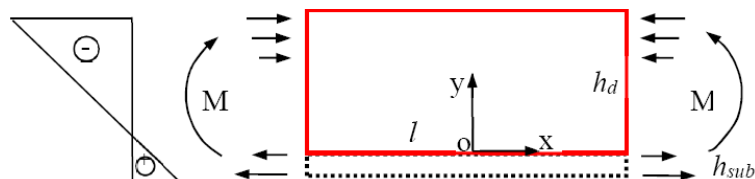


**Figure 2.5:** Planar bending moment introduced by accumulated residual stress [5]

#### 2.1.3.4 Process Control

There are various parameters to be considered in arc welding. Correct settings are vital to later part strength and fatigue behaviour. Rapid heating and cooling affects uniformity, possibility of hot cracks and propagates fatigue cracks. Welded metals also tend to change their physical properties when exposed to multiple rather uncontrolled and local thermal cycles, as may occur while building the layers. Therefore, parameter analysis and process simulation are one of the most difficult tasks in process control. [5, 16, 18, 22]

A lot of research has already been done, nevertheless WAAM remains a rather unstable process, especially regarding repeatability and error proneness. This can be attributed primarily to a lack of possibilities for closed loop process control and suitable non-destructive measurement devices. Manufacturing accuracy is also limited to certain levels: welding rod diameter, arc ignition procedures and bead geometry divergence, to name a few. As a result of the error accumulation through said examples, deposition control can be a problem. Especially considering a consistent layer height and the geometric requirements to successfully stack layers on top of each other. As the number of layers increases, the weld pool becomes larger in the plane of welding, but the layer height decreases. Therefore, current WAAM processes need to be improved regarding automation and feedback control. [6, 11, 19]

Software also plays a critical role in further improvement. Many process parameters need to be monitored and quality control should be done on a parallel basis to the process to ensure closed loop systems. Today, many quality related issues rely on human operators who need to manually control some process stages and choose parameters based on their knowledge. Sharp corners should be avoided or properly compensated, therefore special tool path algorithms might be needed. [6, 19]

#### 2.1.3.5 Simulation and Prediction

Thermo-mechanical FEA commonly requires great processing power, as well as a lot of time to compute, especially when large or complex parts need to be analysed. Additionally, when the accuracy of a model needs to be increased to fit deviation tolerances, the computation time increases drastically. This causes accurate FEA to be much harder to achieve in stable conditions, especially for larger components. [4, 5, 16, 22, 27]

Artificial Neural Networks (ANN) and Machine Learning (ML) are topic of current research in this field. They can be utilised to find correlations between input variables (process parameters) and the mechanical properties of manufactured parts. The prediction of residual stresses and deformation could possibly be simplified and automated parameter optimisation can be conducted. In general, a trend can be found that ANN promise better prediction accuracy compared to currently wide spread models based on mathematical regression and data fitting algorithms. [11, 16, 23, 28]

Another field of studies addresses microstructure formation and phase transformation from a molten weld pool to room temperature. Custom user routines are commonly used to describe material models, which are then implemented in thermo-mechanical analysis. This adds more computational steps for each time step and thus further increases calculation time. [16]

There are also mesh free approaches like the Element-Free Galerkin (EFG) or Diffuse Element Method (DEM), that try to avoid numerical problems related to complex re-meshing tasks by using smoothed particles. Originally derived from other industrial processes containing mainly machining operations, these solutions promise to be much more stable and time efficient. [16, 29, 30]

### **2.1.3.6 Defects and Quality Control**

In general, all AM processes are prone to a certain number of defect sources because of the applied layer by layer manufacturing technology. Porosity is one prominent example, but especially in arc welding processes, crack formation due to powerful heat cycles are a common quality problem. Since WAAM tends to be a solution for small individual batches with complex features, quality control is vital for a practical and economical use. [5, 6, 7, 15]

The wire surface quality, shielding gas content and concentration, as well as torch angle influence overall surface quality and likeliness for porosity. [15]

## 2.2 Ti-6Al-4V Properties in Arc Welding

For each material in arc welding FEA, there is a cut-off temperature. Essentially, mechanical properties remain constant or can not be measured accurately from this specific temperature onwards. As can be observed in Appendix A, for Ti-6Al-4V this point is reached at around 1700°C. [31, 32, 33]

For the sake of simplification, following paragraphs only focus on material parameters which show significant influence on numerical simulations and thus need further investigation to properly describe materials inside a simulation environment. Nearly every material property is dependent on temperature or pressure, therefore detailed descriptions are favourable for accurate analysis. [33, 34, 35, 36, 37]

Most software packages already provide well tried and tested values for many parameters. DEFORM<sup>®</sup> originates from metal forming and forging, therefore a broad material database exists for most common materials. The newly available AM module focuses on welding, which brings genuinely different properties and special features. This, and the fact that welding setups vary in technology and application, cause a lack of material description in some areas, which need user interaction to describe sufficiently. [38]

Another important factor to consider, after a stable FEA is established, is the microstructural behaviour. In general, grain structure differs from bottom to top of the weld bead, especially when in contact with the significantly colder substrate in the first layer. [18, 20, 36, 39]

Porosity usually raises internal stresses and thus shortens the fatigue lifetime proportional to pore size and amount. As basis for a porosity model in FEA, a non-linear isotropic kinematic hardening approach needs to be implemented as elasto-plastic material model. [40, 41]

## 2.3 Finite-Element Analysis of Arc Welding Processes

Considering FEA, WAAM can be described as a multi-layer arc welding process, accordingly many similarities can be used. In general, the heat source has the greatest influence on the outcome in arc welding. It influences distortion, heat input and distribution and bead geometry, which are vital parameters for accurate manufacturing. As a result of a complex geometrical shape and highly non-linear power distribution, as well as commonly occurring complex weld paths and weld bead shapes, suitable solutions with little deviation need to be found. Also the fed wire needs to be taken into account. Since the heat source generates heat by volume unit, specific element activation algorithms are used to subsequently activate the weld bead as the process progresses. [4, 16, 22, 24, 42]

Usually, the process is split into a thermal and subsequently conducted mechanical analysis, which calculates much slower in comparison. Results from the thermal analysis are saved for each element and calculation step. Those thermal fields can then be loaded into the mechanical analysis as boundary conditions. This is done to quickly generate results to fine tune settings. Only promising and stable thermal calculations are then processed as mechanical analysis to predict distortion and residual stresses. However, modern FE packages like DEFORM<sup>®</sup> can separate those calculation steps internally, which improves usability and user friendliness. Additionally and independently, analytical methods can be used to discretise the deposition process to describe complex sub depositions with discontinuous points. [4, 16, 23, 31, 38, 43]

Multi-layer arc welding simulations usually consume a lot of time, especially when calculating thermo-mechanical solutions. Specialised GPU-based computations promise an acceleration of this process and are subject to current research. [5, 23, 27, 31]

### 2.3.1 Thermal Analysis

As basis for combined analysis, thermal calculations need to be conducted. Besides heat transfer phenomena, this also includes melting and solidifying of the material. Usually, process data is acquired to iteratively enhance the replication of a real welding experiment. When a desirable deviation is reached, these optimised and tuned settings can be used to build the thermal model for further analysis. [16, 23, 31]

Commonly, an enthalpy based calculation method is used in this type of numerical problem because it is able to account for latent heat. Therefore, enthalpy  $H$  (2.2) is formulated by



modifying the equation of heat conduction in solids (2.1) to three dimensions. Material density  $\varrho$ , nodal temperature  $T$  and specific heat capacity  $c_p$  are needed to transition to an enthalpy based equation, which is then completed by taking heat conduction in form of the temperature dependent thermal conductivity  $k$  into account. [23, 32]

$$\frac{\partial T}{\partial t} = \frac{k(T)}{\varrho \cdot c_p} \frac{\partial^2 T}{\partial x^2} \quad (2.1)$$

$$\frac{\partial H(T)}{\partial t} = \frac{\partial}{\partial x} \left( k(T) \frac{\partial T}{\partial x} \right) + \frac{\partial}{\partial y} \left( k(T) \frac{\partial T}{\partial y} \right) + \frac{\partial}{\partial z} \left( k(T) \frac{\partial T}{\partial z} \right) \quad (2.2)$$

To consider phase changes and thus latent heat, the following equations describe solid (index S), transition (index T) and liquid (index L) states of the welded metal. Index 0 represents the reference point. Respective equations are applied below the temperature they are rated for. [16, 23]

$$H_S = \int_{T_0}^{T_S} \varrho(T) C_{pS}(T) dT \quad T < T_S \quad (2.3)$$

$$H_T = H_S + \int_{T_S}^{T_L} \left( \varrho(T) \frac{H_L}{T_L - T_S} + \varrho(T) C_{pT}(T) \right) dT \quad T_S \leq T \leq T_L \quad (2.4)$$

$$H_L = H_T + \int_{T_L}^T \varrho(T) C_{pL}(T) dT \quad T_L < T \quad (2.5)$$

Most prominent in arc welding, conductive heat transfer is considered as follows. Heat flow between solid objects is basically regulated by the temperature difference to a respective other node and the coefficient of heat transfer  $k$ . [16, 23, 44, 45]

$$Q_{cd} = k (T - T_0) \quad (2.6)$$

Next, heat transfer inside gases, like the prevailing process atmosphere, is calculated through the temperature difference and the coefficient of convection  $h_c$ . [16, 23, 45, 46]

$$Q_{cv} = h_c (T - T_0) \quad (2.7)$$

Lastly, radiation to the environment is applied in form of thermodynamic boundary conditions. The Stefan Boltzmann constant  $\sigma_r$  and material specific emissivity  $\varepsilon_r$  are needed for this calculation, the latter one can also be dependent on surface temperature. This type of heat transfer is especially dominant in cool down phases. [16, 23, 45, 46]

$$Q_r = \varepsilon_r(T) \sigma_r (T^4 - T_0^4) \quad (2.8)$$

It is indicated by experiments, that the molten pool remains stable during respective layers. Therefore, no additional steps need to be considered when modelling the heat source and the molten pool can be simplified. This also applies to moving heat sources, as long as they move in constant speed intervals. Those can be modelled by a pseudo steady state, which means that the fusion zone keeps its geometric dimensions and the temperature distribution stays constant. [32, 42, 43]

### 2.3.2 Mechanical Analysis

Depending on the chosen object model, elastic or elasto-plastic equations are used as fundamental principle for mechanical calculations. Thermal cycles result in a temperature field  $T$ , which induces expansion and contraction resulting in a displacement field  $U$ , which further translates to a local strain rate  $\varepsilon$  consisting of elastic, plastic and thermal strain. [16, 24, 45, 47]

$$\varepsilon = \varepsilon_e + \varepsilon_p + \varepsilon_{th} \quad (2.9)$$

Strain is connected to stress  $\sigma$  by Hook's law, written in matrix notation as  $D$ . [16, 47]

$$\sigma = D \varepsilon \quad (2.10)$$

By the introduction of the stiffness matrix  $K$  and the previously calculated temperature field  $T$ , a matrix equation resulting in thermal load  $R$  can be solved numerically. This operation consists of several very large matrices, therefore occupying much more computational power than simple thermal calculations. [16, 47, 48]

$$R = K_1 U - K_2 T \quad (2.11)$$

### 2.3.3 Suitable Elements

Depending on the problem's dimension, different element types can be used. In case of 3D analysis, there exist three common element types, as shown in Figure 2.6. The main difference of finite elements is their number of nodes and geometrical shape. Depending on the used Degree of Freedom (DoF) and trial function of an element, extra nodes can be placed on each line-symmetrical, increasing node count. [24, 45, 48]

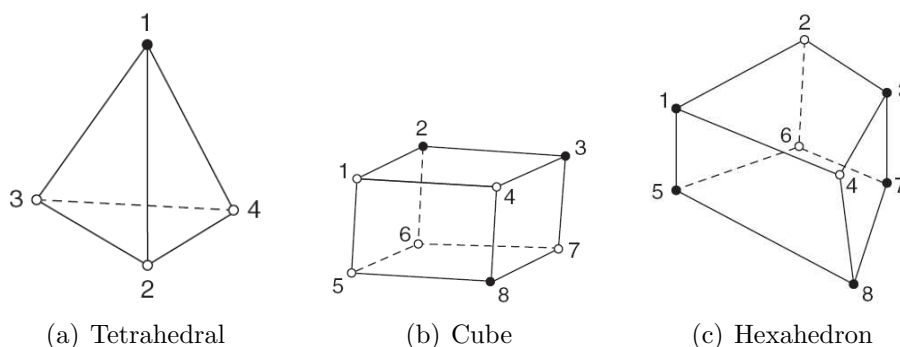


**Figure 2.6:** Possible elements for practical 3D FEA [48]

Tetrahedral elements can be used in a 4 node (TET4) or 10 node (TET10) configuration. Their computational performance is often inferior to other element types because a lot more elements are needed to mesh a structure. However, the big advantage of this element type is flexibility and ease of use. Meshing algorithms are simple and very fast compared to rectangular elements. Due to their triangular shape, they are also best suited to approximate complex parts without too much loss of geometrical information. Cuboidal elements are practically separated in 8 node cube elements (HEX8) and 20 node Hexahedrons (HEX20). [47, 48]

### 2.3.4 Mesh Structure and Creation

The basis of every numerical problem is discretisation. Therefore, the part's geometry is split into a set of areas with specific size and characteristics. Every calculation step represents a certain time jump in the real process. Like in numerical integration, the real world counterpart is approximated by activation of specific areas to represent the process advancement in respective time steps. This approach directly leads to finite elements and their sequential calculation, according to the correct activation strategy. [43]

Although FE software has improved and gotten robust over the years, limitations remain when generating fine static meshes. Mesh size correlates with analysis accuracy: the finer the mesh, the more resource intensive the computation gets. Core capacity in CPUs is a limiting factor for most users, resulting in a very time consuming process and thus compromises regarding accuracy. To encounter this problem, dynamic meshing strategies are being developed to locally refine the mesh in contact areas, while coarsening it in no longer actively used areas. [16, 22, 29]

Local mesh-refinement in the fusion zone and HAZ, as shown in Figure 2.7, are generally recommended due to high temperature gradients. [16, 23, 24]

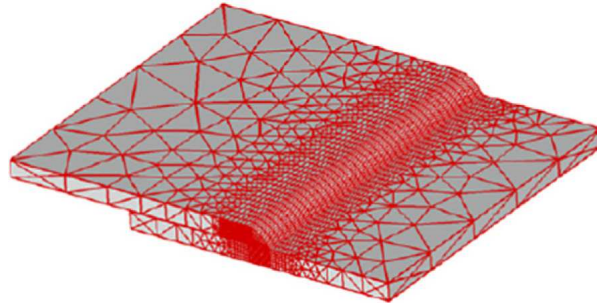


**Figure 2.7:** Reduced mesh with local refinement in the HAZ [23]

### 2.3.5 Weld Bead Models

Usually, a 3D model is sliced into  $n$  layers of vertical element groups, which represent the individual weld beads. Depending on different manufacturing parameters and attention to detail, different methods of modelling the weld beads were developed. [4, 11, 31]

It turns out to be a mayor challenge to effectively predict the layer height and overall shape of the molten pool, which significantly influences the weld bead model in FEA. In addition to established optimisation methods, statistics and ANN can be utilised to find correlations between deposition parameters and the resulting bead shape. [11, 17, 19]

#### 2.3.5.1 Solid Structures

When building solid structures, empty spaces between the perimeter walls need to be filled with welding wire. In theory, a tool path is calculated assuming ideal circumstances and a consistent cross section geometry. However, when placing weld beads parallel and close to each other, adhesion and shifting effects occur. This may result in material piling, risk of porosity and locally raised temperature gradients. To achieve optimal infill with a constant layer height, tool paths needs to be generated with shifted center lines (Figure 2.8), depending on welding parameters. Therefore, filler beads tend to be less wide as wall beads and energy input needs to be adjusted accordingly. For FEA, this results in a modified heat source model and a smaller mesh between the outer walls, adapted to infill width. [49]

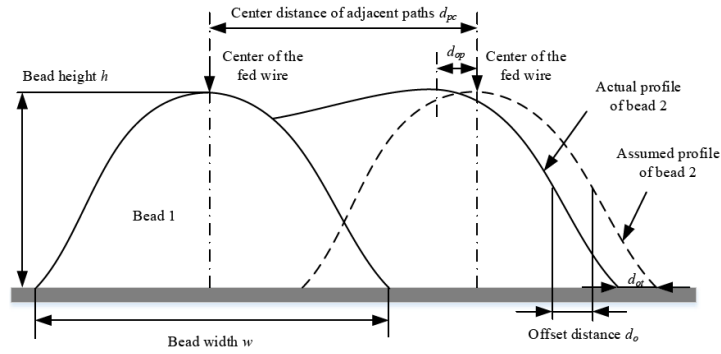


**Figure 2.8:** Deposition strategy optimised for solid infill with a constant layer height [49]

### 2.3.5.2 Overlapping Corners

Some problems arise when modelling sharp corners in thin walled parts because dynamic overlapping occurs in those areas. This does not only influence the weld bead's shape and thus geometry errors, but also local energy input into the mesh. A cross section profile is described by a parabolic function and tool paths are overlapped, resulting in an acceleration of the torch when approaching the corner, to expose it with the same amount of heat per travelled length as the remaining walls. This allows for a reduction in piled material and thus geometry errors in corners, as displayed in Figure 2.9. [19, 49, 50]

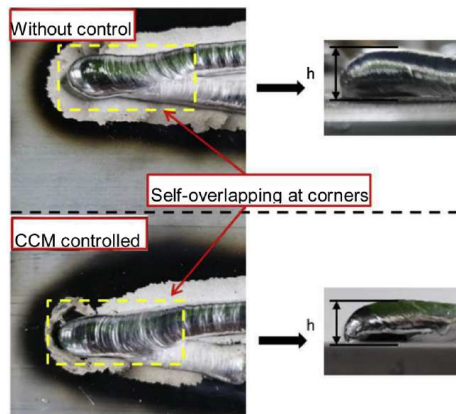


**Figure 2.9:** Experimental verification of the overlapping corner optimization [19]

Considering this circumstance in FEA can be difficult due to complex material flow. In any case, the exact machine movement data needs to be processed in the FEA environment. Therefore, this problem may only be solved with proper closed loop control and sufficient computational resources. Additional algorithms can be utilised to calculate offset distances of the welding wire to the tool path to prevent material build up on sharp inner corners. [19, 49]

### 2.3.5.3 Cross Section Models

A common approach to modelling welded layers is to simplify each layer with a rectangular cross section and then stack them over each other to build a wall. While maintaining easy to mesh and compute structures, this approach has some downsides considering geometrical accuracy and heat distribution. Since the real volume of each welded bead is a bit different and may vary in cross section form, a rectangular approximation tends to overestimate the amount of deposited material. This can lead to smaller deviations in heat capacity and therefore incorrect local temperature readings in FEA. Overall, the deviation is small in relation to the increase in calculation time and preparation effort, especially when considering 3D modelling of welded layers using parabolic or polynomial functions. Basically, there are three possible approaches to model weld bead cross sections, considering attention to detail and available data, shown in Figure 2.10. [4, 11, 19, 22]

Weld bead shape is primarily controlled by the wire feed rate and travel speed, therefore modelling can be reduced to the cross section of the bead perpendicular to the tool path, depending on the current time step. This is a rather simple and two-dimensional approach, therefore travel speed needs to be accounted for in time step size to ensure correct heat input. [19, 49]

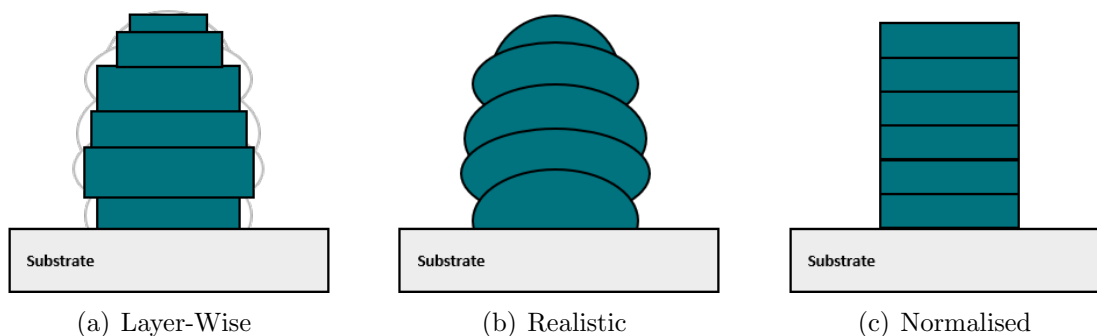


**Figure 2.10:** Schematic cross sections of weld bead modelling approaches

#### 1. Layer-Wise Rectangular Fitting

In this approach, every layer is treated as an independent object. This includes the geometry, material properties and manufacturing parameters. In terms of FEA, every layer needs to be imported, ideally by a specific user routine which also assigns properties. This procedure gets very labour intensive in setup, as well as computationally intensive due to the manual layer separation, independent meshing and coupling of previous layers. Further challenges arise in raw data gathering:

Layers can be approximated as rectangular cross sections with different height and width, according to predictions through the deposition settings. More elegantly, this would be solved with in-process surface measurement of the weld bead, which represents an additional data source and measurement challenge. However, this approach provides the big advantage of accurate modelling and a possible in-process prediction and correction of final part properties. When processing power and measurement abilities are provided, this is by far the best approach considering retrofitting as well as prediction possibilities. [22]

## 2. Realistic Geometry with High-Detail Mesh

When live measurement data is not available, this approach can be used to retrofit the FE model to the experiment. By surface scanning the welded model, it becomes possible to accurately model the weld bead. The so found final geometry can then be meshed with a very detailed grid size to fit universal heat source movements, therefore creating a layer free model. Because in the real process no ideal rectangles are formed, it becomes necessary to replicate the exact torch movement over time, which includes differing layer heights and deposition settings according to detailed process log data. Although possibly very accurate, this model suffers from the big downside of predictability. Because the final geometry is needed, it becomes nearly impossible to set up models in advance for prediction studies. Additionally, detailed log-files are needed to recreate the experiment, which are not always available.

[4, 11, 51]

## 3. Normalised Rectangular Approximation

Similar to the realistic model, this approach can be used in case of a lack of process data or resources for a digital shadow. In contrast, this approach models the ideal output generated by the provided g-code movement of the machine. All layers are modelled as rectangles with the same layer height, which increases compatibility with already existing slicing strategies in FE software. If process parameters are varied mid-process, normalisation routines need to be conducted. To achieve this, every layer is extracted from g-code to calculate predefined process parameters like travel speed, deposition rate and thermal cycles. By comparing the predefined values with ideally assumed properties of the model, its inner properties like density or thermal conductivity can be modified to equalise properties. This can also be done through heat source parameters to correct the specific heat input per volume unit. [4, 22, 51]

### 2.3.6 Heat Source Models

For thermal analysis, a volumetric heat source model based on the induced thermal field is usually used to describe the temperature gradient and shape of the weld pool. Power distribution can be quite complex, depending on the mathematical model behind the heat source. To successfully and accurately predict residual stresses in welded structures, the temperature field caused by the heat source needs to be determined as close to reality as possible. However, the more accurate the heat source is described, the more computational effort needs to be put in, which leads to difficult optimisations, providing sufficient accuracy while maintaining a simple heat source model. [16, 22, 23, 24, 52]

Computational Fluid Dynamics (CFD) analysis offers the possibility of detailed heat source observation and optimisation. Since many volumetric heat sources used to date are inaccurately described, said analysis can even be necessary to achieve suitable results. However, this approach is often avoided because of its very long simulation times. Even in simple cases, the computation can claim several days on dedicated clusters. [23, 30, 43]

In general, heat source models are distinguished by their order of dimension. In practical applications there are three major types which can also be combined together: [22, 52]

1. Unidimensional

Point models are a very primitive way to describe heat sources. Essentially, a point in space is assigned with the heating power.

2. Two-Dimensional

Also called surface models only describe the shape of a used heat source in the horizontal weld pool plane. This method is suitable for the simplified analysis of low energy density welding processes, which do not penetrate deeply into the material.

3. Three-Dimensional

So called volumetric models cover all three cartesian coordinate directions, and therefore are able to map the weld pool's geometry in high energy density welding processes like GMAW, PAW or laser welding. As a result of their complexity and increasing number of parameters, task specific calibration needs to be conducted. They also take much longer to compute compared to simpler models, which can be a limiting factor for large part FEA.



### 2.3.6.1 Rectangular Model

As simpler alternative to the Goldak Double Ellipsoid (GDE), a rectangular heat source model is suggested in combination with simplified rectangular bead models to improve computation time by sacrificing accuracy regarding the fusion zone. [4]

### 2.3.6.2 Goldak Double Ellipsoid

The double ellipsoid equivalent heat source is particularly used in arc welding FEA. Goal of this model is to distribute the heat source's energy to an exact weld pool volume. This approach also shows disadvantages considering the fusion zone and accuracy around the weld seam. Therefore, custom modifications need to be conducted to compensate for deviations in energy density. It was initially derived from the Gauss function and further refined into quarter-ellipsoids (Figure 2.11) to account for different metal flow in the front and back of the weld pool. [24, 52, 53, 46]

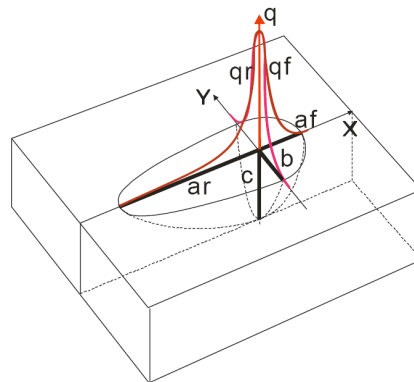


**Figure 2.11:** Schematic diagram of the GDE and its parameters [52]

To describe the heat source, at least four geometric and two energetic parameters are needed. Geometry parameters are usually extracted from measurements of the weld pool's shape through experiments and simulation aid. Additionally, two energetic parameters are needed to determine the energy distribution between front and back. However, this approach may lead to cases where the calculated weld pool temperature raises above the evaporation point in the weld pool's center, as well as way too low on the edge. It is also rather resource intensive to mesh, which can lead to longer computational time on large scale parts. [22, 24, 52]

### 2.3.6.3 Goldak MR10 Modification

Due to problems regarding the correct temperature distribution in GDE models, a modification was conducted by Makrov et al. using a function of the tenth power to describe energy density distribution better. This approach promises to fix the problem with Gaussian distribution, which characteristic property is a distinctive maximum in the center. As experiments showed, this is not always the case with real arc welding heat sources, especially considering hydrodynamic effects in the weld pool. Therefore, an additional form parameter  $\lambda$  is introduced to flatten the peak, as demonstrated in Figure 2.12. For electric arc welding  $\lambda > 2$  is suggested to generate realistic results. [52]

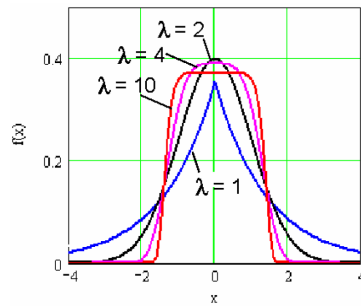


**Figure 2.12:** Influence visualisation of the introduced form parameter  $\lambda$  [52]

Considering FEA accuracy and thus the exact balance of mass and energy when adding welding wire, not only the bottom quarters of the ellipsoid shall be used. Instead, the upper half (coloured section in Figure 2.13), which contacts the weld bead mesh emerged from wire feed, has to be recognised for correct energy input. [52]

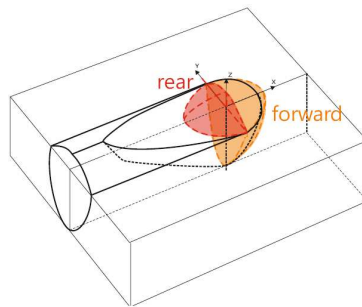


**Figure 2.13:** Elliptical consideration of the energy input of the added weld bead [52]

The so found results are promising to improve the accuracy when compared to conducted welding experiments. Temperature and thus energy distribution can be simulated with more realistic results and less calibration effort. However, it is suggested that the found

solution for GMAW might not be suitable for general application and further adaptation might be needed, depending on the exact process and welding setup. [52]

### 2.3.6.4 Goldak Rectangular Modification

There are two options to consider the power transfer into the weld pool. First, direct transfer from the heat source to the base metal. Second, the wire melting enthalpy considering droplets. Combined with an element activation strategy, this choice is vital for correct results. Up to 50% of total power input is attributable to the fed wire melting. This approach combines the GDE for power transmission to the substrate and a custom developed rectangular model (Figure 2.14) to consider the energy transfer into the weld bead. [24]

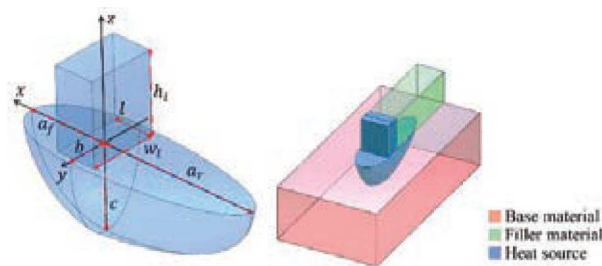


**Figure 2.14:** Rectangular consideration of the energy input of the added weld bead [24]

To assign the correct amount of energy to bead elements, a calculation based on the feed rate is conducted. It is also crucial to match the activation box with weld bead geometry to ensure no energy is distributed in empty space. [24]

### 2.3.7 Element Activation Strategies

When material is melting, the local heat generated is negative. In case of solidification it will be positive. This circumstance demands further considerations in the activation strategy to avoid convergence problems. There are two main characteristics to be mentioned: [24, 27]

#### 1. Quiet Elements

Originated from welding FEA, all deposited metal elements are present throughout the procedure. They are assigned very small thermal conductivity and Young's modulus values to minimise their influence when not needed. Properties can be switched to normal as the heat source passes.

### 2. Inactive Elements

In contrast to quiet elements, inactive elements have no properties at all. They are activated by algorithms when the heat source passes them. Therefore, initial values can be assigned at the time of activation and no heat up process is required.

Recently developed hybrid quiet-inactive elements promise a reduction in processing time, as well as an error reduction considering energy input to heat up pure quiet elements. There are also mesh coarsening strategies to simplify already activated and no longer contacted elements to further reduce computational time compared to a static mesh. [22]

#### 2.3.7.1 Activation by Temperature Gradient

As the heat source passes the inactive element structure, they are activated by exceeding a certain trigger temperature which can be set in advance. [24]

#### 2.3.7.2 Activation in Layers

Layer-wise activation can be combined with other strategies to further reduce the amount of active nodes in the FEA setup and thus improve on computational speed. [22]

#### 2.3.7.3 Activation by Heat Source Volume

For each calculated step, intersections between the heat source and mesh are calculated. Elements are considered as intersection, if their center point lays inside the heat source's volume. The so found elements can then be activated and assigned with properties. On the other hand, elements which were considered active in the previous calculation step and no longer lay inside the control volume are deactivated. This procedure occurs before every other calculation of the current time step to prevent incorrect heat transfer. [43]

When inactive elements are activated, they need to be assigned with properties. Usually those properties are seen as process parameters to replicate real welding circumstances. For example, upon activation, nodal temperatures around 1500 °C are typical for modelling recently added material. [31]

As found in [1], depending on the used FE software, the use of dummy heat sources might be necessary to achieve an activation of the whole weld bead's width without the need of user routines in DEFORM<sup>®</sup>.

### 2.3.7.4 Hybrid Quiet-Inactive Method

Described by Ding et al., a unique hybrid approach is suggested to simplify element activation and reduce the number of active nodes to improve performance. In this method, elements are categorised in three groups. The schematic procedure in FEA can be seen in Figure 2.15. On every time step, the method is repeated and element states are assigned according to the following rules: [22, 43]

1. killed

Elements which describe already deposited material, also known as weld beads. They were active elements in a previous time step and maintain all physical properties for the rest of the process, therefore they are considered kind of quiet. This type of elements can also be combined with mesh coarsening strategies to further reduce the amount of active nodes in no longer active areas of the manufactured component.

2. active

Elements which are in touch with the volumetric heat source in the current time step and thus are transitioned from inactive (no physical attributes) to active. This means, that physical attributes are assigned to them corresponding to the heat source's properties.

3. to be activated

Elements which are initially meshed in a static grid and considered inactive. They have no physical properties and thus do not influence heat distribution at all.

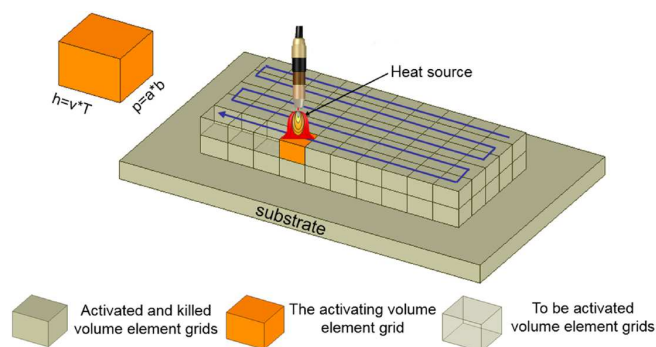


**Figure 2.15:** Schematic representation of hybrid element activation [22]

It is also important to follow the rule of correct time load. The length of active elements divided by the travel speed of the torch results in the propagation speed of the heat source. This parameter needs to be empirically determined for every welding setup to achieve the correct heat input per time step. [22]

## 2.4 Statistical Design of Experiments

Experimental design is a tool that utilises statistics to establish and afterwards conduct a structure of tests. A key element of statistical analysis is the systematic change of defined input parameters to later observe corresponding changes in output values. This is especially important for the identification and optimisation of most impactful parameters to the output in technical applications. [53, 54, 55]

Design of Experiments (DoE) is a versatile tool to identify the important parameters to a problem. Due to its general non-problem related statistical approach, it can be universally applied in many research fields. [54, 55]

### 2.4.1 Procedure

First, a to be optimised process with associated input parameters needs to be analysed. Parameters which are subject to change in this process need to be defined with lower and upper limits, which may be reached in the variable window under consideration. In the next step, the found input variables need to be analysed for complexity. Depending on the problem, a suitable design method needs to be chosen in order to generate a beneficial outcome. Applying a statistical method to the given problem will then provide a matrix containing a minimum of meaningful support points necessary to describe the problem properly. [53, 54, 56]

Previously, many applications were described binary, for example within or without specification of manufacturing tolerance. The novel approach by Taguchi introduces a description by deviation, which defines an optimum point of outcome. Every deviation from this point is analysed: the closer the observed output point is located to specification limits and away from optimum values, the bigger the error. This enables quantification and measurability of error size and thus optimisation to minimum variation. [54]

After the generated variation matrix is conducted in real experiments, the phase of analysis is reached. A combination of mathematical approaches and statistics, like regression or non-linear optimisation, are used to optimise the outcome values of the observed process. [54, 55]

### 2.4.2 Opportunities

In general, statistical DoE opens up possibilities to change multiple variables at once, according to statistically important support points found through the various possible design methods. This enables a minimum testing effort approach to find the most suitable input parameters and obtain the desired output. [53, 54, 56]

DoE also shows the interaction and relation between input and output parameters, which may be used to find the most influential parameters for later optimisation studies. [53, 55]

### 2.4.3 Applications

One prominent example widely used in industry is cost optimisation. Cost centers and components needed when manufacturing a certain product are listed as input variables. Then an experiment is designed to minimise the output, which in this case would be the overall manufacturing cost. [54]

Process parameter optimisation in all industrial processes can be subject to statistical analysis. Minimising the input of chemical components in reactors while containing a certain yield, maximising yield in complex mixing recipe calculation or hitting targeted control values in processes, for example a certain temperature level, are common task definitions. [54]

### 2.4.4 Statistical Approaches and Design Methods

As previously described, the selection of the most suitable design method turns out to be the most critical step in statistical analysis. Depending on complexity and the number of introduced input factors, different models may be beneficial to use regarding the desired outcome. [54, 55]

It lies in the nature of things that some variables are controllable while others are not. When building a robust design, uncontrollable variables are introduced as system noise. Generally speaking, it is beneficial to reduce the amount of uncontrollable parameters and maximise the ones controlled by the user. [54]

In FE modelling of arc welding, there are a lot of boundary conditions and contact variables which need to be considered and exactly determined to minimise the overall noise and maximise informative value. Those variables are considered uncontrolled most of the time, but by keeping them as constant as possible in experimental setups, they become less of a problem. [55]

### **2.4.4.1 Full Factor Variation**

In this approach, all parameters are written in a big table to generate rows in which only one parameter is changed with regard to the starting point. Analysing one value at a time is the natural approach for many problems and the most detailed one, however in most cases turns out to be the least efficient because of its huge resource expenses. This might also be called full factorial design, which represents an extreme case of the usually more efficient factorial method. [54, 55]

### **2.4.4.2 Factorial Combination**

The factorial method assigns a factor for every parameter, which are then subsequently changed. This method can be run on two or more levels, depending on the varying parameters. In contrast to the one factor at a time method, this approach offers to reveal the impact of one parameter at several levels of other factors. Basically, one parameter is chosen to be the level dominant factor, which dictates the number of rows in the combination matrix. One level equals to one iteration step of said parameter, so if parameter A shall be observed at 5 different values, the level will be 5. These levels then get combined with all other parameters, written in each column with their own levels. The combination of all these parameter levels results in the required amount of test runs. It is necessary to apply this method when interactions between parameters are present to avoid misleading outcome, for example in serially coupled mechanical devices. [55, 57]

For variance analysis, ANOVA is prominently used in many cases, as well as desirability analysis for optimisation. This type of method is primarily used for level 2 investigations, which means that every parameter can be either „minimum“ or „maximum“. [58]

### **2.4.4.3 Response Surface Regression**

One of the most commonly used methods in welding is Response Surface Methodology (RSM) with central composite design (CCD). It is very suitable for the relationship and



influence analysis of input parameters to a single output parameter of a process. The basic prerequisite for this approach is a single or a set of output (or response) parameters and a set of independent influencing variables, also known as process parameters. It also offers the advantage of a graphical representation of the output values. [39, 55, 56, 59]

Within this method, it is possible to describe each input parameter with a linear or polynomial model, which further enables the search for theoretical optimal parameters by performing a subsequent optimisation step. The big advantage here is that only a hand full of support points are needed to fully describe each input parameter to a sufficient probability, which makes it overall very accurate while retaining minimum testing effort. [53, 55, 59]

This method can be used in a wide variety of complex technical applications with a good success chance compared to design effort. Quadratic models can be fitted in three ways, as visualised in Figure 2.16. For general and accurate models, circumscribed approaches (CCC) are most suitable. [55, 60]

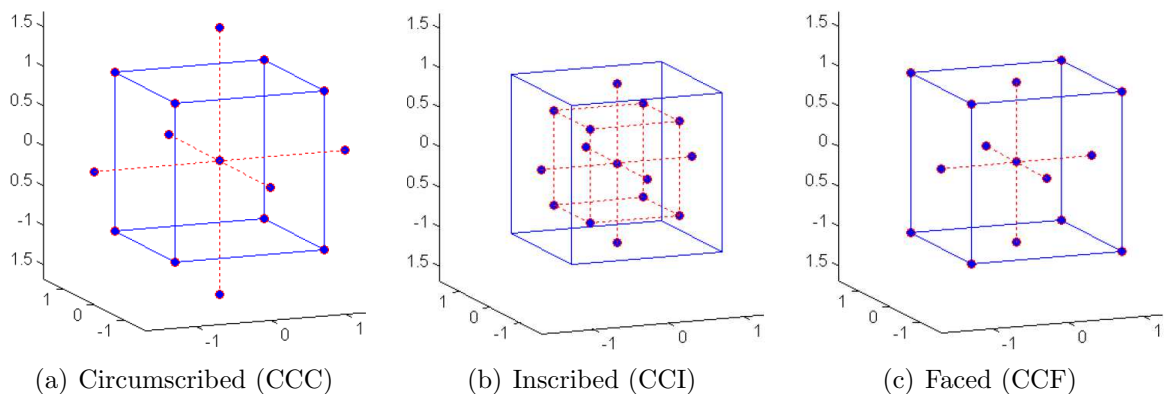


**Figure 2.16:** Central composite design methods for quadratic response surface models [60]

#### 2.4.4.4 Box-Behnken

Similar to RSM, this method is used to describe quadratic models. However, this approach offers a special feature: by avoiding the corners of a quadratic space, extreme and thus unlikely combinations are avoided, as visualised in Figure 2.17. Therefore, this design needs less runs to provide sufficient data than central composite designs, under the circumstance that extreme factor combinations are not present in reality, which needs to be assumed by experience or detailed process knowledge. [55]

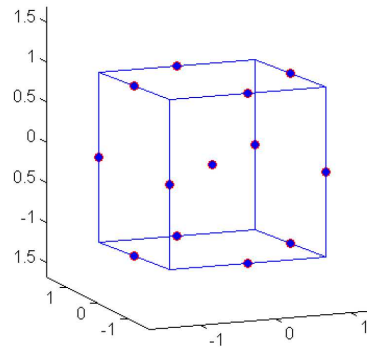


**Figure 2.17:** Visualisation of the Box-Behnken quadratic model [60]

RSM in general have to deal with problems regarding multiple output variables because differentiation between the responses is not trivial. For optimisation regarding single output parameters to certain values, this model is very effective because of the fewer test runs needed for sufficient informative value. [55]

#### 2.4.4.5 Taguchi Orthogonal Array

Proposed by Dr. Taguchi in [61], this design utilises orthogonal arrays to add another dimension to conventional central composite designs. It has proven to produce high quality products and therefore is in frequent use by the automotive industry. As previously stated, also this design suffers from problems regarding multiple output parameters. [55]

To conduct this design, a suitable orthogonal array needs to be chosen, depending on the number of input factors. The then calculated combinations and test runs need to be executed and analysed for optimum parameters. As last step it is suggested to perform one or multiple confirmation runs with the evaluated optimum parameters. This might be necessary to further refine those parameters, because deviation from the real optimum is not guaranteed to be small. When data is noisy, uncertain or incomplete, Taguchi strongly recommends to use signal to noise ratio analysis for optimisation. [55]

One big disadvantage is the given simplification regarding the interaction of parameters, which leads to fewer test runs but at the same time increases uncertainty. Also the results obtained by Taguchi's method are relative and do not directly indicate which parameters influence the experiment most. This fact also makes it impossible to account for dynamically changing processes, like simulation studies with multiple input parameters. [55]

### 3 Numerical Modelling of the Experiment

In this thesis, DEFORM<sup>®</sup> version 12.1 is used to replicate a manufacturing experiment to create the basis for further evaluation and comparison. Therefore, the subsequent chapters will describe the process of setting up a stable FEA for later optimisation steps. The overall goal is not to perfectly replicate the conducted experiments, but rather to find solutions for a universal prediction method in FEA for future manufacturing jobs.

#### 3.1 Experimental Setup

A rectangular single wall is to be manufactured from Ti-6Al-4V wire and substrate in a total of 32 layers, with two subsequent preheating passes. For reference and rough orientation, the experimental setup can be observed in Figure 3.1, the exact measurements of each component can be found in Table 3.4.

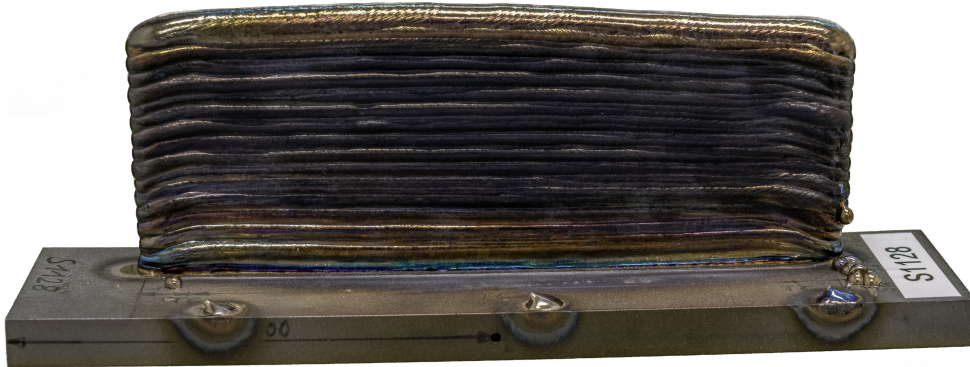


**Figure 3.1:** Picture of the manufactured single wall

Since a simple single wall is built, the axis wise travel information is kept rather simple: the torch moves bidirectionally between  $X = 0$  mm and  $X = 147$  mm, generating an effective torch travel length of  $l_{travel} = 147$  mm. Additionally, the z-coordinate value is increased at each turning point by the individual layer height. The wall is built with  $y_{shift} = 5$  mm out of the substrate's center line on the y-axis to ensure enough distance to thermocouples, as shown in Figure 3.2, therefore changing the temperature distribution in the substrate to asymmetric. Clamps are placed on the center line of the substrate, which needs to be considered in modelling.

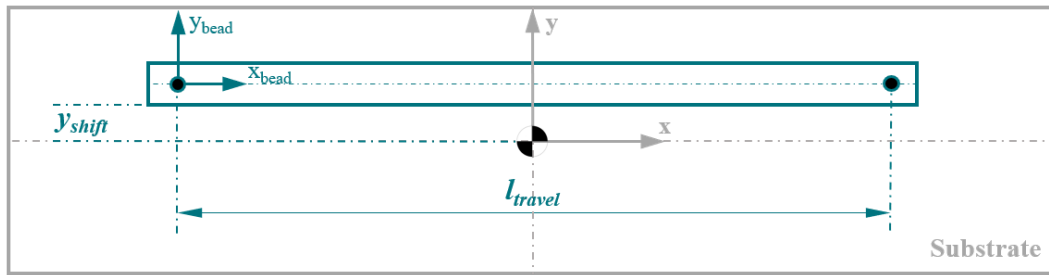


**Figure 3.2:** Visualisation of coordinate and movement setup in the single wall experiment

An argon atmosphere is contained by a gas-tent fixed to the manipulator and a box frame around the workpiece, to ensure below 100 % of O<sub>2</sub> content throughout the process and therefore prevent oxidation.

### 3.1.1 Temperature Measurement

Thermal data is captured with four type J thermocouples positioned on the substrate according to dimensions shown in Figure 3.3. One thermocouple (TC4) is also placed inside a small hole drilled 9 mm deep into the substrate’s side surface center to gather information of the internal temperature deviation. Unfortunately, no in-layer measurements were taken due to the complex argon tent setup, which limits access for personnel and space around the welding setup for thermocouple insertion mechanisms. Surface thermocouples are fixed in place by small welded on wire loops, which were bent over the cables. Thermocouple tips are directly exposed to the atmosphere, no shielding measures were conducted.

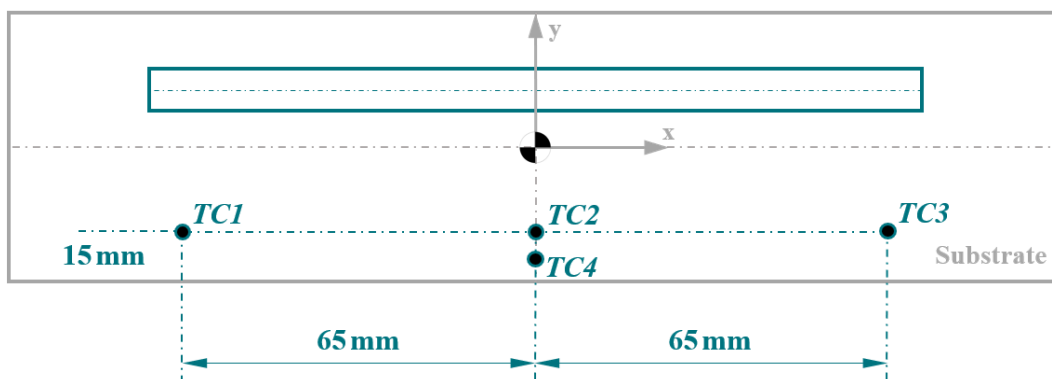


**Figure 3.3:** Visualisation of the thermocouple placement on the substrate top surface

### 3.1.2 Process Data

Machine g-code is provided to extract the layer based settings for deposition, welding strategy and travel speed, as shown in Table 3.1. Hard coded timings like dwell time, where wire feed is already activated without the torch moving, and other delay times can be read out of this information too, as documented in Table 3.2.

**Table 3.1:** Log-File torch information

Layer No.	Feed $\frac{\text{g}}{\text{min}}$	Speed $\frac{\text{mm}}{\text{min}}$	Current A
Preheat	0	300	130
1	29	200	140
2-3	21	160	140
4	21	200	130
5-10	21	240	130
11-32	21	280	130

**Table 3.2:** Log-File timing information

Name	s	Description
delay start	0.5	heat source on
pre-feed	1	wire feed on
delay end	0.5	heat source off
cooldown	30	nominal cooldown

Manual changes made throughout the process to ensure process stability are not saved in the log-file. This means that the exact layer times, individual layer heights and possible live height corrections are not documented.

## 3.2 Data Preparation and Methodic Implementation

Basically, there are three possible approaches to model WAAM in this application, described in chapter 2.3.5. Based on the attention to detail and available data, a normalised layer approach shown in 2.10(c) is chosen for further proceeding.

### 3.2.1 3D Modelling

A manufacturing job is tendered according to the dimensions displayed in Table 3.3 and visualised in Figure 3.4. As can be observed, the dimensions from Table 3.4 show that real components are often characterised by deviations in the geometrical accuracy, as well as several unknown measurements like the individual layer height.

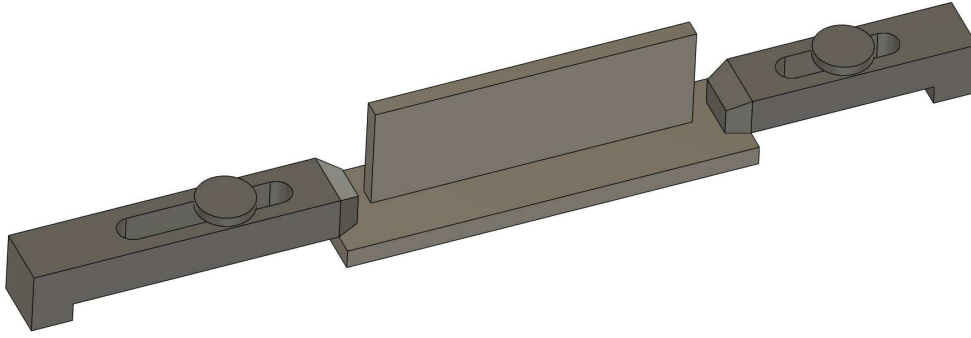


**Figure 3.4:** 3D model of the to be manufactured single wall

**Table 3.3:** Target dimensions of the to be manufactured single wall model

Target Dimensions	$x$ mm	$y$ mm	$z$ mm
Wall	155	8	50
Layer	155	8	1.563
Substrate	200	50	10

**Table 3.4:** Measured dimensions of the finished single wall and their variation

Real Dimensions	$x$ mm	$y$ mm	$z$ mm
Wall	156	8.4	53.4
Layer	150 - 156	7.6 - 8.4	1.1 - 1.8
Substrate	200	50	9.9 - 10.2

The part's target dimensions are used to generate a base model for FEA, which brings the huge advantage of universal application on any manufacturing job. To compensate for differences in geometrical dimensions, the heat source's power input, or inner properties like density need to be manipulated. By adjusting the absolute heat input per layer dynamically, the energy input per volume unit can be fitted to those of the normalised layer model by comparing the real deposition data to the modelled layer volume.

### 3.2.2 Extraction of Individual Layer Times

The provided raw data is not sufficient for exact modelling because pause times were manually extended in several layers due to reasons described in chapter 2.1.3.4. As stated in the provided log-file, every layer is programmed with certain feed and speed rates, as well as defined delays and cool down cycles. However, documentation and in-process trouble shooting often cause longer delay times at the end of a layer, resulting in deviations from the provided data. To compensate for the missing total layer times, a MATLAB<sup>®</sup> script was written to extract local extremes from the most stable surface thermocouple TC2, which will be further used as thermal benchmark. In Figure 3.5, local maxima are marked with circles and local minima with squares.

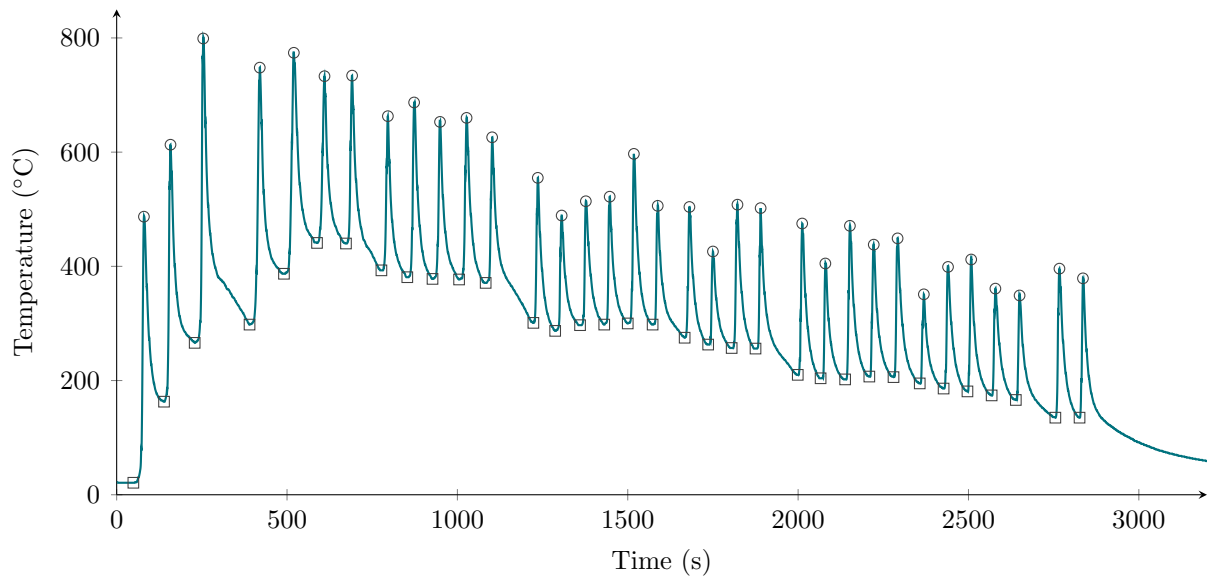


**Figure 3.5:** Layer timing extraction from the raw temperature data of TC2

Real layer times are extracted from the provided thermal history by determining the time differences between local minima. This is permissible because even the slightest heat input (re-activation of the heat source) is noticeable in thermal history.

```
for i = 1 : height( lows ) - 1
    layerTimes(i) = lowID(i+1) - lowID(i);
end
```

In a similar way, the nominal layer time is calculated by using the given hard coded timings from the log-file, mentioned in Table 3.2.

```
for i = 1 : height( lows )
    nominalLayerTimes(i) = pauseStart + feedDelay + weldTimes(i) + ...
        powerDelay + pauseEnd;
end
```

The total individual layer duration is visualised in Figure 3.6 and compared to nominal layer times, which highlights the importance of fundamentally correct machine data. It is to be noted, that both preheat layers are numerically treated the same as welded layers, therefore producing 34 layers for further handling.

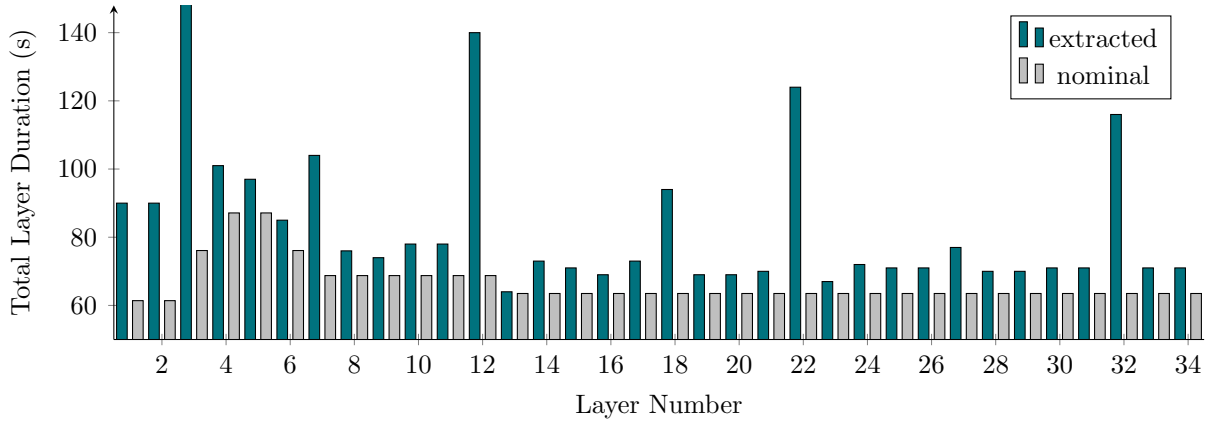


**Figure 3.6:** Layer duration differences resulting from manual interventions

### 3.2.3 Layer Model

The walls are approximated with rectangular shapes but welding wire naturally melts into spherical geometries, therefore it becomes necessary to account for the running volume of molten wire at start and end dwell times, where the heat source is active but no movement is executed. The travel length and physically generated wall length are not the same, as illustrated in the top view provided in Figure 3.7.

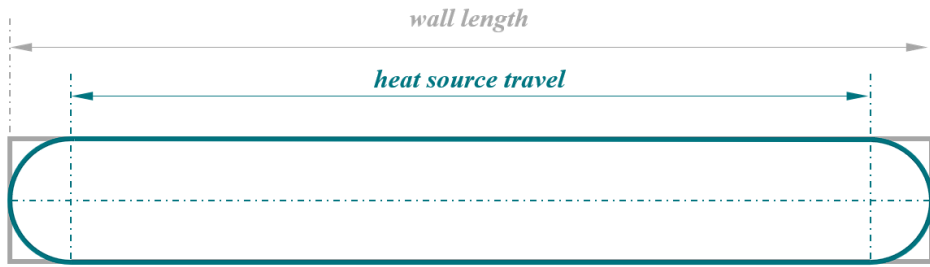


**Figure 3.7:** Modelling of the fed and molten wire volume in a welded layer

The wall is approximated by an ideal cuboid, representing maximum dimensions in each coordinate direction. As can be also observed in Figure 3.7, the start and end points of the weld beads are assumed by a circular cross section, therefore adding half of the weld bead's width  $b_{norm}$  as radius in length on either end of the x-axis travel  $l_{travel}$ , which was previously extracted from the log file.

$$l_{layer} = l_{travel} + b_{norm} \quad (3.1)$$



With this information, the cross section area of the layer can be calculated.

$$A_{layer} = l_{layer} \cdot b_{norm} \quad (3.2)$$

In the final step, a normalised layer height needs to be determined to conclude the volume.

$$h_{layer} = \frac{h_{wall}}{N_{layers}} \quad (3.3)$$

$$V_{layer} = h_{layer} \cdot A_{layer} = h_{layer} \cdot [(l_{travel} + b_{norm}) \cdot b_{norm}] \quad (3.4)$$

The described calculation is integrated numerically in MATLAB<sup>®</sup> by utilisation of the normalised 3d model dimensions previously shown in Table 3.3.

```
normLayerHeight = geom.normHeight / weld.nrLayers;
normLayerVolume = normLayerHeight * geom.normLength * geom.normWidth;
```

### 3.2.4 Wire Feed Strategy

Travel speeds, feed rates and pause times can be extracted from the machine code. This has the great advantage of exact timing in FEA, which offers accurate cooling and heating cycles - a key component for representative models, as described in chapter 2.1.2.2.

Every step in the log-file describes a heat source movement from point  $P_n$  to  $P_{n+1}$  by calling absolute cartesian coordinates and the associated travel speed. As visualised in Figure 3.8, the so travelled distance  $d$  can be calculated by applying the pythagorean theorem. Further, the needed time interval  $t$  can be determined to extract a weld time for each individual layer.

$$d = \sqrt{x^2 + y^2 + z^2} \quad (3.5)$$

$$t = \frac{d}{v} \quad (3.6)$$

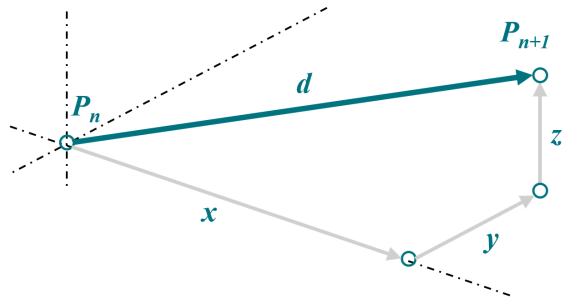


**Figure 3.8:** Description of movement in machine code

To get information about the total volume of deposited wire, hard coded feed delays need to be added to the previously extracted individual weld times. This information is crucial for the later assembly of the heat source model, which needs to differentiate between dwell times at the beginning of a layer and continuous feed.

```
Layer.weldTime = (geom.beadTravel ./ weld.speed) * 60;
Layer.feedTime = Layer.feedDelay + Layer.weldTime + Layer.powerDelay;
```

The activation volume will be fixed on the heat source's midline by default, which either causes gaps in the activated weld bead at reversal points, or incorrect heat input. It is not permissible to simply adjust the travel length to fully activate a layer because the absolute heat input as well as travel speed are falsified, adding up on the list of avoidable inaccuracies. Therefore, a strategy is developed to simulate material flow in dwell stages, as visualised in Figure 3.9.

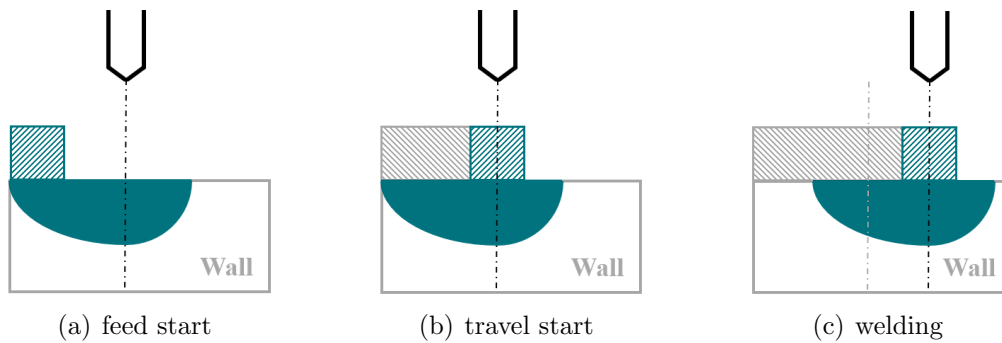


**Figure 3.9:** Visualisation of the implementation strategy for wire feed at reversal points

The green scraped square represents the position and size of the activation volume, the grey scraped rectangle represents the already activated layer volume. As can be clearly seen in the transition from 3.9(a) to 3.9(b), the start and end points of the weld bead are formed by molten material flow, not by heat source movement. Only in the last step, shown in 3.9(c), the activation volume is coupled to the heat source and they move together, as commonly conducted in arc welding FEA.

#### 3.2.5 Arc Power Normalisation

As the real deposition volume differs from the theoretically needed layer volume, due to normalisation in evenly spaced layers, heat input per volume unit needs to be compensated. It is chosen to correct the welding power according to the real deposition volume, and therefore generate a perfectly rectangular wall in FEA with correct energy distribution.

Target deposition in grams is calculated by multiplying the previously obtained unified layer volume by the density of Ti-6Al-4V . In reality, the deposited volume depends on the feed time and wire feed speed of the respective layer.

```
targetDep = normLayerVolume * (Ti64.density * 10^-6);
realDep = (feedTime / 60) .* weld.feed;
```

As basis for normalised power, the Deposition Difference Factor (DDF) is introduced. By comparing the target deposition to the real deposition for each layer, it becomes possible to calculate the needed energy difference. Nominal power, calculated from electrical power and thermal efficiency, will be reduced by the DDF to correct the energy input per volume unit in FEA to the same heat input per volume unit as in the real experiment.

```
ddf = targetDep ./ realDep;
weldPower = weld.voltage .* weld.current .* weld.eta;
redPower = weldPower .* ddf;
```

For simplification in the FEA setup considering the need of a different heat source for each layer, the magnitude setting for heat sources is utilised. By finding the largest power per layer and dividing the reduced power array by this maximum power, percent magnitude values can be obtained for each layer. Enabling the use of a single heat source with maximum settings and adjusting its power by applying a magnitude function over time. The results of this calculation can be observed in Figure 3.10, where the reduced magnitude is plotted according to the deposition difference impact.

```
weldPowerCalc = max(redPower);
magWeld = redPower ./ weldPowerCalc;
```

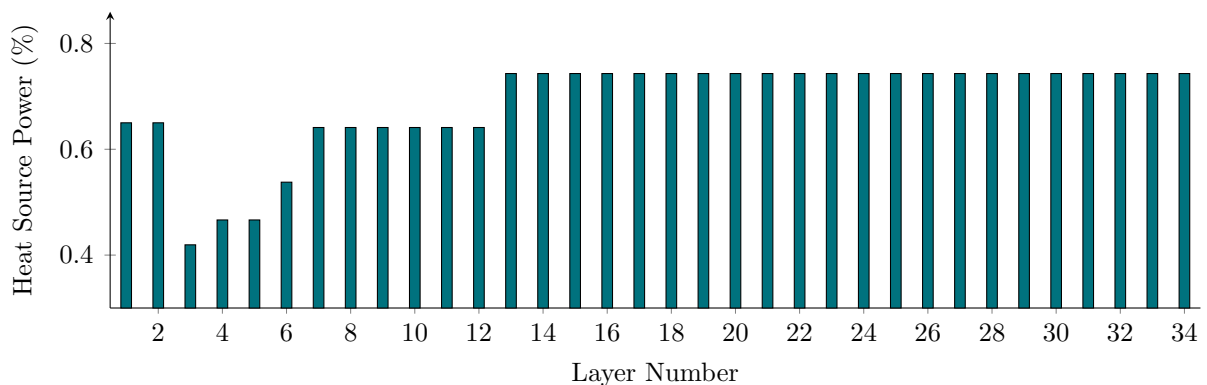


**Figure 3.10:** Reduced heat source magnitude according to deposition difference

### 3.2.6 Activation Volume

As found in previous research studies [1], the activation volume in DEFORM<sup>®</sup> is modelled as a cube with  $2 \cdot h_{Layer}$  in length and placed in the heat source's center, therefore activating one layer height of volume in each direction normal to the movement path, as described in more detail in chapter 2.3.7.3. When the weld bead's width exceeds this dimensions, dummy heat sources need to be introduced to cover the remaining cross section. For this purpose, heat sources with empty power and geometrical parameters are generated and assigned the same activation size as the main heat source. For automatic placement and movement calculation, a fitting code is written in MATLAB<sup>®</sup> which finds the number of necessary dummies to cover the weld bead under the condition of  $1.5 \cdot h_{Layer}$  as maximum size to ensure sufficient overlap. The so found dummies are then placed evenly across the weld bead's width and converted to y-coordinates for later movement calculations.

```
sizeDummy = 1.5 * normLayerHeight;
if (geom.normWidth / normLayerHeight) - floor(geom.normWidth / ...
    normLayerHeight) > 0
    nrDummy = floor(geom.normWidth / sizeDummy) + 1;
else
    nrDummy = floor(geom.normWidth / sizeDummy);
end
ySep = (geom.normWidth / 2) - (sizeDummy / 2);
yDummy = linspace(-ySep, ySep, nrDummy);
```

### 3.2.7 Time Synchronised Process Control

The pre-processor in DEFORM<sup>®</sup> calls for a number of tables to describe the heat source's movement, pause and ignition times, mesh generation intervals and time step size. Although not every parameter needs to be defined and can be left to be interpreted automatically by the software, it is highly favourable to do so. By creating one large constraint and time synchronised table of parameters, it becomes possible to identify and group strategic sub-processes. This allows for the optimisation of pause times by drastically reducing the number of calculation steps in those phases, as well as a precise prediction of sub-processes in the pre-processing environment. Every time the process parameters are changed, a new DEFORM<sup>®</sup> operation block needs to be inserted. By importing pre-processed parameters and settings, manual labour and error possibilities can be effectively reduced. Furthermore, the opportunity of automated user routines for importing is opened up.

When setting up a GDE heat source, described in chapter 2.3.6.2, DEFORM<sup>®</sup> calls for 4 geometrical parameters, 2 power parameters and different timetables. Parameter sets may

be revisited in chapter 4 for optimisation. Timetables however need to be pre-defined to describe the heat source's overall behaviour in 3D space. Three tables are needed:

1. Movement

Every available heat source model is defined around a center point, which can be moved in 3D space over time. To control movement speed and the overall welding path, a table containing all three coordinate positions over time can be loaded.

2. Magnitude

By definition, this parameter describes the intensity of a statically defined heat source model. Similar to the thermal efficiency coefficient  $\eta$ , the magnitude can be defined between 0% and 100% to manipulate the overall energy input. This is especially useful in pause times, because the magnitude can be set to 0% to switch off the heat source, avoiding a new sequence for each layer.

3. Orientation

When welding in wave patterns or planes which differ from the horizontal plane, an orientation vector can be used to define the direction in which the welding torch and therefore the electric arc is pointing. However, in this experimental setup, all welds are conducted in the horizontal plane, where orientation can be set to parallel to the z-axis for the whole process duration.

For table generation, a MATLAB<sup>®</sup> script is set up. All important parameters can be addressed in the same loop by subsequently adding time stamps. In the first step, a bi-directional movement strategy needs to be addressed.

```
for l = 1 : (weld.nrPreheat + weld.nrLayers) % layer index l
    if mod(l,2) == 1 % layer number is uneven
        dir = 1; % direction sign positive
    elseif mod(l,2) == 0 % layer number is even
        dir = -1; % direction sign negative
    end
```

In the main step, cases are created according to the information gathered in chapter 3.2 to subsequently add time stamps. This approach ensures that all tables share the same timeline, which makes them compatible and flexible for adjustments.

```
for d = 1 : 5 % delay index d
    switch d
    case 1 % start delay
        t = t + Layer.startDelay(l);
        magM = magWeld(l);
        magP = 0;
```

```
case 2 % feed delay
    t = t + Layer.feedDelay(1);
    xActiv = xMain;
case 3 % welding
    t = t + Layer.weldTime(1);
    xMain = xMain + (dir * geom.beadTravel);
    xActiv = xMain;
    xPilot = xMain;
case 4 % power off delay
    t = t + Layer.powerDelay(1);
    xActiv = xActiv + (dir * geom.normWidth/2);
    magM = 0;
    magP = magPilot(1);
case 5 % cooldown time
    t = t + Layer.cooldown(1);
end
```

At the end of each layer, a shift by one layer height is performed for all heat sources.

```
if l > weld.nrPreheat
    zMain = zMain + normLayerHeight;
    zPilot = zPilot + normLayerHeight;
    zActiv = zActiv + normLayerHeight;
end
end
```

### 3.2.8 Introduction of Dynamic Step Size

DEFORM<sup>®</sup> allows to import tables to dynamically control the step width in areas of high precision or interest. Similar to timetables explained before, this works by assigning a time in seconds per calculation step for certain time frames, as visualised in Figure 3.11 at the end of this procedure.

Thermocouple measurements are logged in 1 s intervals, therefore FE log time  $s_{log}$  is adjusted to the same for optimal comparability. Additionally,  $f_{sub}$  is introduced as a subdivision factor which splits the log interval in fractions for higher resolution. Since thermal analysis will converge with very rough step sizes, a suitable upper limit needs to be found empirically. In this case it is also limited for reasonability by the thermocouple log time, which explains a factor of 1. However, for later mechanical analysis, time steps need to be much smaller to ensure convergence of the FE solver.

Furthermore, a cool down interval is introduced to potentially safe calculation steps in process times where no welding is conducted.

```
sLog = 1;    % time interval to be exported and saved [s]
fSub = 1;    % deviation factor for deformation analysis
sCool = 10;  % cooling phase time interval [s]
```

To generate time zones with different duration times, a step function is implemented between the transition points from the welding to cooling phase.

```
for l = 1 : (weld.nrPreheat + weld.nrLayers)    % layer index l
    for d = 1 : 4                                % step index d
        switch d
            case 1 % initialise step
                t = stepID{l,1} - 0.01;
                c = sCool;
            case 2 % welding phase
                t = stepID{l,1};
                c = sLog / fSub;
            case 3 % initialise step
                t = stepID{l,4} - 0.01;
                c = sLog / fSub;
            case 4 % cool down phase
                t = stepID{l,4};
                c = sCool;
        end
    end
end
```

The timetables for preheating and welding can be filled with duration values according to the previously generated data points along the step function.

```
if l ≤ weld.nrPreheat    % preheat from row 1 until end
    tempID = (4*l)+d-3;
    stepPre(tempID,1) = t;
    stepPre(tempID,2) = c;
else                    % welding from row 2 until end
    tempID = (4*(l-weld.nrPreheat))+d-3;
    stepWeld(tempID,1) = t;
    stepWeld(tempID,2) = c;
end
end
end
```

Now the minimum number of preheat and welding calculation steps needed to finish the analysis can be calculated. This is especially convenient for DEFORM<sup>®</sup> operators who need to define a finite number of steps for each section added in pre-processing.

```
for i = 2 : height(stepPre)
    if mod(i,2) == 0
        nrStepsPre = nrStepsPre + ((stepPre(i,1) - stepPre(i-1,1)) * ...
            (1/stepPre(i-1,2)));
    end
end

for i = 2 : height(stepWeld)
    if mod(i,2) == 0
        nrStepsWeld = nrStepsWeld + ((stepWeld(i,1) - ...
            stepWeld(i-1,1)) * (1/stepWeld(i-1,2)));
    end
end
```

The results of this operation can be observed in Figure 3.11, where a higher step duration means lower time resolution and therefore less calculation steps.

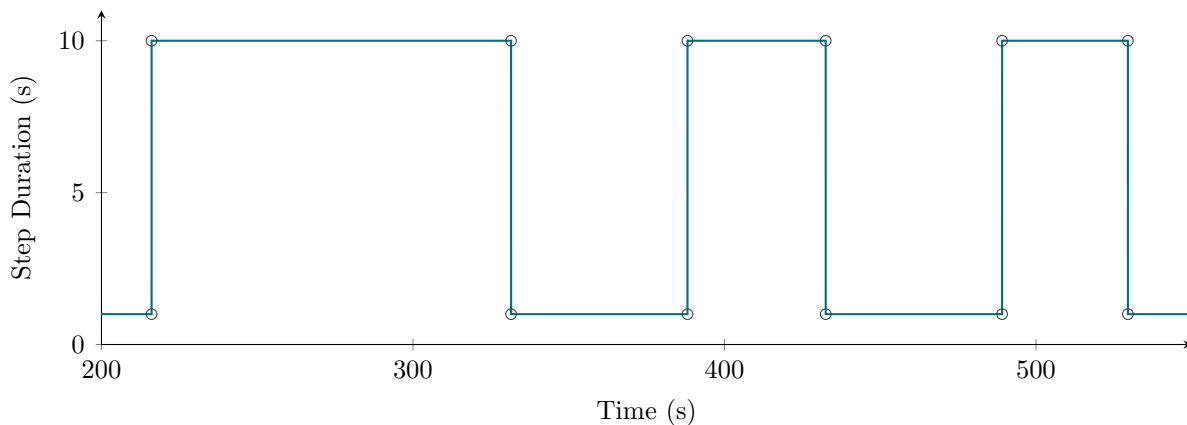


**Figure 3.11:** Dynamic time step duration control while welding

### 3.2.9 Detailed Material Model for Ti-6Al-4V

As described in chapter 2.2, the material model provided in DEFORM<sup>®</sup> is often limited in arc welding due to missing temperature dependent data. Therefore, an improved material model is proposed. Tabular data for the density, specific heat capacity and thermal conductivity is extracted from [62]. The work of Hocine et al. [37] also brought up a model for a temperature dependent emissivity by Yang et. al [63], as well as measurement backed thermal expansion data.

The collected models and tables are put together using MATLAB<sup>®</sup> for convenient exporting in desired sub steps. This way a temperature dependent unified table can be generated,



which can then be interpolated exactly. All exported data points of the needed processed parameters can be found in Appendix A.

The new model was tested on previously conducted experiments [1], as visualised in Figure 3.12. The same contact and boundary conditions were used and the temperature curve went down a little bit, which fits the experimental measurement better. However, peaks are still too high, which might be an issue with experimental setup and isolation in the first place.

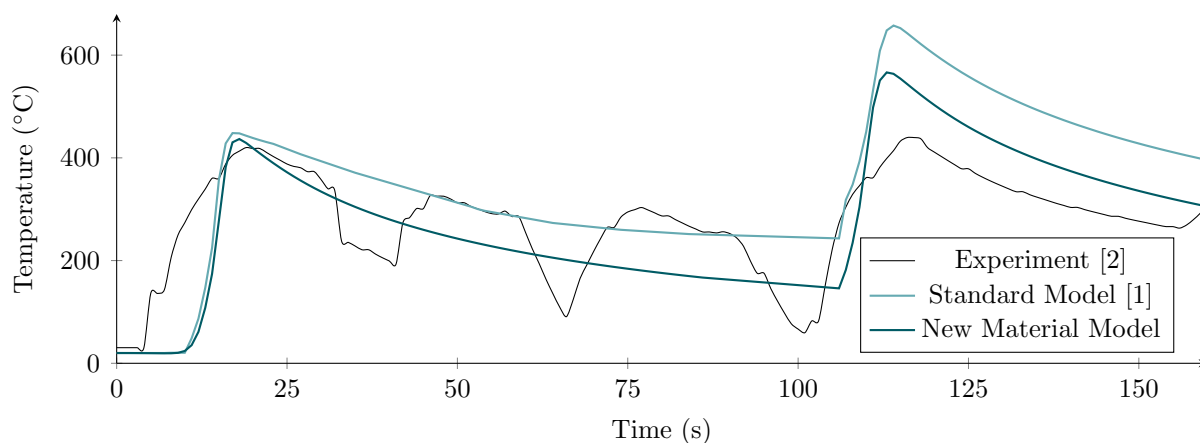


**Figure 3.12:** Validation of the proposed material model with previous investigations

### 3.3 Pre-Processing in DEFORM<sup>®</sup>

Thermo-mechanical analysis generally takes much longer to compute than thermal analysis alone. Since thermocouple measurements are used as reference data, only thermal analysis is conducted in the following experiment to reduce the processing time. After later optimisation steps, a full analysis may be conducted to gather information about the resulting distortion and residual stress state.

#### 3.3.1 Geometry

Due to the chosen implementation of normalised layers with a constant layer height in chapter 3.2.1, the internal slicer provided in DEFORM<sup>®</sup> can be used to automatically generate layers based off the entire wall's geometry. A separate import and handling of single layer objects can therefore be eliminated, which helps a lot considering the additional effort utilising subroutines for importing or manual labour.

The fixture table is modelled in its full thickness and with some space left around the mounted hardware. This was done to account for a realistic heat distribution and therefore thermal latency through the table’s thickness. Additionally, the clamps are modelled in great detail to provide exact thermal radiation surfaces, as well as the correct contact surface of the nut and clamping block to directly apply clamping forces. All so modelled geometries loaded in the pre-processor are listed in Table 3.5.

**Table 3.5:** Maximum dimensions of all generated 3D objects inside DEFORM®

Object Name	x mm	y mm	z mm
Wall	155	8	50
Substrate	200	50	10
Clamp long	160	30	32
Clamp short	tet	30	32
Table	600	200	30

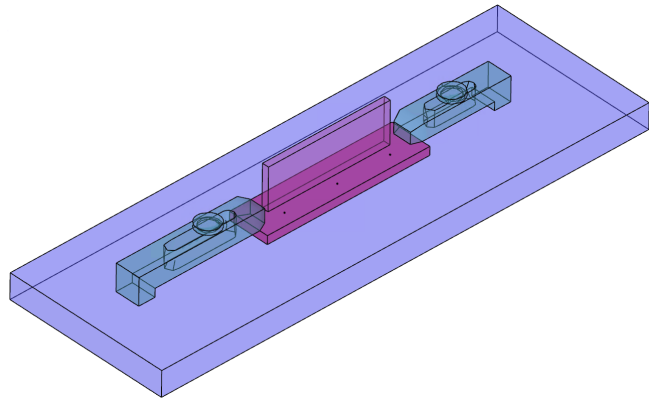


**Figure 3.13:** Visualisation of geometry placement in DEFORM®

### 3.3.2 Meshing

In FEA, it is critical to choose economical element settings to minimise the calculation time while maintaining sufficient numerical accuracy. Therefore, mesh size was initialised on a trial run with 1 mm and a size ratio of 1 on every object to gather benchmark data. Afterwards, the mesh of a single object was subsequently coarsened until deviations to the benchmark run became visible in the temperature response. The so determined maximum coarse mesh sittings are displayed in Table 3.6 to enable the possibility of later recreation.

DEFORM® natively only supports a tetrahedral mesh for AM structures because the built in slicer can not handle cube elements. Therefore, the wall can only be meshed in tetrahedral structures with a mesh size equal to the chosen layer height. Clamps are also meshed as tetrahedral because of their rather complex shapes. The substrate and table could be meshed using cube elements and therefore potentially save some nodes. However, it is chosen to use a tetrahedral mesh on all objects for convenience and optimal contact interaction.

**Table 3.6:** Mesh information for all objects involved in the analysis setup

Object Name	Type	Ratio	Size mm	Elements	Nodes
Wall	tet	1	1.5625	189871	36233
Substrate	tet	1	2	90628	20241
Clamp long	tet	2	5	2737	773
Clamp short	tet	2	5	2108	580
Table	tet	1	30	1616	498

### 3.3.3 Calculation Steps

The process is split in three steps, which are realised in DEFORM<sup>®</sup> by inserting different „General 3D“ operation blocks, as visualised in Figure 3.14. This is necessary due to changing geometrical heat source parameters between the operations. As no bodies are removed or added mid-process, all objects are initialised in the first operation and passed through to the subsequent operations as needed.

1. Preheating

The heat source is turned on with reduced power settings and moved along the future building path in both directions. This procedure ensures adequate preheating, good weldability and thus lower residual stresses. It is important to note, that torch height above the substrate plate is kept constant at  $h = 10$  mm.

2. Welding

Now that the substrate is preheated, welding can be executed. Here the heat source is turned on at full power and the wire is fed into the created arc. To build a structure, the welding torch is moved bi-directionally, as the layer height is subsequently added to the movement path.

3. Declamping

The welding clamps and table are removed. This enables the now connected substrate and wall to deform freely, as it would happen in reality when the clamps are loosened to remove the finished part from a machine. To achieve this, 6 calculation steps with a dynamic step size are set up to find convergence.

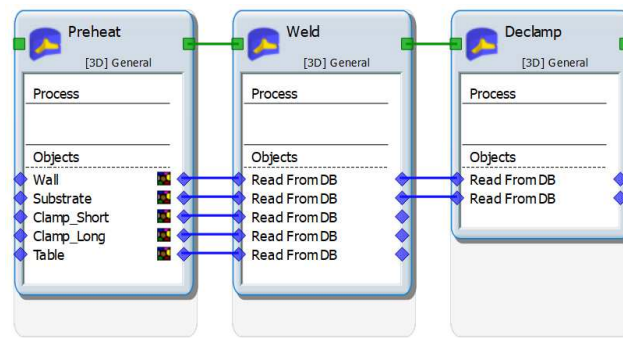


**Figure 3.14:** Visualisation of operation blocks used to model the welding process

### 3.3.4 Boundary Conditions

Depending on what lies in focus of the analysis, different approaches can be used for boundary conditions. In general, there are contact conditions, object material behaviour and thermal conditions. In the following, the process of finding suitable boundary conditions is presented.

#### 3.3.4.1 Material Behaviour Model

When objects are set up as rigid bodies, which is often done for convenience in clamping systems, deformation and possible residual stress build up can be falsified. However, convergence problems caused by contact node shifting can be avoided this way. Contrary to this, there are elastic or elasto-plastic material models, which allow for deformation to occur. This of course is the more realistic and accurate approach, however often comes with problems considering FE solver convergence and an overall increase in calculation effort. In pure thermal analysis, rigid bodies can be utilised to simplify the setup, because deformation analysis is not conducted anyway.

Since thermo-mechanical analysis shall be used later on in this setup, all objects are modelled as realistic as possible to ensure accurate measures of residual stress and deformation in the end. This means that the substrate and wall are set up as elasto-plastic and the welding clamps are set up as pure elastic bodies. The fixture table can be assumed as rigid body for stability reasons and overall no expected deformation.

#### 3.3.4.2 Heat Transfer To Atmosphere

Initially,  $k = 0.02 \frac{\text{N}}{\text{mm}\cdot\text{s}\cdot\text{K}}$  is used to describe heat transfer to the surrounding atmosphere in DEFORM<sup>®</sup>. However, this is a general assumption for air without flow. Since an argon

atmosphere is used inside a gas tent with a certain volumetric flow,  $k = 0.05 \frac{\text{N}}{\text{mm}\cdot\text{s}\cdot\text{K}}$  is estimated for more realistic heat transfer settings. As contact surfaces, the green selections in Figure 3.15 are chosen for all important bodies. In both cases, the bottom most surface not seen in this illustration is not selected for environmental contact, because of the direct heat transfer through body intersection.

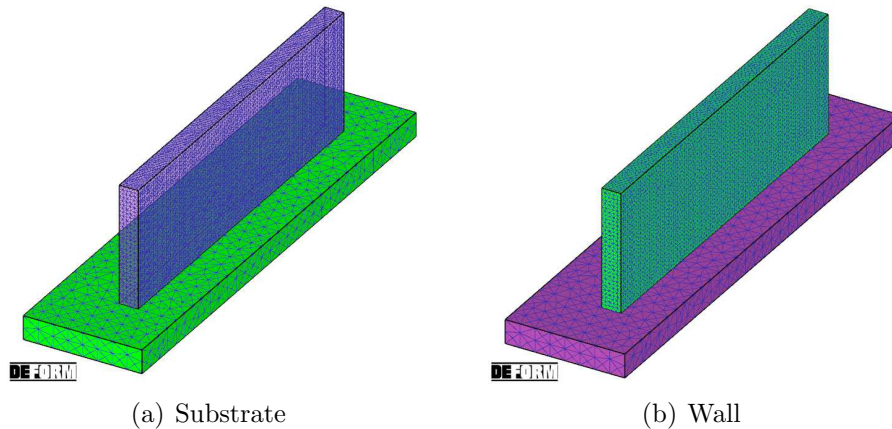


**Figure 3.15:** Example for surfaces involved in thermal convection to the environment

### 3.3.4.3 Contact Properties

General contact needs to be established for every pair of bodies which interfere. The standard contact setting calculates the node collision between objects for each step, because surfaces may change due to deformation throughout the process. This greatly influences stability and makes it harder to estimate thermal conduction settings because contact areas may change dynamically. This characteristic difference between contact modes needs to be noticed when choosing the heat transfer coefficient  $k$  to realistically depict the experiment.

Bodies are modelled deformable, as mentioned in chapter 3.3.4.1, convergence problems may occur in numerical calculations due to contact node shifting. To encounter this problem, sticking and non-separable contact is established between all bodies in the operation „Preheat“ and „Welding“, as visualised in Figure 3.16. For the third operation „Declamping“, the clamping system including the table is removed, thus reducing the number of contact areas. Only one contact condition remains: the connection between the substrate and wall, which needs to be sticking because it is welded together. This approach enables a stable calculation and simple handling for manufacturing, sacrificing a minimum of accuracy by ignoring the deformation while the clamping system is active. As

benefit, this approach suggests high accuracy for the residual stress relief analysis because of full elasto-plastic modelling of the bodies.

	Master	Slave	Sep	Friction	Interface Heat
✓ <input checked="" type="checkbox"/>	(1) Table	(2) Substrate	NO	Shear 1	f(Time)
✓ <input checked="" type="checkbox"/>	(1) Table	(3) Clamp_long	NO	Shear 1	f(Time)
✓ <input checked="" type="checkbox"/>	(1) Table	(4) Clamp_short	NO	Shear 1	f(Time)
✓ <input checked="" type="checkbox"/>	(3) Clamp_long	(2) Substrate	NO	Shear 1	f(Time)
✓ <input checked="" type="checkbox"/>	(4) Clamp_short	(2) Substrate	NO	Shear 1	f(Time)
✓ <input checked="" type="checkbox"/>	(2) Substrate	(5) Wall	NO	Shear 1	1

**Figure 3.16:** Table of contact properties between all used objects

In DEFORM<sup>®</sup> the thermal conduction coefficient  $k$  and can be entered as a function of time, which is used according to the increase in contact pressure due to the bending stresses when welding. For unloaded connections,  $k = 1 \frac{\text{N}}{\text{mm}\cdot\text{s}\cdot\text{K}}$  is used. Depending on contact pressure, up to  $k = 12 \frac{\text{N}}{\text{mm}\cdot\text{s}\cdot\text{K}}$  can be used in high pressure clamping or forming operations. Therefore, the empirically determined rise in thermal conduction due to contact pressure shown in Figure 3.17 can be classified as a realistic assumption.

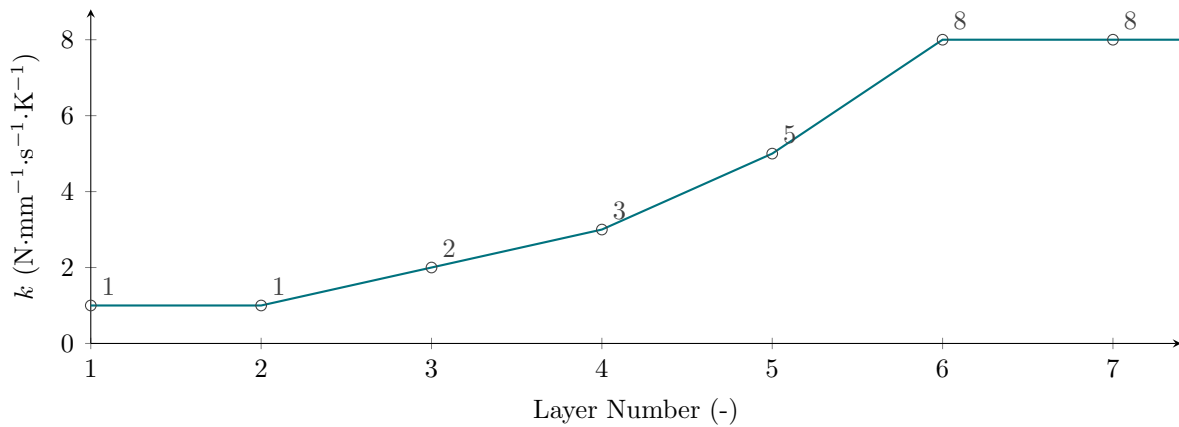


**Figure 3.17:** Increase of the contact heat transfer coefficient  $k$  due to distortion

### 3.3.4.4 Clamping Force

Due to the use of standardised welding clamps, it becomes very time consuming to measure the applied clamping force for each setup. Therefore, a more practical way is chosen: tightening the clamping bolts with a defined torque by using a torque wrench. As the resulting clamping force on the work piece depends on the thread size and geometric

arrangements, a universal analytical approach is pursued to determine said force for every clamp schematically.

First, the thread size and pitch need to be determined to gather enough information to solve for the correlation shown in Figure 3.18. Depending on the thread pitch, a different angle determines the influence of forces. To solve the following equations, values for common thread sizes might be selected from Table 3.7 or equivalent specialised lecture.

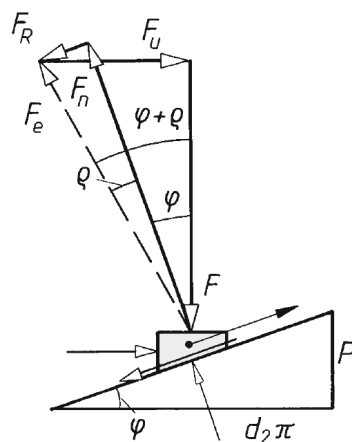


**Figure 3.18:** Schematic diagram of the forces acting on threads when under load [64]

The friction angle plays a major role when tightening. According to common literature,  $\varrho$  can be calculated by an amplification of the predominant coefficient of sliding friction  $\mu_G$ . Depending on the material combination and lubrication status,  $\mu_G$  can range from  $0.08 < \mu_G < 0.25$ . For a dry steel-steel combination, which is usually the case in a clamping situation,  $\mu_G = 0.12$  represents a realistic assumption. [64]

$$\varrho = \arctan(1.155 \cdot \mu_G) \tag{3.7}$$

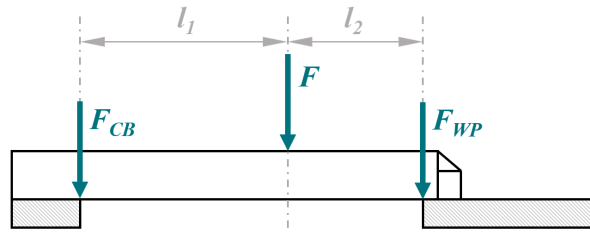
Now that all unknown variables are determined, the resulting clamping force  $F$  can be calculated by dividing the nominal torque moment  $M_T$  by the flank radius. Furthermore, the thread pitch and friction are taken into account when tightening the nut by adding the friction angle  $\varrho$ . [64]

$$F = \frac{2 \cdot M_T}{d_2 \cdot \tan(\varphi + \varrho)} \tag{3.8}$$

**Table 3.7:** Flank diameter and pitch angle of common metric thread sizes [64]

Thread Size	$d_2$ mm	$\varphi$ deg (°)
M6	5.350	3.41
M8	7.188	3.17
M10	9.026	3.03
M12	10.863	2.94
M16	14.701	2.48

Depending on the decision to fully model clamps or simplify them, calculations may be ended at this point. If the clamping system including the clamping block and nut is modelled, the previously calculated clamping force  $F$  may be applied to the nut as boundary condition. When a simplified model is utilised, a force distribution according to geometrical arrangements of the clamping block and workpiece need to be considered, as visualised in Figure 3.19.


**Figure 3.19:** Schematic diagram of force distribution in clamping systems

To calculate the resulting force on the clamping area, exact measurements of  $l_1$  and  $l_2$  need to be known. Further simplification includes a measurement from the incipient edge of the respective object and the clamping screws center line.

$$F_{WP} = \frac{F \cdot l_1}{l_1 + l_2} = \frac{2 \cdot M_T \cdot l_1}{d_2 \cdot \tan(\varphi + \rho) \cdot (l_1 + l_2)} \quad (3.9)$$

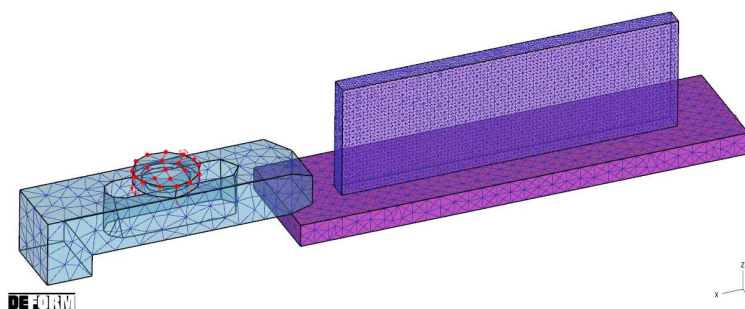
The so calculated clamping force can now be used to apply contact pressure as boundary condition through the known clamping contact area on the workpiece.

In this setup, a full clamp model was chosen. Therefore, the force is calculated as shown in Table 3.8 and applied directly onto the clamp using  $F$  as visualised in Figure 3.20. Alternatively, an equivalent pressure according to the surface area, in this case  $p = 185$  MPa, can be applied on the indicated area.



**Table 3.8:** Values needed to calculate clamp forces

Object	$M_T$ Nm	$d_2$ mm	$\varphi$ deg (°)	$\varrho$ deg (°)	$l_1$ mm	$l_2$ mm	$F$ kN	$F_{WP}$ kN
Clamp long	80	7.188	3.17	7.891	80	50	114	70
Clamp short	80	7.188	3.17	7.891	50	50	114	57

**Figure 3.20:** Visualisation of clamp force applied as boundary condition

### 3.3.5 Heat Source and Activation Volume Setup

When selecting „Additive Manufacturing“ in DEFORM<sup>®</sup>, it is possible to choose different pre-defined heat source models and processes like „Arc Welding“ in this case. Every welding heat source can then be configured using timetables containing the respective information about magnitude, travel path and orientation. What can not be changed depending on process time are the volumetric heat source parameters, as well as the initial element temperature when activated by the heat source. This opens the need for separate pre-processing modules if geometrical properties need to be changed.

Regarding activation, a group of dummy heat sources is created, as proposed in chapter 3.2.6 to establish conditions described in chapter 2.3.7. In this experiment, 4 additional dummies are needed to cover the targeted weld bead width. Their activation radius is set to  $r_d = 1.56$  mm, which represents the layer shift and therefore the maximum possible value. To prevent problems regarding incorrect energy distribution, the dummy heat source power is set to  $P_d = 0.01$  W and their volumetric size is effectively set to zero by choosing  $C_i = 0$  m.

Furthermore, the number of welded layers needs to be configured, in this case 32. All described changes to the default settings inside the DEFORM<sup>®</sup> environment can be

comprehended in Figure 3.21. The corresponding tables can be loaded using the import buttons in the bottom of the „Heat Source“ category.

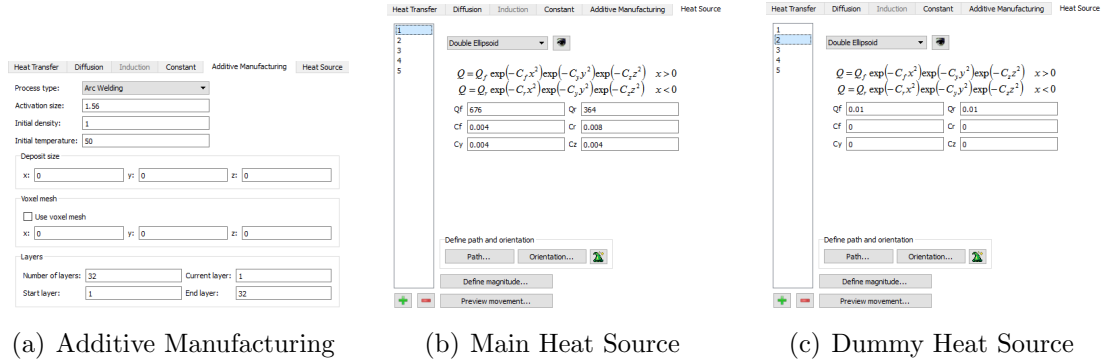


**Figure 3.21:** Heat source settings inside the DEFORM<sup>®</sup> arc welding environment

### 3.3.6 Step Size and Simulation Control

In simulation control, one must define an absolute time step size or a temperature dependent step size. Further, a step limit needs to be defined so the calculation is stopped at the right time. Since the real experimental data is logged every second, the time interval to be saved is also set to one second. Time step size is calculated according to the method proposed in chapter 3.2.8, which results in a timetable to be imported. Therefore, step size is defined as a function of process time and the stopping steps are defined as  $s_p = 74$  for preheating and  $s_w = 1307$  for welding.

Alternatively, if no dynamic step control can be used, then the time step size is set to a static value of one second. Stopping steps need to be adjusted to process times, which read  $s_p = 170$  for preheating and  $s_w = 3500$  for welding. As can be clearly seen, this approach might be more simple, but requires roughly 60% more steps to calculate, which can make a difference of several hours.

### 3.3.7 Point Tracking for Temperature Response

As final step, process specific tracking points are defined to replicate the thermocouples placed in the real manufacturing experiment according to the coordinates listed in Table 3.9. This results in a list of four tracking points P1 to P4, which replicate their real life counterparts. As example, the tracking point placement can be observed mid-process in Figure 3.22.

**Table 3.9:** Coordinates entered in DEFORM® to track thermocouples

Name	x	y	z	Object
-	mm	mm	mm	-
TC1	-65	-10	40	Substrate (2)
TC2	0	-10	40	Substrate (2)
TC3	65	-10	40	Substrate (2)
TC4	0	-15.9	35	Substrate (2)

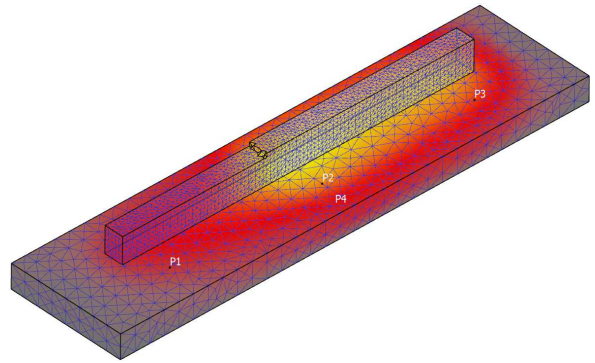


**Figure 3.22:** Visualisation of the thermocouple positions while welding in DEFORM®

## 4 Parameter Optimisation

The basis of every representative FEA is an accurate model of the process. Therefore, all necessary steps described in chapter 3 are taken for granted in the following analysis. Heat transfer settings, boundary conditions and component arrangements are not changed at this point to create a proper environment for statistical analysis and the possibility of interpolation between the measured data points.

### 4.1 Analysis of Influencing Variables

Heat input depends on several variables connected to the heat source and element activation strategy. In the following, an overview of interesting parameters to optimise shall be given, as well as implementation possibilities in FEA.

#### 4.1.1 Thermal Efficiency

On one side, the coefficient of thermal efficiency  $\eta$  depends on the used welding voltage and current. On the other side it depends on the arc length and physical weld pool behaviour. As side effect, overall quality is influenced by welding machine specific power settings, as described in chapter 2.1.2.1. In FEA, thermal efficiency is usually assumed to be constant over the process. In real welding applications, arc wandering and weld pool differences when welding on top of a previous layer will definitively influence efficiency. Heat input is also greatly influenced by the torch to workpiece distance, because longer arcs are more prone to electromagnetic blowing effects and other influences, reducing energy efficiency. However, it is very hard to measure and prove without time and resource intensive verification experiments. Therefore, this parameter becomes a prime example for parameter variation experiments like DoE or ML, to find real or optimal process parameters through data analysis rather than physical experiments.

#### 4.1.2 Goldak Double Ellipsoid Parameters

As described in chapter 2.3.6, the geometric shape and possible combination of multiple shapes greatly influences overall accuracy. However, the mathematical heat source model should be kept the same for all experiments because no target-oriented cognition can be

realised the other way. It is possible to use a GDE heat source in DEFORM<sup>®</sup> natively, which offers great overall precision, but has some flaws previously described in chapter 2.3.6.2. Also the activation size can be set to a certain length, which is then translated to a square cross section above the GDE, producing a solid base model for a simple arc welding process. Therefore, this model is used for convenience reasons in the following experiments, leaving 6 possible parameters to manipulate as shown in Table 4.1.

**Table 4.1:** Heat source parameters available in DEFORM<sup>®</sup> 12.1

Description	Variable	Unit
Power distribution to the front	$Q_f$	W
Power distribution to the rear	$Q_r$	W
Front ellipsoid apex	$C_f$	m
Rear ellipsoid apex	$C_r$	m
Common ellipsoid width	$C_y$	m
Common ellipsoid depth	$C_z$	m

When the heat source is calibrated correctly, its width should be identical to those of the weld bead, therefore eliminating one variable for variation experiments. Power distribution can also be summed up into the distribution factor  $f_f$ , which is originally used in the calculation for  $Q_f$  and  $Q_r$  and therefore directly proportional to welding power.

$$f_f + f_r = 1 \quad (4.1)$$

This connection further results in the front to rear distribution.

$$Q_f = Q \cdot f_f \quad (4.2)$$

$$Q_r = Q \cdot (1 - f_f) \quad (4.3)$$

### 4.1.3 Element and Time Step Size

A simplified single wall model is built and run with different mesh grid sizes to find a balanced setting between the calculation time and sufficient accuracy in thermal analysis. In this model, a single weld bead is placed without a preheating pass to observe the resulting temperature history depending on the mesh size, which is increased subsequently for each part, until a difference can be observed. Additionally, the so found minimum mesh size is connected to the minimal possible time step size. It makes no sense to move the heat source for a distance per time step smaller than the element size. On the contrary, it

is necessary to have as many elements as possible per time step, according to computational efficiency and the previously found reasonable limit due to accuracy and convergence.

Even if the heat source is calibrated and a proper activation strategy is chosen, deviations may occur due to FE specific problems. Because wire is fed from outside the welding environment, its temperature before entering the HAZ needs to be known in static elements. When the weld bead is meshed in advance and placed as static background mesh, an exact volumetric activation of this background mesh is crucial for overall accuracy, as visualised in Figure 4.1. If executed incorrectly or too rough mesh sizes are used, elements outside the current calculation step are activated as well, which then draw energy away from the actual heated volume and thus falsifies the result to lower temperatures. It also preheats a part of the next step's mesh, acting in a chain of falsification onwards.

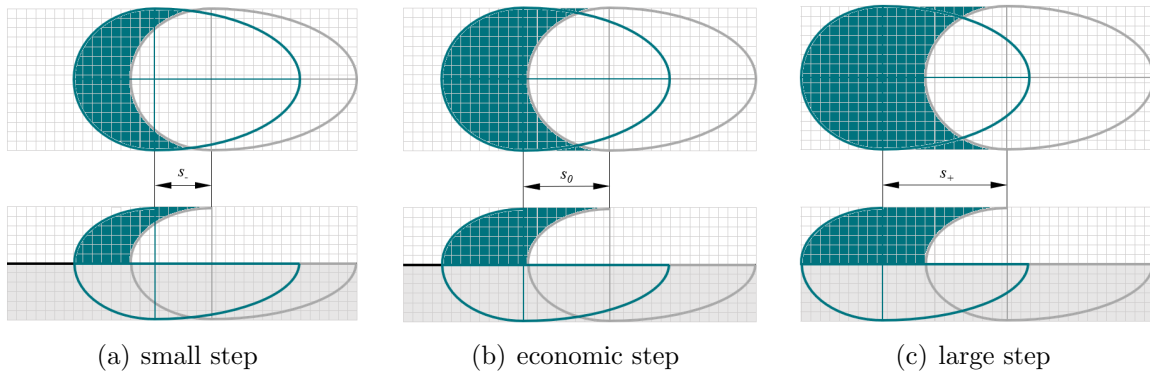


**Figure 4.1:** Impact of mesh size and time step size on activation accuracy

Due to simplifications regarding the activation size, resulting from a rectangular weld bead model, there will always be too much volume per step to match the correctly deposited amount, at least at the start and end points of a weld bead. Fine tuning at this dimension was found to have little impact in accuracy, as discussed in chapter 2.3.5, the error might be ignored. In case accuracy improvements are desired, adjustments in the layer's mass density can be made because the correct value of deposited wire mass per time step can be calculated in advance. Based on this information, the activated mesh volume per step can be assigned with a smaller mass density to match the correct mass per step deposition.

Additionally, a change in step width  $s$  has a non-linear connection to the activated volume. Therefore, it is proposed to match the time step size as close as possible to the ideally calculated step width  $s_0$ , which results in a theoretically deposited mass per step. Although a smaller step size potentially provides higher accuracy, assuming a constant

wire feed, the boundary set by  $s_0$  is approached in favour of computing time by conducting the experiment proposed in Figure 4.1 for different time steps.

#### 4.1.4 Properties of Molten Elements

Due to convenience in FEA, molten elements can not be modelled easily because of a change in the physical properties. Therefore, an initial temperature  $T_i = 50$  K is often chosen for activated elements. This approach however bears the risk of artificial energy loss, because an incorrect amount of heating power is used to melt the deposited material. The resulting difference in energy input may be heating surroundings too much and thus rise the general temperature level.

The other extreme is represented by statically activating each respective part of a layer at room temperature. While this approach offers a more realistic representation in general, the element- and activation size matter a lot. If too much volume is activated, heat flow is obviously falsified because the correct amount of energy is distributed to a larger volume of material.

## 4.2 Design of Experiments

In the following paragraphs, general approaches and the detailed structure of internal design choices shall be documented and described for better traceability.

### 4.2.1 Determination of the Objective

The primary goal is the as close as possible approximation of the real temperature history within FEA. For this purpose, an initial model is needed and built, as described in chapter 3.3, to accurately compare the changes made in individual runs throughout the later parameter variation. In the end of this experimental study, overall deviation from real measurements, represented by TC2 and TC4 shall be minimised.

### 4.2.2 Reference Data

Since TC2 is placed on top of the substrate's surface, it is directly exposed to hot process gases and spatter, which concludes that temperature peaks are falsified. Therefore, TC4 is primarily used for the numerical accuracy comparison, however TC2 is also used to verify

statements. This is possible because the thermocouple readings should always be correct in cool down phases, when the torche's plasma source is switched to standby.

To generate a comparative basis, every time sample of the process is numerically analysed by loading the respective thermocouple's timetable. Each conducted run generates a temperature response curve  $P_i$ , which can be sampled to the same time interval as the real life counterpart thermocouple  $TC_i$ . By subtracting the FEA values from thermocouple values, an absolute temperature deviation  $\Delta T$  can be determined, which builds the foundation of comparison. An example can be observed in Figure 4.2.

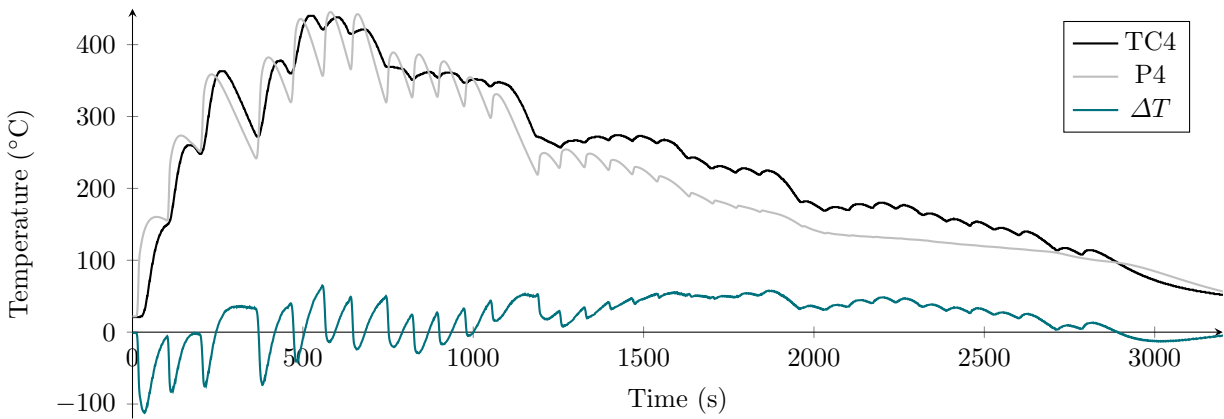


**Figure 4.2:** Visualisation of the time sampled temperature difference approach

### 4.2.3 Design Method

As described in greater detail in chapter 2.4 and also summarised by Prasad et al. in [55], not every method is suitable for every research target. In this study, focus lies on as precise as possible determination of the chosen heat source parameters, rating Taguchi's and factorial methods as unsuitable, because they are not able to exactly find best parameter values and further hardware oriented testing is necessary. This leads to a derivation of RSM, which is able to find the best combination of parameters.

The experimental run effort of RSM designs may reach double of the Taguchi method, but accuracy and possibilities for later optimisation is opened. Therefore, a CCC design, as shown in 2.16(a), is chosen for the experimental design. For this purpose, MATLAB® provides a statistics and machine learning toolbox [60], which already includes a function to generate composite design arrays.



```
doeRaw = ccdesign(nrPar, 'type', 'circumscribed', 'center', 1, 'fraction', 0);  
doeRaw = (doeRaw+1) / (nrPar-1);  
doeRaw = round(doeRaw, 2);
```

It is chosen to only use a single center point, although it is generally recommended to use at least 4. This is needed in real world experiments to compensate for random process noise, which is not to be expected in FEA. Furthermore, a fraction level of 0 is chosen, which means, that the generated array contains all calculated values. In case of very large arrays, the fraction level can be increased to sacrifice statistical accuracy for less runs. Since a maximum of about 30 runs per DoE setup is obtained within the framework of this study, no further reduction is needed.

By normalising the output values, a percent value array is created, which can then be applied to the previously defined minimum and maximum parameter values.

```
doeNum = zeros(height(doeRaw), width(doeRaw));  
for i = 1 : nrPar  
    doeNum(:, i) = par.Min(i) + doeRaw(:, i) .* (par.Max(i) - par.Min(i));  
end
```

For later comprehensibility, a naming system is introduced to individually generate run names based on the DoE setup revision, experiment name and material used. This array is then converted to a table for convenient exporting and further formatted to fit the DEFORM<sup>®</sup> specific parameters, as attached in Appendix B.

```
varNames = par.Name;  
rowNames = string(linspace(0, nrRuns-1, nrRuns)) + "_V1_S1128_Ti64";  
DoE = table(doeNum, 'VariableNames', varNames, 'RowNames', rowNames);  
  
for i = 1 : nrRuns  
    % extract current distribution factor ff and calculate absolute values  
    ffTemp = table2array(DoE(i, "ff"));  
    DoEdeform{i, "Qf"} = round(weldPower * ffTemp);  
    DoEdeform{i, "Qr"} = round(weldPower * (1 - ffTemp));  
    % fill remaining columns in correct order  
    DoEdeform(i, "Cf") = DoE(i, "Cf");  
    DoEdeform(i, "Cr") = DoE(i, "Cr");  
    DoEdeform{i, "Cy"} = 0.004;  
    DoEdeform(i, "Cz") = DoE(i, "Cz");  
end
```

#### 4.2.4 Response Surface Model

In the following, the developed MATLAB<sup>®</sup> function „customRSM“ shall be described in greater detail for better insight of response surface modelling and a special application discovered in the process of creation. Usually, one response parameter is optimised to a static value. However, in this application, a time series of connected events (second wise generated temperature data) is observed, which will most likely not produce a discrete optimum value. Therefore, further analysis needs to be conducted to apply the DoE optimisation process to a time series and gather useful results.

Depending on the used response surface model, a certain polynomial degree is necessary to build the mathematical equations in the background. Basically, the higher the interaction between chosen parameters and therefore the higher the accuracy gets, the more coefficients are needed. When building the response surface  $S$ , a linear model  $S_L$  is used as basis. Here, surface coefficients  $\beta_i$  are used in combination with all available input parameters  $x_i$ .

$$S_L = \beta_0 + \beta_1 x_1 + \beta_2 x_2 + \beta_3 x_3 \quad (4.4)$$

Linear models are often too inaccurate, so parameter interaction terms  $S_I$  and quadratic terms  $S_Q$  are added to receive a full quadratic surface model.

$$S_I = \beta_{12} x_1 x_2 + \beta_{13} x_1 x_3 + \beta_{23} x_2 x_3 \quad (4.5)$$

$$S_Q = \beta_{11} x_1^2 + \beta_{22} x_2^2 + \beta_{33} x_3^2 \quad (4.6)$$

This connection results in a cumulative sum of partial models to calculate a general solution for the response surface  $S$ . As the amount of parameters  $k$  rises, more individual surface coefficients  $\beta$  are needed to describe the wanted model. As coefficient arrays grow rapidly when adding polynomial degrees, cubic models are avoided in praxis.

$$S = S_L + S_I + S_Q = \beta_0 + \sum_{i=1}^k \beta_i x_i + \sum_{i=1}^{k-1} \sum_{j=2}^k \beta_{ij} x_i x_j + \sum_{i=1}^k \beta_{ii} x_i^2 \quad (4.7)$$

Numerically, the function „x2fx“ can be used in MATLAB<sup>®</sup> to build a linear ( $S_L$ ), interactive ( $S_L + S_I$ ), or full quadratic model ( $S_L + S_I + S_Q$ ) by providing the number of parameters used and a model identification term. Then the coefficient vector  $\beta$  can be calculated by simple QR-decomposition.

```
design = x2fx(x,model);  
[Q,R] = qr(design,0);  
beta = R \ (Q' * y);
```

Now that all surface parameters are known, the other significant model parameters can be considered. The confidence interval size  $\alpha$  is especially important to deal with extreme outliers while preserving statistical accuracy. Therefore,  $\alpha = 0.05$  is usually applied in statistical analysis, which is also adopted here.

```
res = y - (design * beta);           % residuals  
dof = max(size(y,1)) - length(beta); % degrees of freedom  
pconv = 1 - alpha;                  % percent of data represented
```

By using the resulting DoF as a control mechanism, the root means square error (RMSE) and  $R^2$  value can be calculated to receive basic accuracy indicators for the just fitted surface parameters.

```
if (dof > 0)  
    rmse = sqrt(sum(res .* res) ./ dof);  
    crit = sqrt(length(beta) * finv(pconv,length(beta),dof)) * rmse;  
else  
    rmse = NaN;  
    crit = NaN;  
end  
  
sstot = sum(y.^2);  
ssres = sum(res.^2);  
R2 = (1 - (ssres / sstot));
```

For a detailed observation and correct scaling, the range needs to be adjusted according to the input parameters boundaries, which are defined by the user in the previously conducted DoE setup. This step can be critical for later analysis. Uneducated guesses might cause clipping, which occurs when the boundary bands are defined to narrow and optimal values are found outside set borders.

```
maxx = max(x);  
minx = min(x);  
xrange = maxx - minx;  
  
xfit = xrange(ones(nrPts,1),:) ./ (nrPts - 1);  
xfit(1,:) = minx;  
xfit = cumsum(xfit);
```

The analysis is performed separately for each parameter of interest, which enables a universal approach inside a loop to minimise the individual coding effort. First, the x

range is fitted to defined parameter boundaries, then the individual values are applied to the previously found universal response surface to obtain a specific polynomial function to describe the current parameter. Afterwards, the set up response surface is evaluated for the current parameter, resulting in a numerically predicted polynomial.

```

for k = 1:nrPar
    initx = xsettings;
    tempx = xfit(:,k);
    initx(1:nrPts,k) = tempx;

    xpred = x2fx(initx,model);
    yfit(:,k) = xpred(1:nrPts,:) * beta;    % y = b0 + b1x + b2x + ...

```

It is mandatory to calculate the confidence intervals for this polynomial to describe inaccuracy. Only predicted response polynomials with low spread can be seen as useful outcome.

```

err = xpred(1:nrPts,:) / R;
tmp = sqrt(sum(err .* err,2));
dy = repmat(tmp,1,length(crit)) .* repmat(crit, length(tmp),1);

convUp = yfit - dy;
convDown = yfit + dy;

```

Depending on the surface model used, linear or polynomial parameter responses are obtained. This results in the possibility of multiple response values intersecting the x-axis, which represents  $\Delta T = 0$  K. It is also possible that no intersection occurs inside the set process parameter boundaries. For these two cases, visualised in Figure 4.3, a determination method needs to be implemented for clipping prevention.

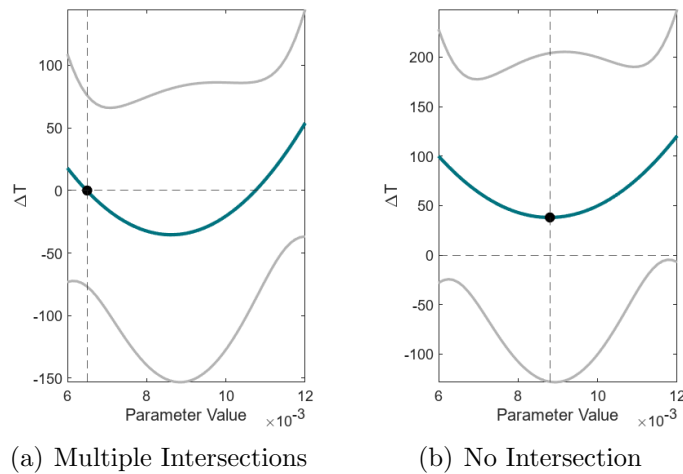


**Figure 4.3:** Handling of special cases in RSM analysis of individual timestamps

To handle this problem, a polynomial is fitted to the numerically found response data points to generate a continuous function for further analysis. Due to the circumstance that  $\Delta T$  can be negative, absolute values are formed to simplify the calculation steps.

```
cfs = polyfit(xfit(:,k),yfit(:,k),polyDeg);
xtemp = linspace(minx(k),maxx(k),nrSamles)';
ytemp = polyval(cfs,xtemp);
ysqr = sqrt(ytemp.^2);
```

Potential zeros are found by sorting all y values ascended and cutting off the number of potential intersections according to the used polynomial degree. Parameter values represented by x are then found through reverse searching.

```
ymin = sort(ysqr,"ascend");
ymin = ymin(1:polyDeg)';

[minID,~] = find(ysqr==ymin);
pot0 = xtemp(minID);
```

Finally, the previously found zeros are observed. If multiple zeros are possible, the optimal parameter selection is based on the value with the smallest confidence interval, which suggests the best possible accuracy.

```
% choose potential zero with smallest variance inside x range
varzero = interp1(xfit(:,k),dy,pot0);
[~,minID] = min(varzero);
optx(k) = round(pot0(minID),4);
[minID,~] = find(xtemp==pot0(minID));
opty(k) = ytemp(minID);
end
```

### 4.2.5 Interpretation Method

Response surfaces describe a parameter map depending on a chosen evaluation variable, which makes it possible to find the best combination of the individual parameters by applying mathematical boundary conditions. In this case, the evaluation variable shall be minimised, which translates to a local minimum of the generated surface. However, this process is static and only applicable for one specific set of parameters in a certain process state.

Process parameters may change over the course of a manufacturing job, which makes the experiment's time series more interesting than any specific end result. Therefore, the built custom RSM analysis, described in the previous chapter, is applied for every calculation

step of the FEA. This approach creates a time series of theoretical best choices for every input parameter, as well as RMSE and  $R^2$  values for each input sample.

To conduct this advanced analysis, boundary conditions need to be established. A confidence interval of 90% is chosen for raw data to be considered. Furthermore, all individual RSM fits producing  $R^2 < 0.90$  are sorted out to prevent outliers and names are read out of the imported DoE table used to create the physical experiments.

```
p = 0.05;
minR2 = 0.90;

x = DoE{1:nrFiles, :};
xNames = string(DoE.Properties.VariableNames);
yName = "Temperature Difference";
```

Custom response surface fitting is conducted for the given parameters  $x$  and output measurement  $y$  in a loop to calculate the information for each timestamp of the given temperature curve. As most stable and representative thermocouple, TC4 is chosen for primary optimisation.

```
for t = 1 : dataCut
    y = tempDev.TC4{t, 1:nrFiles}';
    tempRSM = customRSM(x, y, "linear", p, xNames, yName, "false");

    if tempRSM.R2 < minR2           % filter for outliers
        bestParRaw{t, :} = NaN;
    else
        bestParRaw{t, 1:3} = tempRSM.optPar;
        bestParRaw.RMSE(t) = tempRSM.RMSE;
        bestParRaw.R2(t) = tempRSM.R2;
    end

    if isnan(bestParRaw.R2(t)) == false
        b = b + 1;
        tempBest = [t, bestParRaw{t, :}];
        bestPar{b, :} = tempBest;
    end
end
```

Next, the mean and median values are calculated for the found optimal parameter choice array to find a best possible general fit of input parameters for the whole process duration.

```
meanPar = round(mean(bestPar{:, 2:6}), 4)
medPar = round(median(bestPar{:, 2:6}), 4)
```

To visualise an example outcome in Figure 4.4, the grey circles represent the individual optimal parameter choices for each timestamp. It would also be possible to use the whole characteristic polynomial of each timestamp to produce a surface map. However, a two dimensional approach using only the optimal parameter data points offers a clearer layout, as well as more efficient computing, especially when considering that only optimal parameter values are the subject of this investigation.

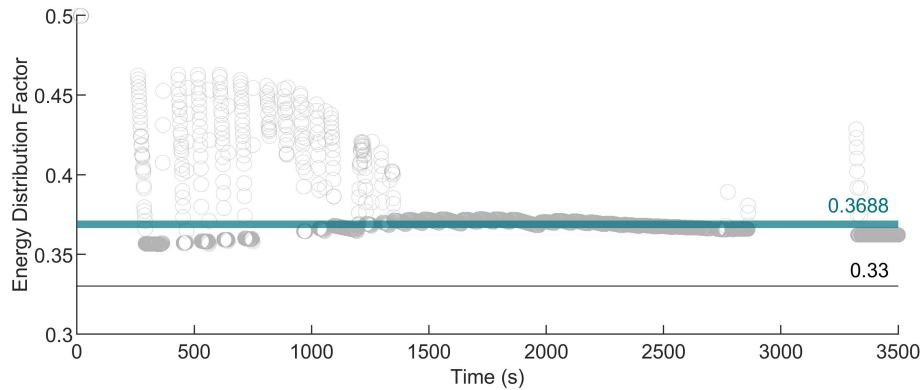


**Figure 4.4:** RSM analysis applied on a time series

This approach can be refined individually by fitting polynomials or layer-wise analysis to obtain some sort of time dependent parameter data. However, it becomes very hard to verify possibly extracted curves. Therefore, sufficient and careful considerations regarding meaningfulness need to be made to prevent unrealistic assumptions.

## 4.3 Simulation Runs and Parameter Variation

For the following experimental runs, only thermal FEA is used to approach the benchmark measurements provided through TC4. This proceeding is suitable because calculation effort is limited. Orientation of parameter influence needs to be conducted first, afterwards a separate analysis can be set up to investigate the remaining important parameters.

### 4.3.1 Run 1 - Inspection of Geometric Influence

In the first experiment, only heat source parameters are chosen for variation to figure out their overall influence. Especially the geometrical parameters are a point of interest, because they are generally hard to physically investigate.

In this context, the heat source width is kept constant at  $C_y = 0.04$  because the weld bead width is not expected to change. Further, the power parameters  $Q_f$  and  $Q_r$  are combined into the distribution factor  $f_f$  to reduce the number of parameters, as displayed in Table 4.2.

**Table 4.2:** Process parameters and their range for DoE run 1

Description	Variable	Min	Max	Unit
Power distribution factor	$f_f$	0.20	0.50	-
Front ellipsoid apex	$C_f$	0.002	0.006	m
Rear ellipsoid apex	$C_r$	0.002	0.006	m
Common ellipsoid depth	$C_z$	0.006	0.012	m

A CCC design is created according to the previously mentioned MATLAB<sup>®</sup> procedure, resulting in 26 simulation runs. Assuming the empirically found heat transfer function between the substrate and welding table is correct, good estimations can be made by using a quadratic RSM model to gather optimal process parameters through the median output, visualised in Figure 4.5. It can also be observed that the newly found optimal process parameters do not differ too much from the assumed normalised starting values.

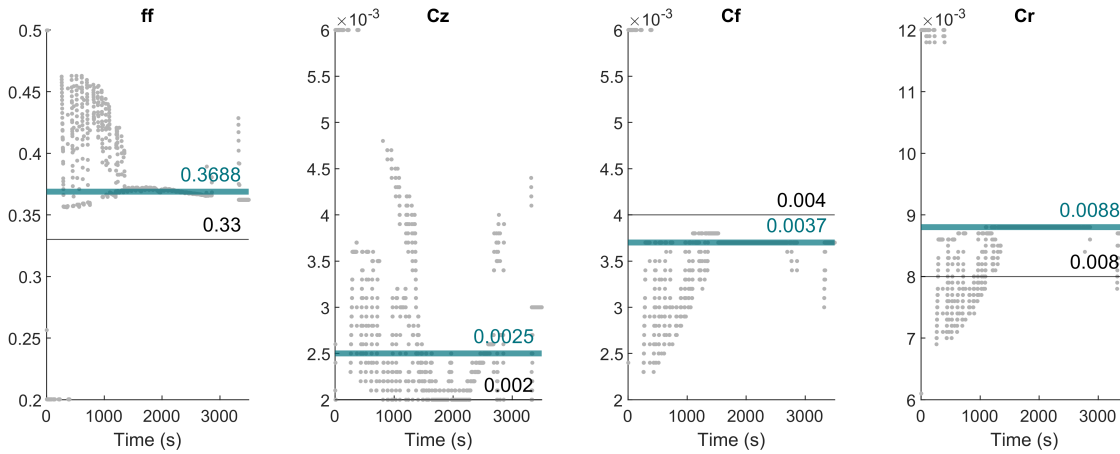


**Figure 4.5:** Optimal parameters of the custom time series RSM analysis for run 1

Small manual adjustments to the suggested optimal parameters in this run already show a pretty good agreement with the thermocouple measurement, which can be observed in Figure 4.6. Especially in the first layers, the real process temperature (black line) is covered well by a compilation of experimental curves (green lines). In the middle however,



significant underperformance can be observed, which might be connected to a change in thermal efficiency or contact heat due to deformation resulting from residual stress relief. Therefore, further investigations will focus on the energetic parameters rather than the geometric ones.

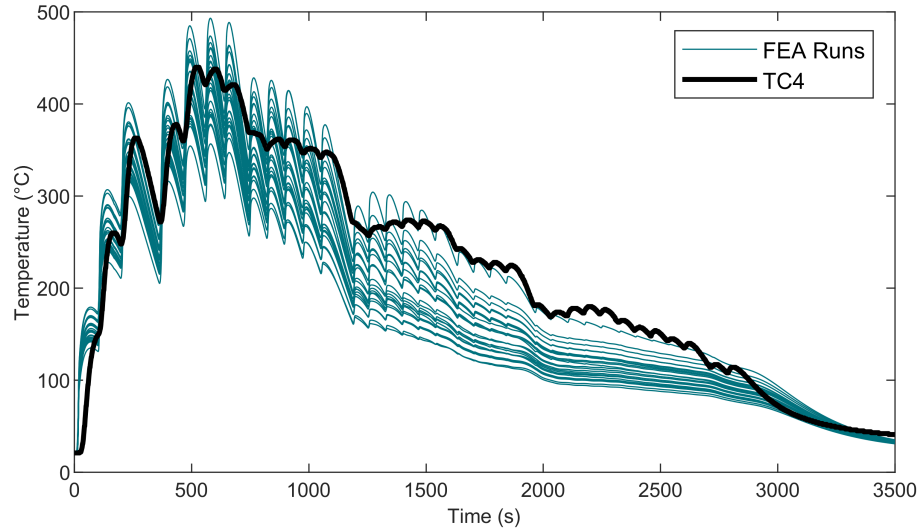


**Figure 4.6:** Visualisation of temperature responses in run 1

### 4.3.2 Run 2 - Inspection of Thermal Influence

In this run, only thermal parameters are observed to figure out the feasibility of a more universal approach with fixed geometrical parameters. For this purpose, the theoretical optimal values found in run 1 are used for the entire experiment. The initially empirical contact heat transfer coefficient is set to a constant value of  $k = 1 \frac{\text{N}}{\text{mm}\cdot\text{s}\cdot\text{K}}$  for the whole process to cancel out its influence. As compensation for the suspected temperature deviation, thermal efficiency is taken into account in DoE. It is suspected that thermal efficiency is not constant in the real process, therefore the focus lies on finding a time dependent influence, if possible. Additionally, the initial element activation temperature is observed, resulting in the variation plan shown in Table 4.3.

**Table 4.3:** Process parameters and their range for DoE run 2

Description	Variable	Min	Max	Unit
Power distribution factor	$f_f$	0.25	0.40	-
Thermal efficiency factor	$\eta$	0.20	0.50	-
Initial element temperature	$T_i$	20	150	°C

As before, a CCC design matrix is built according to the experimental plan and quadratic RSM is applied for the whole time series. The resulting 15 simulation runs produced an optimal parameter selection according to Figure 4.7, which can clearly be ruled out as productive outcome because of clipping. This essentially means, that parameter boundaries are chosen poorly, resulting in the maximum possible parameter choices for almost all time stamps. Ideally, the suspected parameter range is only filled by about 80 %.

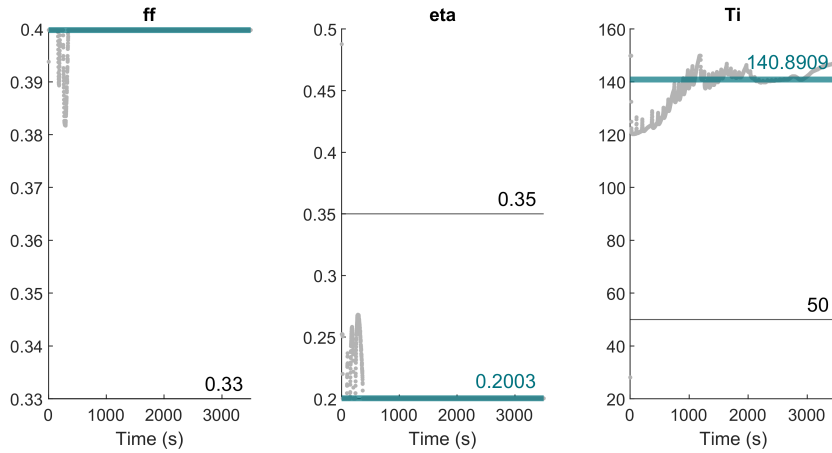


**Figure 4.7:** Optimal parameters of the custom time series RSM analysis for run 2

The experimental response curves shown in Figure 4.8 clarify the previously mentioned clipping issue. As can be observed, all responses exceed the real thermocouple measurement by far, especially from layer 3 onwards.

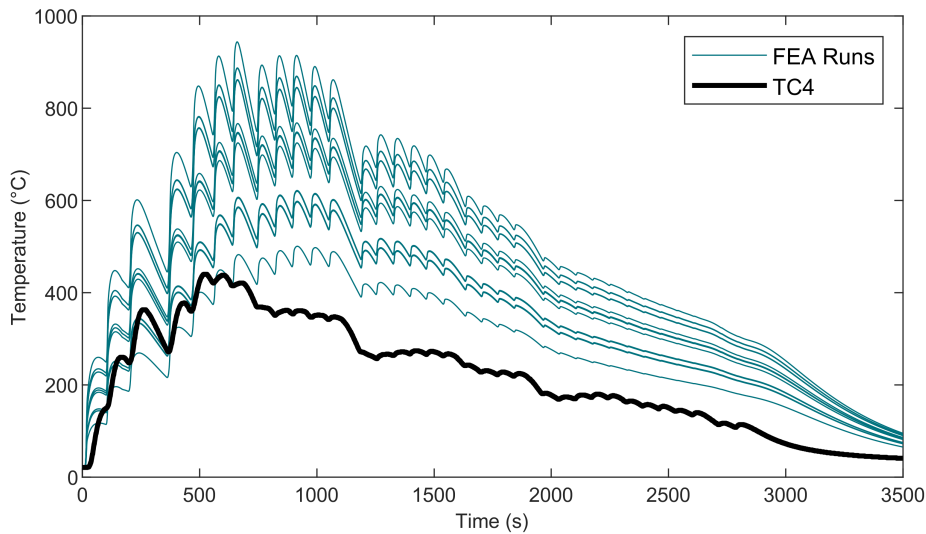


**Figure 4.8:** Visualisation of temperature responses in run 2

As a result of the mentioned clipping issues, this run only serves as indicator of a non-linear connection of the coefficient of thermal conduction  $k$  and eventually thermal efficiency  $\eta$ . However, due to the connection to the initial element activation temperature, thermal efficiency is also influenced, which further weakens these arguments.

### 4.3.3 Run 3 - Verification of Contact Setting Assumptions

Now the initial element temperature is replaced with the thermal conduction coefficient  $k$  for variation, as shown in Table 4.4. Also, power distribution is changed to front-heavy because it is suspected that power distribution mainly causes a time shift in the thermal response, but no drastic changes in absolute temperature cycles.

**Table 4.4:** Process parameters and their range for DoE run 3

Description	Variable	Min	Max	Unit
Power distribution factor	$f_f$	0.50	0.80	-
Thermal efficiency factor	$\eta$	0.25	0.40	-
Thermal conduction coefficient	$k$	5	10	$\frac{\text{N}}{\text{s}\cdot\text{mm}\cdot\text{K}}$

As can be seen in Figure 4.9, similar problems like in run 2 arise when observing energy distribution and thermal efficiency, because almost the same setup as in run 2 is used. This was constructed intentionally to investigate a swap in distribution to front-heavy, as well as thermal conduction over time.

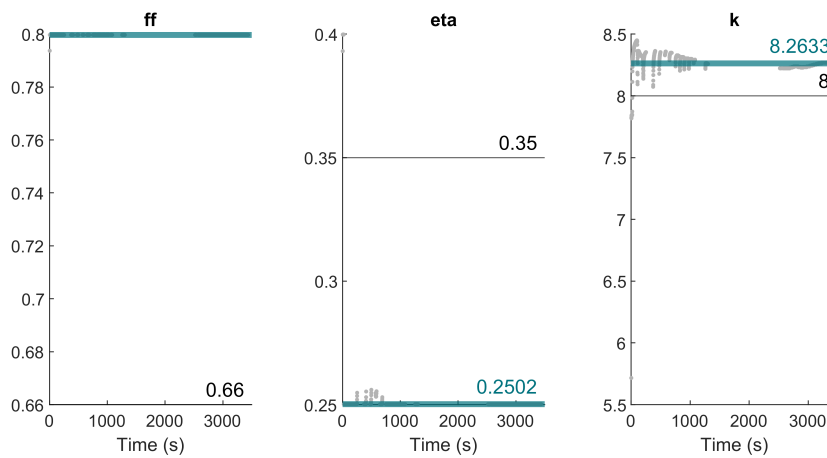


**Figure 4.9:** Optimal parameters of the custom time series RSM analysis for run 3

Run 3 showed that the assumption of  $k = 8 \frac{\text{N}}{\text{mm}\cdot\text{s}\cdot\text{K}}$  in the first place seems to be a pretty accurate estimation over the course of the process. Figure 4.10 proves, that thermal conduction is indeed time dependent and even with non-ideal energetic heat source parameters, largely influences the thermal history and therefore needs to be further investigated.

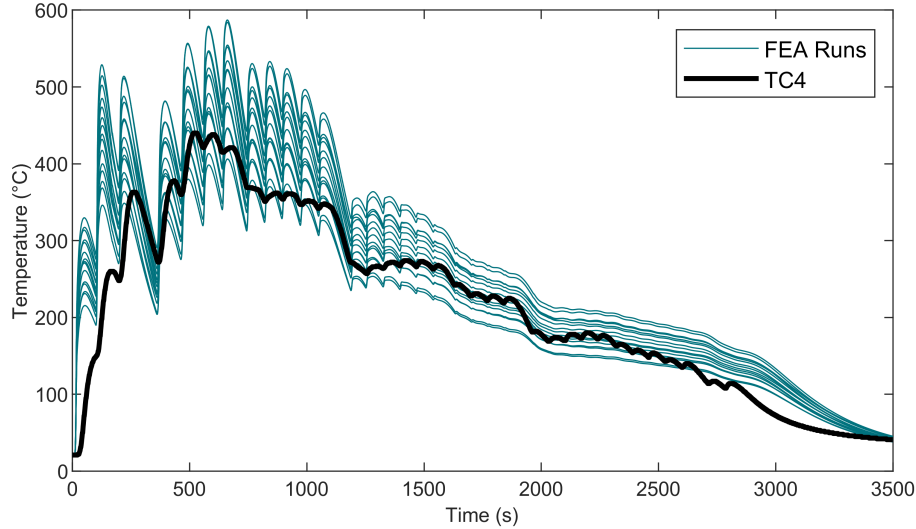


**Figure 4.10:** Visualisation of temperature responses in run 3

## 4.4 Improved Approach through Previous Findings

A new model is built from all findings so far to enhance the performance for detailed FEA. For this purpose, several changes in the initial setup need to be made, as well as parameter adjustments throughout the process. Since run 1 already showed promising results, it is normalised to serve as the basis for a manual parameter variation. This way the conjectures gathered from run 2 and 3 can be tested and fitted, until a solid and representative model is achieved.

### 4.4.1 Heat Source Setup in DEFORM<sup>®</sup>

All geometrical heat source parameters are normalised to the suggested starting values mentioned in common literature. As weld bead width  $b_{weld}$  is limited by the deposited wall width, also the heat source's width parameter  $C_y$  is limited. This further determines the normalised dimensions as follows:

$$C_y = \frac{1}{2} \cdot b_{weld} \quad (4.8)$$

$$C_z = C_y \quad (4.9)$$

$$C_f = C_y \quad (4.10)$$

$$C_r = 2 \cdot C_y \quad (4.11)$$

The weld bead's width is extracted from the idealised 3D model as  $b_{weld} = 8$  mm, which then results in the parameter list shown in Table 4.5 to describe a normalised heat source fitted for the investigated manufacturing experiment.

**Table 4.5:** Normalised heat source parameters for the GDE

Description	Variable	Value
-	-	m
Front ellipsoid apex	$C_f$	0.004
Rear ellipsoid apex	$C_r$	0.008
Common ellipsoid width	$C_y$	0.004
Common ellipsoid depth	$C_z$	0.004

#### 4.4.2 Mesh Generation for Layer-Wise Arc Welding

As described previously, only tetrahedral elements can be used in DEFORM<sup>®</sup> for automatic slicing. This approach has worked so far, but shows some major flaws considering boundary conditions and solver convergence, especially in mechanical analysis.

There exists another rather inconvenient solution that uses a cuboid mesh, which drastically simplifies the FE model. This was only known to be functioning inside the powder bed and blow powder modules, which require a much higher initial element temperature upon activation and do not use the volumetric heat source's element activation strategy. In exchange, a rectangular activation cross section is defined, which does not consider the heat source's power as in arc welding. This circumstance makes an adaptation pointless, because all previously found parameters do not fit the used method any more.

After several iterations to stabilise thermo-mechanical analysis, a solution was found to realistically describe arc welding processes without the downside of a sliced tetrahedral mesh. For this purpose, a mapped brick mesh is used for the wall, substrate and table, according to Table 4.6. Clamps are still meshed in tetrahedral elements due to their rather

complex shape. Overall, a reduction in element count of around 80 % could be achieved compared to the tetrahedral only meshes with similar element size used before, promising superior calculation time.

**Table 4.6:** Mesh information for all objects involved in final validation

Object Name	Type	Ratio	Size mm	Elements	Nodes
Wall	cube	2	1.5625	27520	32109
Substrate	cube	2	2	11250	14196
Clamp long	tet	3	4	3008	777
Clamp short	tet	3	4	2397	622
Table	cube	2	30	300	682

The substrate was meshed in 2 mm element size, resulting in 5 thickness elements and an overall cubic expansion. Considering the manufactured wall, 1.5625 mm was chosen for element height, which represents exactly one normalised layer height. In width, 8 elements are placed, making them not exactly cubic. An overview of the so generated mixed mesh can be found in Figure 4.11.

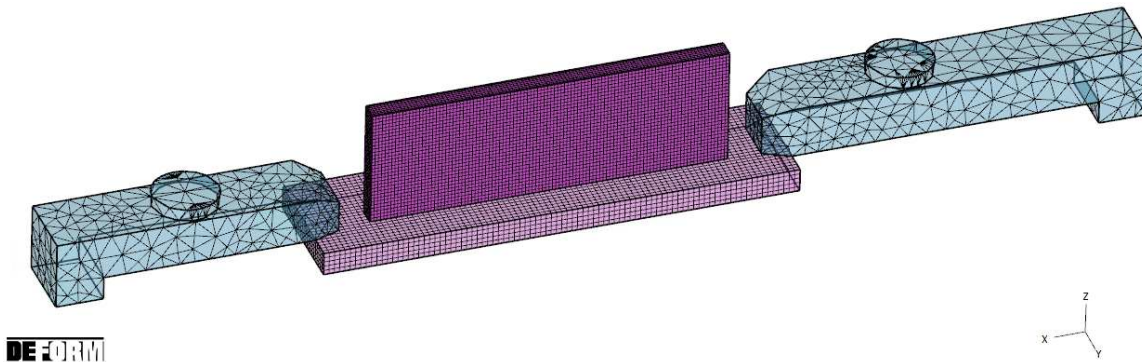


**Figure 4.11:** Visualisation of the introduced mixed mesh setup

Now that all bodies are meshed according to accuracy requirements, AM needs to be activated, which requires layer information. When using a brick mesh, the built in slicer is not available, requiring manual node picking to assign the needed layer information. This process is extremely labour intense if all 32 layers need to be selected. However in this workaround, all wall elements can be selected and assigned with layer 1 using the „object elements“ tool.

Since the whole model now consists of one layer, activation needs to be considered. Contrary to using the powder bed module, arc welding can still be chosen to correctly consider the previously found heat source model. Combining the generated deposition model depending on dummy heat sources and layer-less modelling. In contrast to other approaches that place the wall on top of the preheated substrate, it is mandatory to already initialise AM in the preheating step. Otherwise the wall can not be connected to the substrate in the subsequent welding step, resulting in solver errors and geometrical anomalies. Therefore, the already established approach using a heat source with activation size zero is used in preheating, enabling proper contact between the wall and substrate mesh.

#### 4.4.3 Time Dependent Thermal Conduction

As can be observed in Figure 4.12, heat conduction is split in two contact types to better mimic reality. Both curves show a significant increase after preheating due to the initial deformation and residual stresses induced. With increasing wall height, the substrate to table heat flow is reduced again because less surface area will be in contact with the table due to lifting of the substrate's edges. At around 2500 s, the welding operation is completed, which results in a drastic rise of contact pressure in both cases. This is suspected to happen because the part is cooling down to room temperature, which increases residual stresses and thus contact pressure on the remaining surface area.

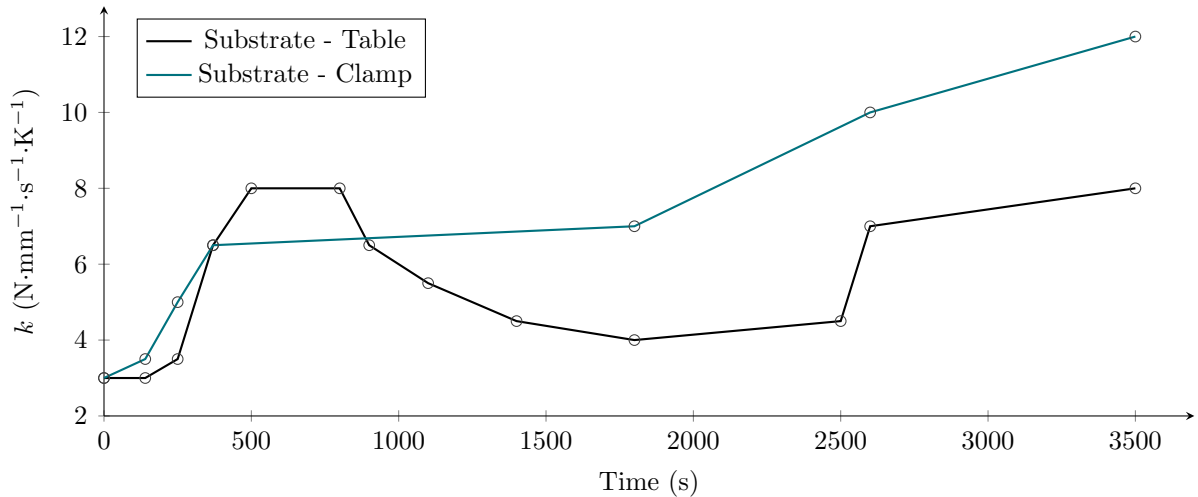


**Figure 4.12:** Experimentally found thermal conduction coefficients over time

#### 4.4.4 Contact Property Definition

Until now, no deformation took place in FEA, which means that all initialised contact nodes stick together throughout the whole process. However, in thermo-mechanical analysis,

nodes will shift and separate from each other, reducing the effective area of contact. If sticking boundary conditions are established to ensure contact, heat transfer is drastically falsified. Therefore, as realistic as possible contact settings need to be established, as shown in Figure 4.13.

	Master	Slave	Sep	Friction	Interface Heat
✓ <input type="checkbox"/>	(1) Table	(2) Substrate	YES	Coulomb 0.4	f(Time)
✓ <input type="checkbox"/>	(1) Table	(3) Clamp_long	YES	Coulomb 0.6	f(Time)
✓ <input type="checkbox"/>	(1) Table	(4) Clamp_short	YES	Coulomb 0.6	f(Time)
✓ <input type="checkbox"/>	(3) Clamp_long	(2) Substrate	YES	Coulomb 0.6	f(Time)
✓ <input type="checkbox"/>	(4) Clamp_short	(2) Substrate	YES	Coulomb 0.6	f(Time)
✓ <input checked="" type="checkbox"/>	(2) Substrate	(5) Wall	NO	Shear 1	1

**Figure 4.13:** Contact settings for the realistic modelling of deformation

To assist the solver regarding convergence, the substrate plate, as well as both clamps are fixed to the table using free distortion boundary conditions. This way, almost no nodes are excluded from surface contact, which would limit and falsify heat flow, but excessive movement is prohibited. It was also empirically tested, if node fixation is necessary in the first place. These investigations clearly showed an increase in convergence issues when no restrictions are applied. Contact pressure is accounted for by the previously described thermal conduction coefficient, which changes over time according to system changes.

Nodes will move due to thermal expansion and distortion, which needs to be realistically restricted by surface to surface friction. The previously shown contact settings use material pair dependent coulomb friction coefficients, as documented in Table 4.7. Contact friction between the wall and substrate is set to  $\mu_{TT} = 1.00$  because these components are welded together, prohibiting any relative motion further on.

**Table 4.7:** Coulomb friction used for all occurring material pairs

Description	Variable	Value
Titanium - Titanium	$\mu_{TT}$	1.00
Titanium - Steel	$\mu_{TS}$	0.60
Titanium - Aluminium	$\mu_{TA}$	0.40
Steel - Aluminium	$\mu_{SA}$	0.60



#### 4.4.5 Simulation Control

In this model, a thermo-mechanical analysis shall be possible, therefore a smaller time step size will be needed to converge. Explicit time steps are critical in a dynamic analysis, which is why a temperature gradient step size is applied in this model, as shown in Table 4.8.

**Table 4.8:** Dynamic time step size settings for final validation

Description	Value
Temperature gradient	150 K
Initial time step	1.0 s
Minimal time step	$1 \cdot 10^{-3}$ s
Maximal time step	1.0 s

Further, the MUMPS solver was chosen for deformation but switched to Conjugate Gradient for temperature calculation. In multi-processor calculation, MUMPS is highly recommended for thermal analysis, however, if only one CPU core is available, Conjugate Gradient is favourable in terms of calculation time.

#### 4.4.6 Temperature Response with Optimised Parameters

With run 1 as comparative basis, it was possible to further enhance results by applying the found time dependent thermal conductivity coefficients as described previously. Additionally, thermal efficiency was reduced to  $\eta = 0.25$  instead of the initially assumed  $\eta = 0.30$ , because the overall temperature history tended to overshoot real measurements.

As can be clearly observed in Figure 4.14, all runs describe the process pretty well, which enables further improvements inside the so defined boundaries. Now that the real thermocouple history can be found in the middle of the set experimental range without clipping, interpolation and thus more or less accurate approximation becomes possible. This also proves, that the used brick mesh workaround approach, combined with already known dummy heat sources, is suitable for realistic process description.

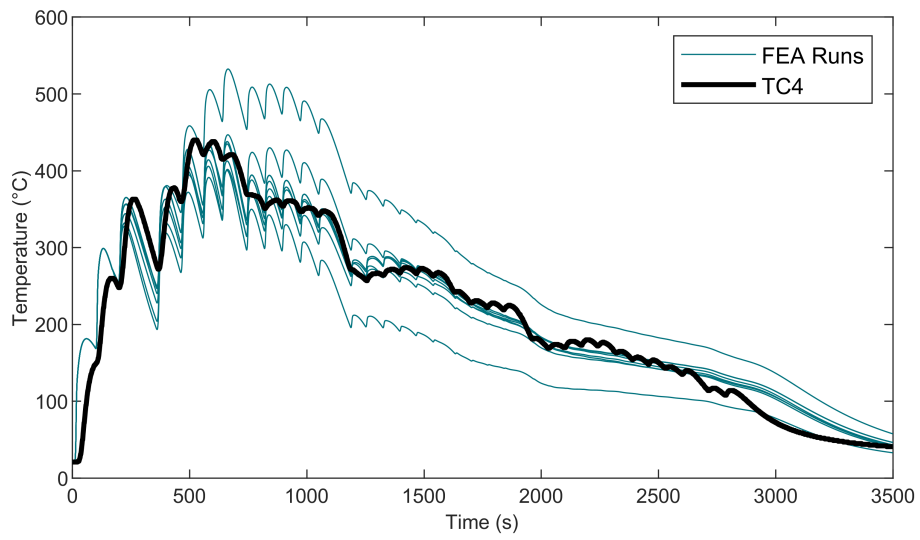


**Figure 4.14:** Visualisation of temperature responses in final validation

## 5 Results

In the following, the achieved main results and findings are presented. The focus lies on a compact and informative recap of the conducted tasks to point out significant findings.

### 5.1 Realistic Heat Source Model

First, the received process data was prepared and processed to extract exact layer timings, as well as detailed movement data. It was possible to build a heat source movement model based on a normalised layer height, which does not need the individual layer height to work.

Inside the DEFORM<sup>®</sup> environment, arc welding is conducted by defining a heat source model in geometric and thermal parameters, which is then moved according to a previously prepared movement table. In case of the heat source's energy density, a normalisation approach was set up to compensate for the rectangular approximation of the welded layers. For this purpose, the volumetric material flow is calculated and compared to the added volume unit per time step inside the rectangular approximation. The resulting DDF (Figure 3.10) is then used to adjust the heating power to match a similar value in energy input per volume unit as in the real process.

Dummy heat sources are introduced to correctly activate each layer. Depending on the weld bead's width, more or less activation volumes are used to cover the whole cross section. All previously accomplished results are combined in one time synchronised heat source model. This is done using a MATLAB<sup>®</sup> script which reads all previous calculations and then formats them into the needed input tables. Additionally, dynamic step size is calculated for simple thermal FEA to save computation time.

## 5.2 Improved Ti-6Al-4V Material Model for Arc Welding

When the standard Ti-6Al-4V material model included in DEFORM<sup>®</sup> is used, data needs to be extrapolated above 1000 °C, which may cause numerical errors up to the extent of failed convergence. By improving and extending the available material model of Ti-6Al-4V, it became possible to stabilise the convergence problems and enhance FEA accuracy. Performing a simple retrofit into a previously conducted analysis confirmed that the model improved the performance and accuracy.

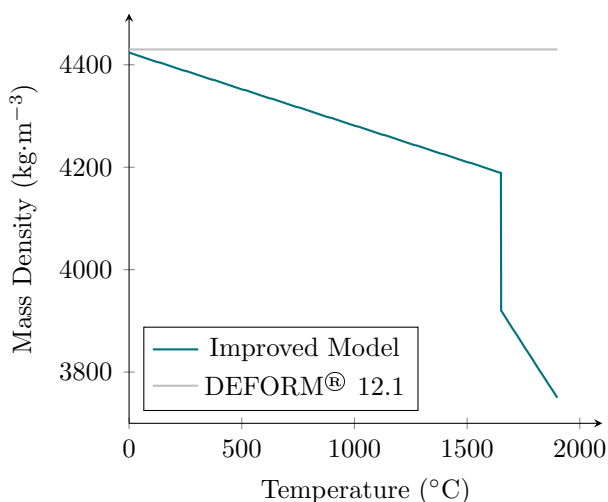


**Figure 5.1:** Mass Density  $\rho$  cf. [62]

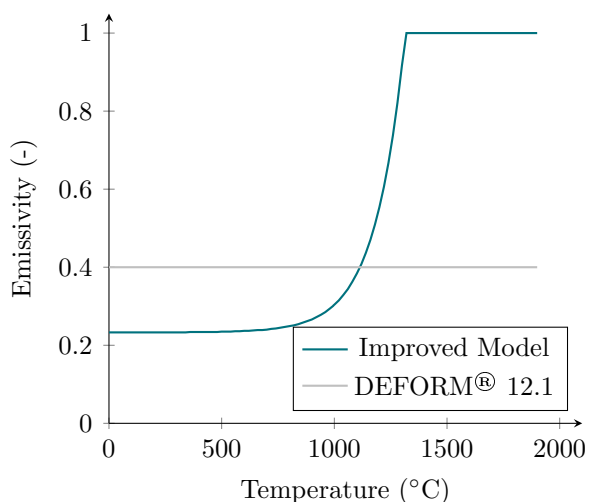


**Figure 5.2:** Emissivity  $\varepsilon_r$  cf. [37, 63]

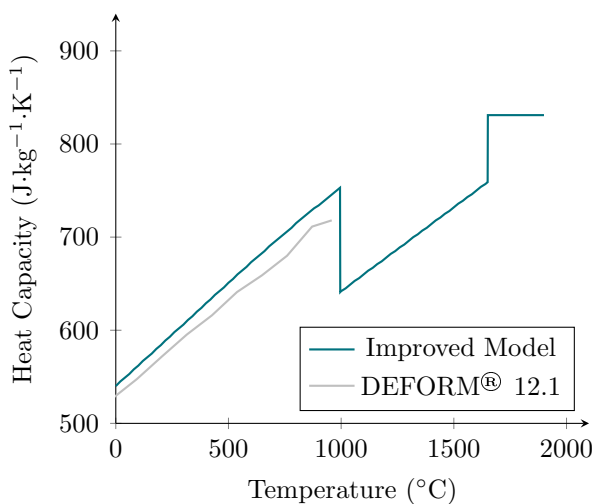


**Figure 5.3:** Heat Capacity  $c_p$  cf. [62]

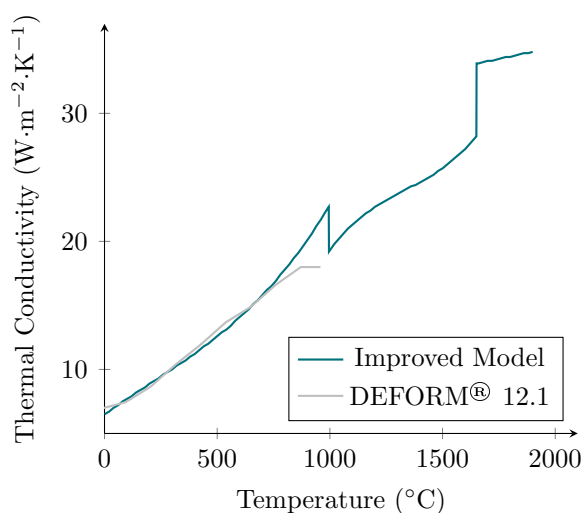


**Figure 5.4:** Thermal Conductivity  $k$  cf. [62]

### 5.3 Parameter Studies

DoE was set up using a CCC design matrix, which promises good accuracy and informative value regarding the parameter range. Influencing parameters were analysed to determine which variables are suitable for a detailed analysis. This resulted in 8 different parameters to be observed, of which 6 regard heat source control and 2 define thermal boundary conditions. To minimise the number of experiments, three different parameter variation runs were conducted, each with a specific focus on different areas of influence.

Each DoE run was individually analysed using MATLAB<sup>®</sup> to automate quadratic RSM. Usually, this type of analysis is used to find optimal parameters of a static and unilateral process. To apply RSM on a time series data set like the ones obtained from FEA thermal history, a custom function was programmed. By applying RSM analysis on a time series, a quadratic surface model is generated for each individual step, which can then be cut along the input parameters cross sections, generating a quadratic function to describe their influence.

As comparative basis, the temperature difference between a thermocouple measurement and FEA thermal history was chosen, resulting in a correlation plot between the absolute temperature deviation and input parameter values, as visualised in Figure 4.3. It was chosen to plot the objectively found best values for each parameter, according to the smallest temperature deviation and confidence interval.

The resulting best value over time curve was then analysed and used as result to adjust FEA. In general, the RMSE regarding temperature can be found below 30 K and statistical accuracy is measured as  $R^2 > 95\%$ , which represents a great success from a mathematical standpoint.

Geometrical parameters were investigated in the first DoE run and found to be influential to the overall temperature distribution. However, the depth parameter  $C_z$  showed high scatter and overall lower influence. A standardised approach is further pursued to normalise FEA as much as possible. The statistical analysis of said first run tended to optimise towards standardised heat source dimensions, which encouraged to fix geometrical parameters as suggested in common literature and proceed with a more detailed analysis of energetic parameters.

Thermal parameters represented a special interest throughout DoE run 2 and 3. Additional information could be extracted to a point at which statements can be made about the time dependent thermal conduction coefficient  $k$  and thermal efficiency  $\eta$ . The empirically found connections between thermal cycles and contact pressure, visualised in Figure 4.12, are one product of this investigation. For thermal efficiency, no sharp statements could be formed.

To sum up these results, all analysed parameters and their theoretically found best values focusing on normalisation are listed in Table 5.1. Basically, this investigation proved that universal heat source parameters, suggest by common literature are suitable inside the DEFORM<sup>®</sup> environment, especially when no detailed process data is available.

**Table 5.1:** Resulting optimal values for all analysed parameters

Description	Variable	Value	Unit
Front ellipsoid apex	$C_f$	0.004	m
Rear ellipsoid apex	$C_r$	0.008	m
Common ellipsoid depth	$C_z$	0.004	m
Common ellipsoid width	$C_y$	0.004	m
Energy distribution factor	$f_f$	0.66	-
Thermal efficiency	$\eta$	0.25	-
Initial element temperature	$T_i$	50	°C
Thermal conduction coefficient	$k$	3 - 12	$\frac{\text{N}}{\text{s}\cdot\text{mm}\cdot\text{K}}$

## 5.4 Resulting Finite Element Model

An improved model was built based on the findings throughout all DoE runs. The conducted experiments in combination with RSM analysis enabled better process knowledge and proved the concept of normalised FE modelling. With manual adjustment according to the obtained information, a very accurate approximation of the real thermal history was possible, as visualised in Figure 5.5 and Figure 5.6. However, from layer 10 onwards, the heat cycle amplitude decays constantly, which does not represent reality perfectly.

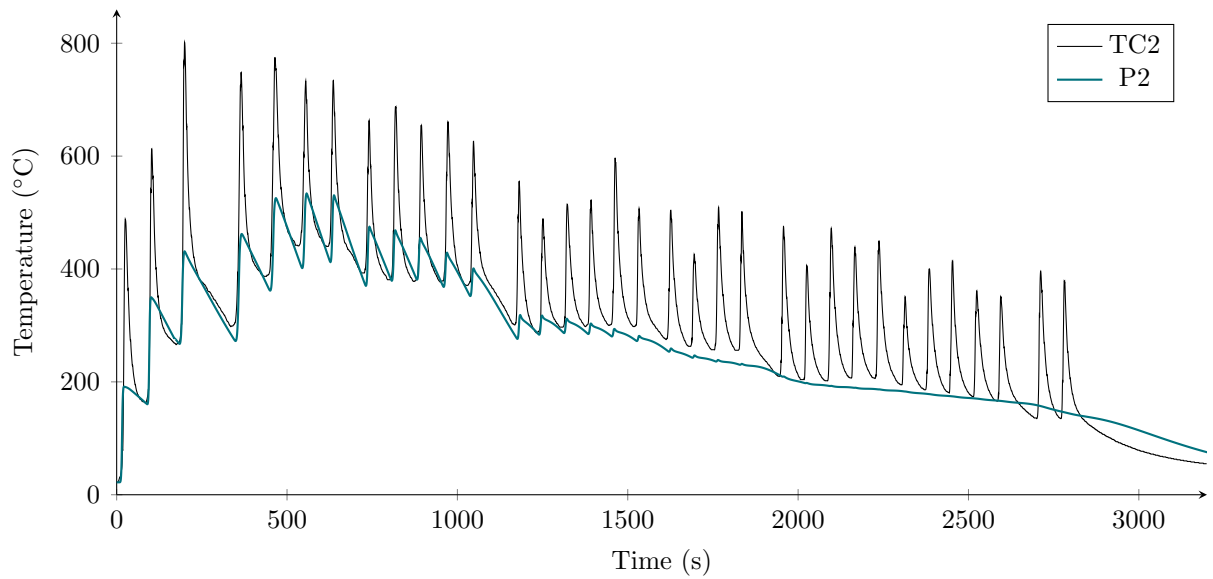


**Figure 5.5:** Final thermal response data for TC2

In both cases, the generated temperature response hits the reference thermocouple measurements especially in cool down times, which is chosen as comparative basis due to its superior stability.

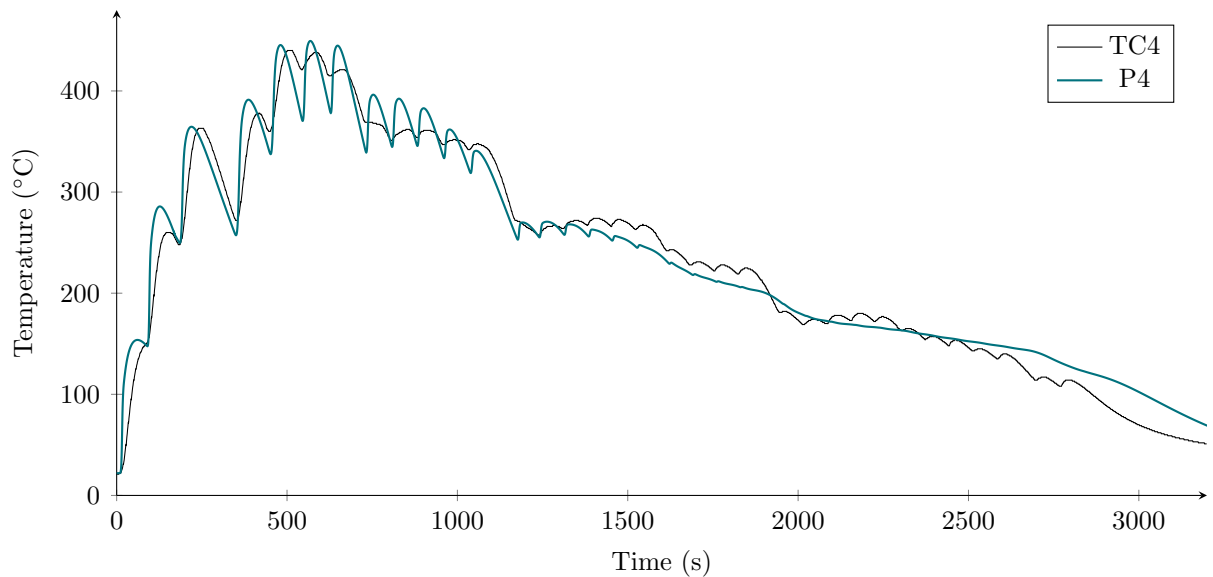


**Figure 5.6:** Final thermal response data for TC4

In addition, an improved approach for the thermo-mechanical analysis inside DEFORM<sup>®</sup> was discovered, reducing the calculation time from about 20 days to 4 days, while retaining the same overall accuracy and drastically improving convergence problems. As described

in chapter 4.4.2, a brick mesh could be utilised instead of the suggested tetrahedral mesh, opening room for simplifications.

After the full thermo-mechanical analysis was conducted, residual stresses and absolute deformation are evaluated. For this purpose, a de-clamping step was added to find equilibrium at the end of the arc welding operation, where clamps are physically removed. The resulting stress and deformation state can be observed in Figure 5.7.

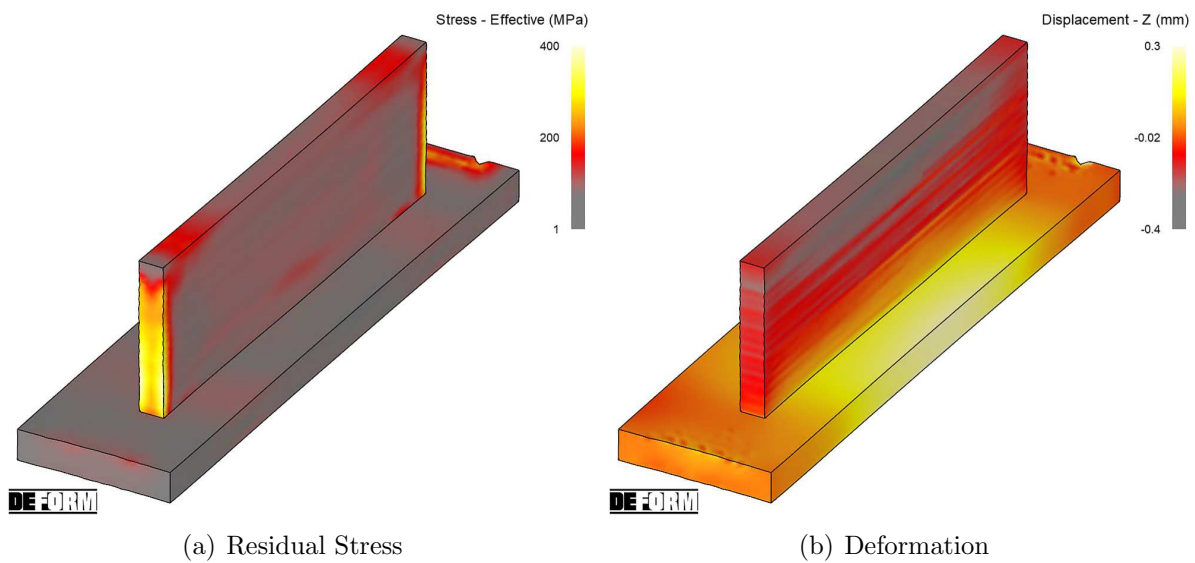


**Figure 5.7:** Resulting residual stress and deformation state after de-clamping



## 6 Discussion

The found results may show potential for improvement or better approaches would be possible under certain conditions. Therefore, challenges and used methods are critically discussed in the following.

### 6.1 Raw Data and Boundary Conditions

There exist many parameters in arc welding, especially in WAAM, which influence the overall accuracy of FE models. To visualise the connections and dependencies between measurable values, all important parameters are shown in Figure 6.1. Black objects represent more or less well known or measured parameters, whereas grey objects show fields of insufficient data or not easy to directly measure process values. The most significant problems regarding raw data are described in greater detail further on.

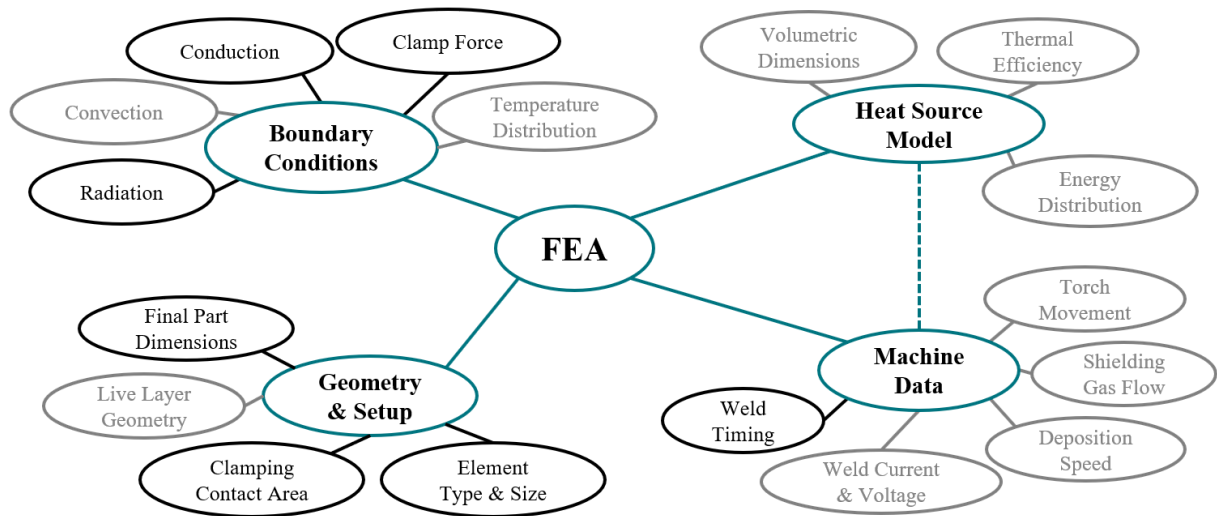


**Figure 6.1:** Visualisation of the measurements and process data influencing FEA

Raw data was provided through .txt configuration files of the manufacturing machines. Hard coded welding delays and feed speeds are used to control the plasma torch. It is common practice to manually or automatically adjust welding parameters mid-process, which ensures stability. This however influences the heat source's parameters, movement speed and layer height, which leads to rather drastic differences in an idealised model and the real experiment. Since this procedure is more or less individual for each manufacturing

job, real time process data is mandatory for an accurate replication. In this case, no live data was available, which led to the development of a MATLAB<sup>®</sup> tool to extract exact layer timing and deposition settings, described in chapter 3.2.2, to somehow realistically replicate the manufacturing experiment. However, this approach comes with obvious flaws, like the inability to recognise the mid-layer feed rate or travel speed changes. Everything is „normalised“ in layer wise calculation steps, leaving significant gaps in the raw data for future improvement capabilities because no live geometry measurement was possible.

When considering thermal conduction, it becomes very hard to determine the time dependent influence of deformation due to a build up of residual stresses. As found in DoE run 3, an overall assumption of  $k = 8 \frac{\text{N}}{\text{mm}\cdot\text{s}\cdot\text{K}}$  seems to fit the process well when using sticking conditions to assure convergence in FEA. However, in reality, the contact surfaces do not stick together, therefore deformation analysis needs to be considered. This on the other hand increases the calculation time by a lot and therefore is not really practical. Also the distribution between the welding table and clamp heat flux is not known. In practise, the contact pressure is raised on clamps but overall contact between the substrate and table is reduced due to lifting corners and general bulging of the substrate. This logically leads to a pressure dependent definition of thermal conduction, which is possible in DEFORM<sup>®</sup> but not known in this practical example, which opens up rather simple possibilities for improvement.

As can be observed in the resulting thermal history (Figure 5.6), the heat cycle amplitudes decay to a point of nearly constant development. This might be due to the neglect of thermal efficiency, which could not be mapped qualitatively in this study. Furthermore, thermocouples were loosely mounted on the substrate, which definitely falsifies the reference data to some extent. Since FEA can read temperature values directly from nodes, the real measurements inside drilled holes will always deviate a little bit, which explains higher amplitudes in early layers. Additionally, thermocouple wires are directly exposed to the process atmosphere, which can substantially heat up and thus falsify the measurements. From this perspective, the obtained FEA temperature response curve with a decaying amplitude might be more correct than real measurements, because such influences can be ruled out.

## 6.2 Methodic Implementation

Due to poor process control, targeted geometries can not be achieved with ease, which makes realistic modelling very hard. Therefore, the proposed normalisation of the model was used. It would be better to model each layer separately and load them into FEA via sub routines. However, as previously mentioned, there is not enough process data available to correctly do so. Especially the geometrical weld bead information, needed for a detailed model of the individual layers, is missing. Moreover, such detailed modelling approaches cause an even greater increase in calculation complexity and raises new challenges considering sub routines and layer separation.

Besides the different options for mesh activation, the activation volume can be determined as a big influencing variable. DEFORM<sup>®</sup> offers the option to choose an activation radius, therefore providing a quadratic cross section in the heat source's center, as described in chapter 2.3.7.3. Although this might not be an ideal solution in terms of accuracy, it is easier in handling, especially considering user routines and modifications outside the user interface, which impede easy adaptability and understanding. Therefore it is chosen to leave the settings found in chapter 3.3.5 and focus on other, more important influencing parameters.

Thermal history was compared to the temperature response curves using a differential approach. It showed, that different influencing parameters like the coefficient of thermal conduction  $k$  and heat distribution caused a significant shift in the temperature response. This behaviour could be further utilised to compare not only absolute temperature difference per time step, but also its gradient and absolute time shift. Data analysis was conducted using RSM and statics, which are more or less suited for this application. In retrospect, a more detailed and measurement backed investigation of thermal boundary conditions and heat transfer coefficients would have made more sense. This way, the physical behaviour could have been modelled better, which then enables ML or more detailed RSM approaches to fit the geometrical heat source parameters based on a grey box model.

Friction coefficients between the contacting surfaces were assumed as constant values, when they are dependent on contact pressure in reality. However, this setting is not too critical because no movement besides thermal expansion is expected.

Thermal FEA was used throughout all variation runs, because it calculates quickly and does not cause convergence problems as often as full thermo-mechanical analysis. However, one thermo-mechanical analysis run was conducted based on the final model to investigate the impact of deformation on the thermal history, which highlighted many problems, as will be discussed later on.

### 6.3 Influence and Effect of Parameters

To verify the thermal history data and thus accuracy of the chosen distribution factor  $f_f$ , holistic thermal camera pictures or equivalent would be needed. Although the FEA approximates TC4 pretty accurately, nothing can be said about the front to rear energy distribution of the heat source, which greatly influences the wire melting behaviour, local thermal stress and grain structure. Further verification complications arise when thermocouples are compared to point tracking, because of latency and progressing distancing of the heat source from the measured nodes. From layer 10 upwards, the temperature response curve can only be seen as rough guidance, because no connection to the in-layer temperature distribution can be made.

Considering geometric heat source parameters, the front and rear expansion are found to be most influential, however they are strongly connected to the energy distribution, which makes this result hard to verify. The weld pool's depth seems to have a little impact over all, which is why a standardised depth is chosen for general analysis.

Thermal efficiency and contact heat transfer showed to be most influential. At the same time, they are hard to physically verify, which makes investigations like this necessary. A time dependent conductivity was empirically found to realistically model thermal history, however thermal efficiency remains an unknown variable at this point. In-line measurements need to be conducted to eliminate its influence from the list of needed parameter for variation to verify the assumed conductivity functions.

In general, all observed parameters will be time dependent in real experiments, which complicates investigations. However, it is possible to assume many parameters as constant due to their rather small overall influence and focus on more influential parameters. Further verification data is definitely needed, but a good overview and comparative basis for future investigations could be built.

## 6.4 Multi-Layer Arc Welding in DEFORM<sup>®</sup> 12.1

DEFORM<sup>®</sup> can be used to describe arc welding processes. However, especially when building multi-layered structures like WAAM does, it comes to inconveniences and problems. First and foremost, there is no built in solution for the layer-wise mesh activation. A workaround using a combination of a simplified brick mesh and the arc welding module, as described in chapter 4.4.2, could be achieved. This finding represents a major achievement for WAAM FEA in DEFORM<sup>®</sup> on which can be built in future approaches. However, access to arc welding and heat source parameters through user routines is limited and inconvenient to handle, especially when compared to other FE tools, which allow direct and individual access including automation possibilities through python scripts.

The implementation of dynamic arc welding process parameters is nearly impossible at this point. Geometrical heat source parameters or the heat distribution inside the weld pool can only be accessed through 3D operation blocks. Inside said operations, only static values can be established, which results in the need of a new operation block as soon as a parameter is changed. This is highly impractical and causes a lot of manual labour regarding adjustment, contact definition and boundary conditions. In case of a process change, every block needs to be adjusted individually, which is unacceptable for automated calculation approaches and also causes a lot of possible human errors. Furthermore, the needed computation time is increased drastically because informations need to be passed on between operations, causing repeated initiation phases.

Further, thermal boundary conditions are strongly dependent on the chosen contact settings. Node shifting due to deformation often causes convergence problems, therefore strategic fixations or connections need to be established. However, these settings should not influence the thermal history too much to remain accurate. If the substrate plate is fixed onto the table by velocity boundary conditions, the heat flux contact property is not calculated properly anymore, which immensely falsifies thermal history by keeping too much heat in the substrate. Alternatively, the substrate can be kept unfixed and sticking contact between the table, substrate and clamps can be applied. This however establishes constant and thus unrealistic contact surfaces, which lead to a higher heat flux to the surroundings, also falsifying the thermal history significantly. Differences are shown as an example in Figure 6.2, where the thermal history of the preheating phase can be observed.

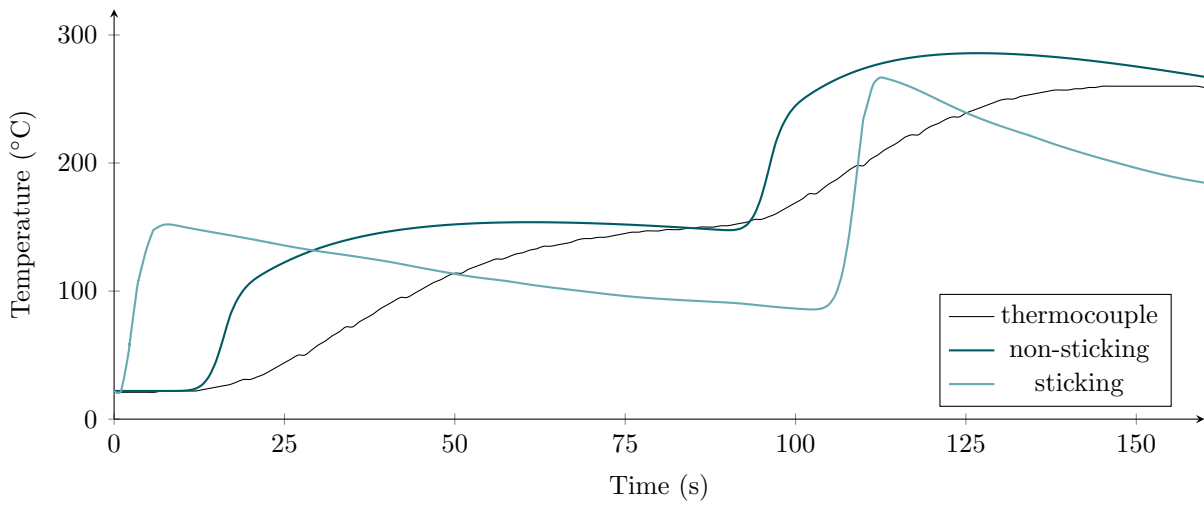


**Figure 6.2:** Difference between sticking and non-sticking contact settings

Especially the thermo-mechanical analysis needs further improvement regarding its boundary conditions and fixations to realistically model the process. At some points, unrealistic deformations occur due to necessary x and y axis fixations of the substrate resulting from convergence problems or an unrealistic thermal history if built differently. Free distortion boundary conditions promise a relatively stable calculation without messing with contact properties. However, when building additive mesh structures on previously deformed surfaces, convergence problems arise again.

## 7 Conclusion and Outlook

This thesis focused on the detailed feasibility study of DEFORM<sup>®</sup> in multi-layer arc welding. DoE was used to statistically analyse a previously built and tested FE model regarding several influencing parameters, primarily affecting the heat source and thermal boundary conditions. While investigating the conducted experiments in MATLAB<sup>®</sup>, several points of insufficient data were discovered. Although statistical analysis returned promising results regarding optimal process parameters, the uncertainty of realistic development remains. Simply too many process parameters are either approximated as static, or insufficiently measured in the first place. It became clear, that several parameters need to be measured and then imported into the analysis, to get good informative value of other, not as easy to measure parameters. These findings lead to the proposed outlook and possible approaches for future investigations.

### 7.1 Dynamic Process Values

As of now, static values are often chosen for boundary conditions. In order to improve the accuracy and build a useable model, digital transformation and thus the approach for enhanced communication is inevitable. Live measurement of contact pressures and the temperature distribution are essential for a future model validation. In this context, a detailed g-code file or equivalent live machine movement data is mandatory for an accurate replication of the process.

Especially in the heat source model, many parameters are estimated or found empirically for each setup, which represents a large effort in manual labour. Additionally, thermal efficiency  $\eta$  and geometrical heat source parameters are most likely not constant over time, which needs further investigation. Weld pool observation and detailed measurements of the electrical power consumption lead the way to a better understanding of the heat source's behaviour. However, this topic is rather hard to investigate due to a lack of sufficient in-line measurement equipment and analysing methods.

Additionally, influences like the area of contact between the substrate and welding table, active table cooling, argon atmosphere temperature and flow, as well as dynamically adapted welding parameters should be considered in future approaches. Even if they are not used in analysis, they might provide insight to verify a certain behaviour.

To consider the contact pressure and heat flux to clamps, a measurement setup containing thermocouples and strain gauges is suggested to fit onto the welding clamps. Once pressure dependent thermal conduction is determined, a simplified FE model using rigid clamp objects can be built on this findings to save calculation time. The clamping force is in general of great interest for future approaches. Therefore, integration of a strain or force measurement into specialised welding clamps is suggested for the live measurement and bilateral communication between the experiment and FEA.

### **7.2 Improved Temperature Measurement**

Over the course of this investigation, it became clear, that the surface thermocouples are greatly influenced by arc strikes and bypassing hot gases, which makes them rather unreliable for process optimisation. Subsurface thermocouples, like the comparative basis TC4, can be seen as more stable. However, better contact inside the drilled hole promises an even better accuracy in the future, especially considering the amplitudes and their decaying behaviour.

A measurement system consisting of a thermocouple, heat conductive paste and a conical clamping screw is suggested. By applying the thermal paste on the probes inside a drilled hole and clamping them in place, shifting can be controlled and air gaps can be prohibited. Several holes can be drilled into the substrate right beneath the weld pool, which promises better observation capabilities regarding the real heat distribution in the heat source, at least in the first layers.

### **7.3 Automation and Digitalisation**

It became obvious that at least unidirectional communication between the manufacturing machine and FEA needs to be established to receive a realistic model. Process data is often logged in one second intervals, or not even saved at all. Some parameters are assumed as constant in the initial setup, which potentially produces errors that can not be observed



without sufficient data. Therefore, a data driven approach is suggested, which eventually results in a digital shadow. Only then the experiment can be modelled to a satisfactory extent and further optimised by using automated algorithms or ML approaches to address the complex time dependent behaviour of WAAM.

To achieve this, a layer-less model based on the precise heat source travel data is suggested. This can be possible by dynamically applying in-situ measured weld pool information like the temperature distribution, arc position or geometric proportions in FEA. The so gathered real data can then be imported, where it grants advanced flexibility and accuracy regarding the weld bead's geometry and dynamic layer height.

## **7.4 Advanced Statistical Analysis and Machine Learning**

As previously described in chapter 4.2.5, statistical analysis and RSM is limited when applied to a time series data set. It can be conducted to quickly gather information about the individual parameter influence through DoE, however it becomes very experimentally intense and hard to analyse when applied to a system with several unknown parameters. Therefore, a combination of live process data and ML is suggested to fit the time dependent data more quickly.

Probably the most important point to apply this type of analysis to is the weld pool's behaviour. In combination with a proper digital shadow, which returns all easy to measure process data into FEA, only hard to measure weld pool parameters will remain. A data driven black or grey box model is suggested to then find general correlation between the thermal history and heat source parameters. When applied correctly, this model should be able to effectively predict heat source parameters depending on the environmental influences and therefore be used to generate time dependent process parameters.

# List of Figures

2.1	Schematic overview of welding technologies used in WAAM cf. [10]	4
2.2	Weld bead parameters in dependence of wire feed rate and diameter [20]	5
2.3	Possible in-layer deposition strategies [7]	6
2.4	Cooling rate in dependence of different process parameters [20]	7
2.5	Planar bending moment introduced by accumulated residual stress [5]	8
2.6	Possible elements for practical 3D FEA [48]	15
2.7	Reduced mesh with local refinement in the HAZ [23]	16
2.8	Deposition strategy optimised for solid infill with a constant layer height [49]	17
2.9	Experimental verification of the overlapping corner optimization [19]	17
2.10	Schematic cross sections of weld bead modelling approaches	18
2.11	Schematic diagram of the GDE and its parameters [52]	21
2.12	Influence visualisation of the introduced form parameter $\lambda$ [52]	22
2.13	Elliptical consideration of the energy input of the added weld bead [52]	22
2.14	Rectangular consideration of the energy input of the added weld bead [24]	23
2.15	Schematic representation of hybrid element activation [22]	25
2.16	Central composite design methods for quadratic response surface models [60]	29
2.17	Visualisation of the Box-Behnken quadratic model [60]	30
3.1	Picture of the manufactured single wall	31
3.2	Visualisation of coordinate and movement setup in the single wall experiment	32
3.3	Visualisation of the thermocouple placement on the substrate top surface	32
3.4	3D model of the to be manufactured single wall	34
3.5	Layer timing extraction from the raw temperature data of TC2	35
3.6	Layer duration differences resulting from manual interventions	36
3.7	Modelling of the fed and molten wire volume in a welded layer	36
3.8	Description of movement in machine code	37
3.9	Visualisation of the implementation strategy for wire feed at reversal points	38
3.10	Reduced heat source magnitude according to deposition difference	39
3.11	Dynamic time step duration control while welding	44
3.12	Validation of the proposed material model with previous investigations	45
3.13	Visualisation of geometry placement in DEFORM <sup>®</sup>	46
3.14	Visualisation of operation blocks used to model the welding process	48
3.15	Example for surfaces involved in thermal convection to the environment	49
3.16	Table of contact properties between all used objects	50

3.17	Increase of the contact heat transfer coefficient $k$ due to distortion . . . . .	50
3.18	Schematic diagram of the forces acting on threads when under load [64] . . .	51
3.19	Schematic diagram of force distribution in clamping systems . . . . .	52
3.20	Visualisation of clamp force applied as boundary condition . . . . .	53
3.21	Heat source settings inside the DEFORM <sup>®</sup> arc welding environment . . . .	54
3.22	Visualisation of the thermocouple positions while welding in DEFORM <sup>®</sup> . .	55
4.1	Impact of mesh size and time step size on activation accuracy . . . . .	58
4.2	Visualisation of the time sampled temperature difference approach . . . . .	60
4.3	Handling of special cases in RSM analysis of individual timestamps . . . .	64
4.4	RSM analysis applied on a time series . . . . .	67
4.5	Optimal parameters of the custom time series RSM analysis for run 1 . . . .	68
4.6	Visualisation of temperature responses in run 1 . . . . .	69
4.7	Optimal parameters of the custom time series RSM analysis for run 2 . . . .	70
4.8	Visualisation of temperature responses in run 2 . . . . .	70
4.9	Optimal parameters of the custom time series RSM analysis for run 3 . . . .	71
4.10	Visualisation of temperature responses in run 3 . . . . .	72
4.11	Visualisation of the introduced mixed mesh setup . . . . .	74
4.12	Experimentally found thermal conduction coefficients over time . . . . .	75
4.13	Contact settings for the realistic modelling of deformation . . . . .	76
4.14	Visualisation of temperature responses in final validation . . . . .	78
5.1	Mass Density $\rho$ cf. [62] . . . . .	80
5.2	Emissivity $\varepsilon_r$ cf. [37, 63] . . . . .	80
5.3	Heat Capacity $c_p$ cf. [62] . . . . .	80
5.4	Thermal Conductivity $k$ cf. [62] . . . . .	80
5.5	Final thermal response data for TC2 . . . . .	83
5.6	Final thermal response data for TC4 . . . . .	83
5.7	Resulting residual stress and deformation state after de-clamping . . . . .	84
6.1	Visualisation of the measurements and process data influencing FEA . . . .	85
6.2	Difference between sticking and non-sticking contact settings . . . . .	90

# List of Tables

3.1	Log-File torch information . . . . .	33
3.2	Log-File timing information . . . . .	33
3.3	Target dimensions of the to be manufactured single wall model . . . . .	34
3.4	Measured dimensions of the finished single wall and their variation . . . . .	34
3.5	Maximum dimensions of all generated 3D objects inside DEFORM <sup>®</sup> . . . . .	46
3.6	Mesh information for all objects involved in the analysis setup . . . . .	47
3.7	Flank diameter and pitch angle of common metric thread sizes [64] . . . . .	52
3.8	Values needed to calculate clamp forces . . . . .	53
3.9	Coordinates entered in DEFORM <sup>®</sup> to track thermocouples . . . . .	55
4.1	Heat source parameters available in DEFORM <sup>®</sup> 12.1 . . . . .	57
4.2	Process parameters and their range for DoE run 1 . . . . .	68
4.3	Process parameters and their range for DoE run 2 . . . . .	69
4.4	Process parameters and their range for DoE run 3 . . . . .	71
4.5	Normalised heat source parameters for the GDE . . . . .	73
4.6	Mesh information for all objects involved in final validation . . . . .	74
4.7	Coulomb friction used for all occurring material pairs . . . . .	76
4.8	Dynamic time step size settings for final validation . . . . .	77
5.1	Resulting optimal values for all analysed parameters . . . . .	82
A.1	Exported datapoints for the improved material model of Ti-6Al-4V . . . . .	104
B.1	Tabulated experimental plan for parameter variation run 1 . . . . .	105
B.2	Tabulated experimental plan for parameter variation run 2 . . . . .	106
B.3	Tabulated experimental plan for parameter variation run 3 . . . . .	107

# Bibliography

- [1] Marcel Czipin. “Simulationsstudie von additiv gefertigtem Ti-6Al-4V”. Bachelor Thesis. Leoben: University of Leoben, 2022.
- [2] Martin Bielik. “Thermo-mechanical analysis of plasma-based additive manufacturing of Ti-6Al-4V components using Simufact Welding 8.0”. Master Thesis. Vienna: Vienna University of Technology, June 2020.
- [3] S. W. Williams et al. “Wire + Arc Additive Manufacturing”. In: *Materials Science and Technology* 32.7 (2016), pp. 641–647. DOI: 10.1179/1743284715Y.0000000073.
- [4] Keval P. Prajadhama et al. “Development of Bead Modelling for Distortion Analysis Induced by Wire Arc Additive Manufacturing using FEM and Experiment”. In: *MATEC Web of Conferences* 269 (2019), p. 05003. DOI: 10.1051/mateconf/201926905003.
- [5] Haibin Geng et al. “Theoretical Model of Residual Stress and Warpage for Wire and Arc Additive Manufacturing Stiffened Panels”. In: *Metals* 10.5 (2020), p. 666. DOI: 10.3390/met10050666.
- [6] Chunyang Xia et al. “A review on wire arc additive manufacturing: Monitoring, control and a framework of automated system”. In: *Journal of Manufacturing Systems* 57 (2020), pp. 31–45. ISSN: 02786125. DOI: 10.1016/j.jmsy.2020.08.008.
- [7] Bilal Ahmad et al. “Influence of Deposition Strategies on Residual Stress in Wire + Arc Additive Manufactured Titanium Ti-6Al-4V”. In: *Metals* 12.2 (2022), p. 253. DOI: 10.3390/met12020253.
- [8] Fronius International GmbH. *Wire Arc Additive Manufacturing: Economical 3d-printing for metal*. URL: <http://www.froniusexplorer.com/en-gb/uk/welding-technology/info-centre/press/waam>.
- [9] Sudhanshu Ranjan Singh and Pradeep Khanna. “Wire arc additive manufacturing (WAAM): A new process to shape engineering materials”. In: *Materials Today: Proceedings* 44 (2021), pp. 118–128. ISSN: 22147853. DOI: 10.1016/j.matpr.2020.08.030.
- [10] Hans J. Fahrenwaldt, Volkmar Schuler, and Herbert Wittel. *Praxiswissen Schweißtechnik: Werkstoffe, Prozesse, Fertigung*. 4., überarb. Aufl., 2011. Praxis. Wiesbaden: Vieweg + Teubner, 2012. ISBN: 9783834881991. DOI: 10.1007/978-3-8348-8199-1.

- [11] Xingwang Bai et al. “Numerical analysis of heat transfer and fluid flow in multilayer deposition of PAW-based wire and arc additive manufacturing”. In: *International Journal of Heat and Mass Transfer* 124 (2018), pp. 504–516. ISSN: 00179310. DOI: 10.1016/j.ijheatmasstransfer.2018.03.085.
- [12] Yan Li, Chen Su, and Jianjun Zhu. “Comprehensive review of wire arc additive manufacturing: Hardware system, physical process, monitoring, property characterization, application and future prospects”. In: *Results in Engineering* 13 (2022), p. 100330. ISSN: 25901230. DOI: 10.1016/j.rineng.2021.100330.
- [13] Posch Gerhard et al. “MANUFACTURING OF TURBINE BLADES BY SHAPE GIVING CMT-WELDING”. In: 2014. URL: [https://www.researchgate.net/profile/gerhard-posch/publication/268778936\\_manufacturing\\_of\\_turbine\\_blades\\_by\\_shape\\_giving\\_cmt-welding](https://www.researchgate.net/profile/gerhard-posch/publication/268778936_manufacturing_of_turbine_blades_by_shape_giving_cmt-welding).
- [14] A. Sahoo and S. Tripathy. “Development in plasma arc welding process: A review”. In: *Materials Today: Proceedings* 41 (2021), pp. 363–368. ISSN: 22147853. DOI: 10.1016/j.matpr.2020.09.562.
- [15] A. Horgar et al. “Additive manufacturing using WAAM with AA5183 wire”. In: *Journal of Materials Processing Technology* 259 (2018), pp. 68–74. ISSN: 09240136. DOI: 10.1016/j.jmatprotec.2018.04.014.
- [16] Abdulrahman Shuaibu Ahmad et al. “Finite Element Prediction of Residual Stress and Deformation Induced by Double-Pass TIG Welding of Al 2219 Plate”. In: *Materials (Basel, Switzerland)* 12.14 (2019). ISSN: 1996-1944. DOI: 10.3390/ma12142251.
- [17] Adeel Ikram and Hyun Chung. “Numerical simulation of arc, metal transfer and its impingement on weld pool in variable polarity gas metal arc welding”. In: *Journal of Manufacturing Processes* 64 (2021), pp. 1529–1543. ISSN: 15266125. DOI: 10.1016/j.jmapro.2021.03.001.
- [18] Mariacira Liberini et al. “Selection of Optimal Process Parameters for Wire Arc Additive Manufacturing”. In: *Procedia CIRP* 62 (2017), pp. 470–474. ISSN: 22128271. DOI: 10.1016/j.procir.2016.06.124.
- [19] Donghong Ding et al. “A shape control strategy for wire arc additive manufacturing of thin-walled aluminium structures with sharp corners”. In: *Journal of Manufacturing Processes* 64 (2021), pp. 253–264. ISSN: 15266125. DOI: 10.1016/j.jmapro.2021.01.029.

- [20] W. Ou et al. “Fusion zone geometries, cooling rates and solidification parameters during wire arc additive manufacturing”. In: *International Journal of Heat and Mass Transfer* 127 (2018), pp. 1084–1094. ISSN: 00179310. DOI: 10.1016/j.ijheatmasstransfer.2018.08.111.
- [21] Jiankang Huang et al. “A 3D dynamic analysis of different depositing processes used in wire arc additive manufacturing”. In: *Materials Today Communications* 24 (2020), p. 101255. ISSN: 23524928. DOI: 10.1016/j.mtcomm.2020.101255.
- [22] Donghong Ding et al. “The well-distributed volumetric heat source model for numerical simulation of wire arc additive manufacturing process”. In: *Materials Today Communications* 27 (2021), p. 102430. ISSN: 23524928. DOI: 10.1016/j.mtcomm.2021.102430.
- [23] R. M. Farias, P.R.F. Teixeira, and L. O. Vilarinho. “An efficient computational approach for heat source optimization in numerical simulations of arc welding processes”. In: *Journal of Constructional Steel Research* 176 (2021), p. 106382. ISSN: 0143974X. DOI: 10.1016/j.jcsr.2020.106382.
- [24] Filippo Montevercchi et al. “Finite Element Modelling of Wire-arc-additive-manufacturing Process”. In: *Procedia CIRP* 55 (2016), pp. 109–114. ISSN: 22128271. DOI: 10.1016/j.procir.2016.08.024.
- [25] Francis H. Froes and Rodney Boyer, eds. *Additive manufacturing for the aerospace industry*. Elsevier, 2019. ISBN: 9780128140628.
- [26] Joel C. Najmon, Sajjad Raeisi, and Andres Tovar. “Review of additive manufacturing technologies and applications in the aerospace industry”. In: *Additive manufacturing for the aerospace industry*. Ed. by Francis H. Froes and Rodney Boyer. Elsevier, 2019, pp. 7–31. ISBN: 9780128140628. DOI: 10.1016/B978-0-12-814062-8.00002-9.
- [27] Hui Huang et al. “Toward large-scale simulation of residual stress and distortion in wire and arc additive manufacturing”. In: *Additive Manufacturing* 34 (2020), p. 101248. ISSN: 22148604. DOI: 10.1016/j.addma.2020.101248.
- [28] C. Wang et al. “Machine learning in additive manufacturing: State-of-the-art and perspectives”. In: *Additive Manufacturing* 36 (2020), p. 101538. ISSN: 22148604. DOI: 10.1016/j.addma.2020.101538.
- [29] Olivier Champagne and Xuan-Tan Pham. “Numerical simulation of moving heat source in arc welding using the Element-free Galerkin method with experimental validation and numerical study”. In: *International Journal of Heat and Mass Transfer* 154 (2020), p. 119633. ISSN: 00179310. DOI: 10.1016/j.ijheatmasstransfer.2020.119633.

- [30] Hisaya Komen et al. “Numerical Investigation of Heat Transfer During Submerged Arc Welding Phenomena by Coupled DEM-ISPH Simulation”. In: *International Journal of Heat and Mass Transfer* 171 (2021), p. 121062. ISSN: 00179310. DOI: 10.1016/j.ijheatmasstransfer.2021.121062.
- [31] S. Trupiano et al. “A novel modeling approach for multi-passes butt-welded plates”. In: *Journal of Thermal Stresses* 44.7 (2021), pp. 829–849. ISSN: 0149-5739. DOI: 10.1080/01495739.2021.1916415.
- [32] Øystein Grong. *Metallurgical modelling of welding*. 2. ed. Vol. 677. Materials modelling series. London: The Institute of Materials, 1997. ISBN: 1861250363.
- [33] A. El Bakali et al. “Effect of oxidation on spectral and integrated emissivity of Ti-6Al-4V alloy at high temperatures”. In: *Journal of Alloys and Compounds* 889 (2021), p. 161545. ISSN: 09258388. DOI: 10.1016/j.jallcom.2021.161545.
- [34] L. González-Fernández et al. “Infrared normal spectral emissivity of Ti-6Al-4V alloy in the 500–1150K temperature range”. In: *Journal of Alloys and Compounds* 541 (2012), pp. 144–149. ISSN: 09258388. DOI: 10.1016/j.jallcom.2012.06.117.
- [35] F. Pixner et al. “Contactless temperature measurement in wire-based electron beam additive manufacturing Ti-6Al-4V”. In: *Welding in the World* 65.7 (2021), pp. 1307–1322. ISSN: 0043-2288. DOI: 10.1007/s40194-021-01097-0.
- [36] Matteo Villa et al. “Metallurgical Modelling of Ti-6Al-4V for Welding Applications”. In: *Metals* 11.6 (2021), p. 960. DOI: 10.3390/met11060960.
- [37] Samy Hocine, Helena van Swygenhoven, and Steven van Petegem. “Verification of selective laser melting heat source models with operando X-ray diffraction data”. In: *Additive Manufacturing* 37 (2021), p. 101747. ISSN: 22148604. DOI: 10.1016/j.addma.2020.101747.
- [38] Scientific Forming Technologies Corporation. *DEFORM® Documentation*. 2021.
- [39] Laukik P. Raut and Ravindra V. Taiwade. “Wire Arc Additive Manufacturing: A Comprehensive Review and Research Directions”. In: *Journal of Materials Engineering and Performance* 30.7 (2021), pp. 4768–4791. ISSN: 1059-9495. DOI: 10.1007/s11665-021-05871-5.
- [40] T. D. Dinh et al. “A unified approach to model the effect of porosity and high surface roughness on the fatigue properties of additively manufactured Ti6-Al4-V alloys”. In: *Additive Manufacturing* 33 (2020), p. 101139. ISSN: 22148604. DOI: 10.1016/j.addma.2020.101139.



- [41] Bin Sun et al. “Controlling the Microstructure and Properties of Plasma Arc Additively Manufactured Ti-6Al-4V Alloy Through Heat Treatment”. In: *SSRN Electronic Journal* (2022). DOI: 10.2139/ssrn.4053494.
- [42] Xiangman Zhou et al. “Three-dimensional numerical simulation of arc and metal transport in arc welding based additive manufacturing”. In: *International Journal of Heat and Mass Transfer* 103 (2016), pp. 521–537. ISSN: 00179310. DOI: 10.1016/j.ijheatmasstransfer.2016.06.084.
- [43] Zeyu Zhou et al. “Thermal field prediction for welding paths in multi-layer gas metal arc welding-based additive manufacturing: A machine learning approach”. In: *Journal of Manufacturing Processes* 64 (2021), pp. 960–971. ISSN: 15266125. DOI: 10.1016/j.jmapro.2021.02.033.
- [44] VICTOR USTINOV et al. “Modellentwicklung für den kontaktdruckabhängigen Wärmeübergang”. In: *MTZ - Motortechnische Zeitschrift* 72.2 (2011), pp. 142–147. ISSN: 0024-8525. DOI: 10.1365/s35146-011-0034-2.
- [45] R. Sepe et al. “Influence of thermo-mechanical material properties on the structural response of a welded butt-joint by FEM simulation and experimental tests”. In: *Forces in Mechanics* 4 (2021), p. 100018. ISSN: 26663597. DOI: 10.1016/j.finmec.2021.100018.
- [46] R. Gokulakrishnan R. Sriram et al. “Finite element simulation of temperature distribution and residual stress in single bead on plate weld trial using double ellipsoidal heat source model”. In: *International Journal of Recent Technology and Engineering* 8.1S2 (2019), pp. 133–138.
- [47] P. K. Taraphdar et al. “Significance of Finite Element Models and Solid-State Phase Transformation on the Evaluation of Weld Induced Residual Stresses”. In: *Metals and Materials International* 27.9 (2021), pp. 3478–3492. ISSN: 1598-9623. DOI: 10.1007/s12540-020-00921-4.
- [48] Singiresu S. Rao. *The finite element method in engineering*. Sixth edition. Kidlington, Oxford, United Kingdom: Butterworth-Heinemann an imprint of Elsevier, 2018.
- [49] Yongzhe Li et al. “Enhanced beads overlapping model for wire and arc additive manufacturing of multi-layer multi-bead metallic parts”. In: *Journal of Materials Processing Technology* 252 (2018), pp. 838–848. ISSN: 09240136. DOI: 10.1016/j.jmatprotec.2017.10.017.
- [50] Jörn Mehnert et al. “Design study for wire and arc additive manufacture”. In: *International Journal of Product Development* 19.1/2/3 (2014), p. 2. ISSN: 1477-9056. DOI: 10.1504/IJPD.2014.060028.

- [51] X. Shan et al. “Thermo-mechanical modelling of a single-bead-on-plate weld using the finite element method”. In: *International Journal of Pressure Vessels and Piping* 86.1 (2009), pp. 110–121. ISSN: 03080161. DOI: 10.1016/j.ijpvp.2008.11.005.
- [52] Oleg Mokrov et al. *A fine modification of the double ellipsoid heat source*. DOI: 10.3217/978-3-85125-615-4-04.
- [53] Julia Madrid et al. “A Virtual Design of Experiments Method to Evaluate the Effect of Design and Welding Parameters on Weld Quality in Aerospace Applications”. In: *Aerospace* 6.6 (2019), p. 74. DOI: 10.3390/aerospace6060074.
- [54] Kamel Rekab and Muzaffar Shaikh. *Statistical design of experiments with engineering applications*. Vol. volume 182. Statistics, textbooks and monographs. Boca Raton: Taylor & Francis, 2005. ISBN: 978-1-4200-5631-0. URL: <https://ebookcentral.proquest.com/lib/kxp/detail.action?docID=1568649>.
- [55] K. Siva Prasad. “Application of design of experiments to plasma Arc Welding Process: a review”. In: *ABCM* (2012).
- [56] Luiz Fernando C. S. Durão et al. “Optimizing additive manufacturing parameters for the fused deposition modeling technology using a design of experiments”. In: *Progress in Additive Manufacturing* 4.3 (2019), pp. 291–313. ISSN: 2363-9512. DOI: 10.1007/s40964-019-00075-9.
- [57] S. A. Abdul-Wahab and J. Abdo. “Optimization of multistage flash desalination process by using a two-level factorial design”. In: *Applied Thermal Engineering* 27.2-3 (2007), pp. 413–421. ISSN: 13594311. DOI: 10.1016/j.applthermaleng.2006.07.010.
- [58] Muhammad Asad Ahmad, Anwar Khalil Sheikh, and Kashif Nazir. “Design of experiment based statistical approaches to optimize submerged arc welding process parameters”. In: *ISA transactions* 94 (2019), pp. 307–315. DOI: 10.1016/j.isatra.2019.04.003.
- [59] Ashish Kumar and Kuntal Maji. “Selection of Process Parameters for Near-Net Shape Deposition in Wire Arc Additive Manufacturing by Genetic Algorithm”. In: *Journal of Materials Engineering and Performance* 29.5 (2020), pp. 3334–3352. ISSN: 1059-9495. DOI: 10.1007/s11665-020-04847-1.
- [60] MathWorks®. *Help Center - matlab® and Simulink® Documentation*. Ed. by MathWorks, Inc. R2022b. URL: <https://mathworks.com/help>.
- [61] G. Taguchi. “Quality engineering (Taguchi methods) for the development of electronic circuit technology”. In: *IEEE Transactions on Reliability* 44.2 (1995), pp. 225–229. ISSN: 00189529. DOI: 10.1109/24.387375.

- [62] Kenneth C. Mills. *Recommended values of thermophysical properties for selected commercial alloys*. Cambridge: Woodhead, 2002. ISBN: 9780871707536.
- [63] Jihong Yang et al. “Experimental investigation and 3D finite element prediction of the heat affected zone during laser assisted machining of Ti6Al4V alloy”. In: *Journal of Materials Processing Technology* 210.15 (2010), pp. 2215–2222. ISSN: 09240136. DOI: 10.1016/j.jmatprotec.2010.08.007.
- [64] Roloff Matek. *Maschinenelemente: Normung, Berechnung, Gestaltung*. 20., überarb. und erw. Aufl. Wiesbaden: Vieweg + Teubner, 2011. ISBN: 978-3-8348-1454-8.

# A Improved Material Model for Ti-6Al-4V

Data points of the generated material shown in chapter 5 are documented with a sampling rate of 50°C for later comprehensibility.

**Table A.1:** Exported datapoints for the improved material model of Ti-6Al-4V

T °C	$\varepsilon_r$ -	$\rho$ $\frac{\text{kg}}{\text{m}^3}$	$c_p$ $\frac{\text{J}}{\text{kg}\cdot\text{K}}$	$k$ $\frac{\text{W}}{\text{m}^2\cdot\text{K}}$	T °C	$\varepsilon_r$ -	$\rho$ $\frac{\text{kg}}{\text{m}^3}$	$c_p$ $\frac{\text{J}}{\text{kg}\cdot\text{K}}$	$k$ $\frac{\text{W}}{\text{m}^2\cdot\text{K}}$
0	0.233	4424	540	6.5	995	0.301	4282	753	22.7
50	0.233	4416	551	7.1	1000	0.304	4281	642	19.3
100	0.233	4409	562	7.7	1050	0.336	4274	651	20.4
150	0.233	4402	573	8.3	1100	0.384	4267	660	21.3
200	0.233	4395	584	8.9	1150	0.453	4260	669	22.0
250	0.233	4388	595	9.4	1200	0.554	4253	678	22.7
300	0.233	4381	606	10.0	1250	0.701	4246	687	23.2
350	0.234	4374	618	10.6	1300	0.917	4239	696	23.7
400	0.234	4367	629	11.2	1350	1.000	4232	705	24.2
450	0.234	4360	640	11.9	1400	1.000	4225	714	24.6
500	0.235	4352	651	12.6	1450	1.000	4217	723	25.1
550	0.235	4345	662	13.3	1500	1.000	4210	732	25.7
600	0.237	4338	673	14.1	1550	1.000	4203	741	26.4
650	0.238	4331	683	14.9	1600	1.000	4196	750	27.2
700	0.240	4324	694	15.8	1650	1.000	4189	759	28.2
750	0.244	4317	704	16.7	1700	1.000	3886	831	34.1
800	0.249	4310	715	17.8	1750	1.000	3852	831	34.3
850	0.256	4303	725	18.9	1800	1.000	3818	831	34.4
900	0.266	4296	734	20.1	1850	1.000	3784	831	34.6
950	0.282	4289	744	21.4	1900	1.000	3750	831	34.8

## B Design of Experiments

In the following, parameter variation tables applied in DoE are documented.

**Table B.1:** Tabulated experimental plan for parameter variation run 1

Run Name	$f_f$ -	$C_z$ m	$C_f$ m	$C_r$ m
0_V1_S1128_Ti64	0.33	0.002	0.004	0.008
1_V1_S1128_Ti64	0.275	0.003	0.003	0.0075
2_V1_S1128_Ti64	0.275	0.003	0.003	0.0105
3_V1_S1128_Ti64	0.275	0.003	0.005	0.0075
4_V1_S1128_Ti64	0.275	0.003	0.005	0.0105
5_V1_S1128_Ti64	0.275	0.005	0.003	0.0075
6_V1_S1128_Ti64	0.275	0.005	0.003	0.0105
7_V1_S1128_Ti64	0.275	0.005	0.005	0.0075
8_V1_S1128_Ti64	0.275	0.005	0.005	0.0105
9_V1_S1128_Ti64	0.425	0.003	0.003	0.0075
10_V1_S1128_Ti64	0.425	0.003	0.003	0.0105
11_V1_S1128_Ti64	0.425	0.003	0.005	0.0075
12_V1_S1128_Ti64	0.425	0.003	0.005	0.0105
13_V1_S1128_Ti64	0.425	0.005	0.003	0.0075
14_V1_S1128_Ti64	0.425	0.005	0.003	0.0105
15_V1_S1128_Ti64	0.425	0.005	0.005	0.0075
16_V1_S1128_Ti64	0.425	0.005	0.005	0.0105
17_V1_S1128_Ti64	0.2	0.004	0.004	0.009
18_V1_S1128_Ti64	0.5	0.004	0.004	0.009
19_V1_S1128_Ti64	0.35	0.002	0.004	0.009
20_V1_S1128_Ti64	0.35	0.006	0.004	0.009
21_V1_S1128_Ti64	0.35	0.004	0.002	0.009
22_V1_S1128_Ti64	0.35	0.004	0.006	0.009
23_V1_S1128_Ti64	0.35	0.004	0.004	0.006
24_V1_S1128_Ti64	0.35	0.004	0.004	0.012
25_V1_S1128_Ti64	0.35	0.004	0.004	0.009

**Table B.2:** Tabulated experimental plan for parameter variation run 2

Run Name	$f_f$ -	$\eta$ -	$T_i$ °C
0_V2_S1128_Ti64	0.330	0.350	50
1_V2_S1128_Ti64	0.280	0.260	46
2_V2_S1128_Ti64	0.280	0.260	124
3_V2_S1128_Ti64	0.280	0.440	46
4_V2_S1128_Ti64	0.280	0.440	124
5_V2_S1128_Ti64	0.370	0.260	46
6_V2_S1128_Ti64	0.370	0.260	124
7_V2_S1128_Ti64	0.370	0.440	46
8_V2_S1128_Ti64	0.370	0.440	124
9_V2_S1128_Ti64	0.250	0.350	85
10_V2_S1128_Ti64	0.400	0.350	85
11_V2_S1128_Ti64	0.325	0.200	85
12_V2_S1128_Ti64	0.325	0.500	85
13_V2_S1128_Ti64	0.325	0.350	20
14_V2_S1128_Ti64	0.325	0.350	150
15_V2_S1128_Ti64	0.325	0.350	85

**Table B.3:** Tabulated experimental plan for parameter variation run 3

Run Name	$f_f$ -	$\eta$ -	$k$ $\frac{N}{s \cdot mm \cdot K}$
0_V3_S1128_Ti64	0.660	0.350	8
1_V3_S1128_Ti64	0.560	0.280	6
2_V3_S1128_Ti64	0.560	0.280	9
3_V3_S1128_Ti64	0.560	0.370	6
4_V3_S1128_Ti64	0.560	0.370	9
5_V3_S1128_Ti64	0.740	0.280	6
6_V3_S1128_Ti64	0.740	0.280	9
7_V3_S1128_Ti64	0.740	0.370	6
8_V3_S1128_Ti64	0.740	0.370	9
9_V3_S1128_Ti64	0.740	0.325	7.5
10_V3_S1128_Ti64	0.500	0.325	7.5
11_V3_S1128_Ti64	0.800	0.250	7.5
12_V3_S1128_Ti64	0.650	0.400	7.5
13_V3_S1128_Ti64	0.650	0.325	5
14_V3_S1128_Ti64	0.650	0.325	10
15_V3_S1128_Ti64	0.650	0.325	7.5